(83)

Seismic Characterization Of Fractured Reservoirs (Part I)
Crustal Deformation In the Tibetan Plateau (Part II)

by

Feng Shen

Ph.D Sedimentology (1994)
Graduate School, Chinese Academy of Geosciences (Beijing)

Submitted to the Department of Earth, Atmospheric and Planetary Sciences in partial fulfillment of the requirements for the degree of

Doctor of Philosophy

at the

MASSACHUSETTS INSTITUTE OF TECHNOLOGY

December, 1998

[February, 1999]

Author .....
Department of Earth, Atmospheric, and Planetary Sciences
December, 1998

Certified by .....
M. Nafi Toksöz
Professor of Geophysics
Thesis Supervisor

Certified by .....
Leigh Royden
Professor of Geophysics and Geology
Thesis Co-Supervisor

Accepted by .....
Ronald Prinn
Chairman
Department of Earth, Atmospheric and Planetary Sciences

SEISMIC CHARACTERIZATION OF FRACTURED RESERVOIRS (PART I)
CRUSTAL DEFORMATION IN TIBETAN PLATEAU (PART II)

by

FENG SHEN

Submitted to the Department of Earth, Atmospheric and Planetary Sciences
Massachusetts Institute of Technology
December 1998
in partial fulfillment of the requirements for the degree of Doctor of Philosophy

ABSTRACT (PART I)

In this thesis, we study the possibility of using P-waves to investigate properties of fractured reservoirs and the diagnostic ability of the P-wave seismic data to detect fractures. The objectives of this thesis are threefold: (1) to identify the effects of fracture parameters and background media on the NMO velocities and azimuthal AVO responses in homogeneously fractured reservoirs, (2) to investigate the scattering characteristics in heterogeneously fractured reservoirs and the diagnostic ability of these characteristics to recover fracture density information, (3) to apply these theoretical studies and techniques to the field data analyses in order to detect fractures.

Fracture properties, described by fracture parameters (fracture density, fracture aspect ratio and saturating fluid), are related to anisotropic parameters of the equivalent VTI model and affect the NMO velocities. Studies show that the shear wave splitting parameter is most sensitive to crack density and is insensitive to saturating fluid content and the crack aspect ratio, while $\delta^{(v)}$ and $\varepsilon^{(v)}$ have different characteristics in gas- and water-saturating, fractured rocks. The effects of fracture parameters on P-wave NMO velocities are comparable with the influences of $\delta^{(v)}$.

Unlike anisotropic parameters and NMO velocities, P-wave azimuthal AVO variations are not necessarily correlated with the magnitude of fracture density. Studies show that the properties of background rocks have an important effect on P-wave azimuthal AVO responses. Azimuthal AVO variations at the top of gas-saturated, fractured reservoirs which contain the same fracture density are significant in the reservoir model with small contrasts in Poisson's ratio. Varying fracture density and fluid content can lead to variations in AVO gradients in off fracture strike directions. The presence of overburden anisotropy caused by VTI media can significantly distort AVO gradients, which suggests that the inversion of fracture parameters based on an individual AVO curve would be biased without correcting for this influence. By using primarily P-wave data, studies indicate that though studying azimuthal AVO variations could be effective for detecting fractures, the combination of other of data is more beneficial than using reflection amplitude data alone. Quantitative interpretation can be difficult when using the P-wave seismic signatures alone because of the variables discussed above.

Considering heterogeneity of fracture density due to spatial variations, statistical representation is employed to model the fracture density field and build the fracture density realizations. In this study, for stochastic modeling to be practical, the fracture density field is modeled as a spatially stationary Gaussian random field. The von Karman correlation function is used to model heterogeneity in fracture density, which is specified by the function describing its amplitude, orientation, characteristic wave numbers and its roughness number. The scattering characteristics, including amplitude and frequency, are investigated at the tops and

the bases of gas saturated, fractured reservoirs. Results show that the strength of the scattering field is a function of the background medium. Scattering field, are weak at the top of fractured reservoirs. The first order results are dominated by velocity anisotropy of a mean crack density field. The base of the fractured reservoir corresponds to a strong scattering field on which fracture heterogeneity has a larger effect. The strength of the scattering field at the base of a fractured reservoir is inversely proportional to the correlation length of the fracture density field and is proportional to the scatter (fracture) density.

An estimation procedure is applied to field data analyses to obtain the offset-dependent attributes, the amplitude versus offset (AVO) and the frequency versus offset (FVO). These attributes are applied to determine principal orientation of fractures in carbonate fractured reservoirs located in the Maporal field in the Barinas basin in southwestern Venezuela. Our studies show that, in this area, P-wave reflectivity is characterized by a large increase of amplitude with offset (large positive AVO gradient) and a large frequency decay with offset (large negative FVO gradients) in the crack normal direction. In the crack strike direction, P-wave reflectivity is characterized by a scatter distribution of AVO gradients but a small variation of FVO gradients. Velocity attributes, inverted from near-offset and the whole range of offset stacked amplitude, are used to predict the lateral lithological heterogeneity in the reservoir zone. The variations of AVO gradients in the crack strike direction can be attributed to heterogeneity in the reservoir.

ABSTRACT (PART II)

The objectives of this thesis are twofold: (1) to understand how the strength of upper and lower crust influences the topographic features, (2) to understand the tectonic evolution of the Tibetan plateau and the basic processes that control its deformation.

A 3-D, large-scale analytical model is used to model continental crustal deformation in the Tibetan plateau. The idealized crust is assumed to consist of two layers, an upper layer with a uniform viscosity and a lower layer with viscosity decreasing exponentially with depth. The motions of the underlying mantle are the fundamental driving forces for crustal thickening. The parameters used in modeling are constrained mainly by observations in the India-Asia collision zone of topography. The modeled results reveal that the growth of the Tibetan plateau can be divided into two phases: the mountain building and plateau phases. With the thickening of crust, the spatial and temporal characteristics of deformation are different in these two phases.

Numerical experiments yield spatial distributions of velocity, strain and rotation rate on the modeled Tibetan plateau. The modeled velocity results indicate that right-lateral motion occurs between India and south China. Large extension is located at the edges of the high plateau and the development of surface extension is proportional to the weakness of the lower crust. Rapid shortening occurs on the flanks of the plateau and is oriented roughly perpendicular to the regional topographic contours. In the central plateau, deformation is characterized by E-W extension. Much of the relative right-lateral motion is accomplished by clockwise rotation in the region of eastern syntaxis. The maximum rates of rotation about vertical axes occurs in the region of the eastern syntaxis proper.

Thesis Supervisor: M. Nafi Toksöz, Professor of Geophysics
Thesis Co-Supervisor: Leigh H. Royden, Professor of Geophysics and Geology

Listing of Key of Variables and Symbols

Seismic Characterization of Fractured Reservoirs (Part I)

δ	Thomsen parameters in VTI media
ε	Thomsen parameters in VTI media
γ	Thomsen parameters in VTI media
$\delta^{(v)}$	Anisotropic parameters of the equivalent VTI model
$\varepsilon^{(v)}$	Anisotropic parameters of the equivalent VTI model
$\gamma^{(v)}$	Anisotropic parameters of the equivalent VTI model
AVO	Amplitude vs. Offset
C_{ij}	Elastic stiffness tensor
FVO	Frequency vs. Offset
HTI	Transversely isotropic medium with a horizontal symmetry axis
MDL	Minimum description length
MUSIC	Multiple signal classification
NMO velocity	Normal Moveout velocity
S^{b}_{ijkl}	Compliance tensor of the unfractured background rock
S^{f}_{ijkl}	Excess compliance tensor induced by fractures
U_{11}	Discontinuity in transverse displacement
U_{33}	Discontinuity in normal displacement
VTI	Transversely isotropic medium with a vertical symmetry axis
ρ	Rock density
λ, μ	Lame parameters
ϕ	Azimuthal Angle
σ_{kl}	Average stress tensor
Z_N	Fracture normal compliance tensor
Z_T	Tangential compliance tensor

Crustal Deformation in the Tibetan Plateau (Part II)

b	Upper layer thickness
h	Lower crustal thickness
$b+h_o$	Initial crustal thickness
μ_o	Uniform viscosity of the upper layer
α	Viscosity decay coefficient

Table of Contents

Acknowledgments

This thesis has benefited from the influence of a number of people. First of all, I would like to thank my advisors, professor Nafi Toksöz and professor Wiki Royden.

Nafi provided me with the opportunity to work and learn exploration geophysics within a stimulating research environment at the Earth Resource Laboratory (ERL) for which I will always be grateful. My learning and research benefit from the considerable input of his knowledge and his ability touch key points of a question directly and think about a question critically. His support, patience and encouragement accompany my learning and research at ERL. All of these will certainly be a very nice memory to keep in my life.

I am grateful to Wiki for her support, encouragement, help and patient guidance whenever I needed it. Her scientific insights into understanding the essential physics of a problem using analytical models are very impressive. I am deeply thankful to her for allowing me the freedom to explore and develop my own interests and research directions. Over the past few years, she has contributed immensely to my education.

I have also greatly benefited from working with Dr. Bob King on GPS and very much appreciate him for patiently teaching me about GPS data processing and analysis as well as in English writing. I thank him for his time and efforts. I had a very good time working with professor Tom Herring on GPS research. His GPS courses were very enjoyable and had broadened my perception of geodesy. I will be always appreciate his help and encouragement.

This thesis benefits from Ningya Cheng's Ph.D thesis work and Xiang Zhu's investigation in his M.S. thesis. I thank Ningya Cheng for his helpful discussion in his 3-D finite difference code. I believe the pleasurable memory and friendship with Xiang will always be kept in this thesis. I thank Maria for her great help in the seismic data processing with Promax. I appreciate Helen Webb's enthusiasm and willingness to discuss the stochastic modeling technique with me.

I owe a great deal of gratitude to the people at ERL. I would specifically like to thank Dr. Dan Burns. He has proven to be a reliable source of inspiration, encouragement and advice. Jesus Sierra, my officemate, generously shared his industry working experience

with me and was a great source of knowledge on practicality. His encouragement gives me stability in my research directions. Franklin Ruiz's friendship, sense of humor and enthusiasm relieved a lots of frustration during my research. I thank Abdulfattah Al-Dajani for his many good, enthusiastic suggestions. I would also like to thank Joe Matarese for his valuable discussions in the use of the nCUBE parallel computing facilities. I want to thank Dr.s Zhenya Zhu, Chuck Doll, Roger Turpening, Bill Rodi, Matthijs Haartsen, Matthias Imhof and Rick Gibson for their friendship and help. In addition, Liz Henderson, Sue Turbak and Sara Brydges were always helpful in administrative matters. I thank Jane Maloof for making ERL computers run smoothly. Kate Jesdale's help and efforts in improving my English writing for this thesis and other papers are greatly appreciated.

Students past and present who have shared their ideas, help and friendship made my difficult graduate life turn out to be enjoyable: Ming Fang, Xiaojun Huang, Yu Jin, Peter Kaufman, Mary Krasovec, Lana Panasyuk, Michael Pope, Shirley Rieven, Paula Waschbusch, Mousumi Roy, Wenqun Shi, Youshun Sun, Jie Zhang, Jonathan Kane. Specifically, I would like to thank Yu Jin for his generous help in my study and research and for his sincere friendship in my difficult graduate life. Erchie Wang deserves my true gratitude for his understanding, support and valuable encouragement.

Outside MIT, I am thankful for help discussions, valuable comments and encouragement from Dr. John Queen.

I appreciate my thesis committee members for their efforts: Professor Michel Bouchon, Dr. Reinaldo Michelena, Professor John Grotzinger, Professor Chris Marone.

On the other side of the earth, my first Ph.D thesis advisor, professor Baojun Liu deserves great gratitude. I don't think that I would have attempted to start my second Ph.D graduate life at MIT were it not for his relentless encouragement, sincere enthusiasm and recommendations. I express my deep gratitude to my master thesis advisors: professor Shaoxin Qian and professor Wenlin Liu for their particular influence on my studies in exploration geophysics. I thank my good friend Dr. Enru Liu of British Geological Survey for teaching me seismic anisotropy through emails and enjoyable times at SEG meetings.

I thank the corporation project between MIT and Chengdu Geological Institute, Department of Geological Ministry headed by Professor Clark Burchfiel and Professor

Zhiliang Chen for providing me with such a good opportunity to study at MIT. I also thank Professor Xueyang Zhang, Professor Xijiang Zhao and Professor Yuping Liu for their generous help in GPS data and files.

I am deeply grateful my parents for their constant love, support and encouragement. Down my chosen path, their understanding and enthusiasm always company me...

The first part of the thesis was supported by the Borehole Acoustics and Logging/Reservoir Delineation Consortium at M.I.T. The seismic data sets are provided by Intervep, S. A.

CHAPTER 1

Introduction

The state of stress and its variation with time are two of the most fundamental physical parameters controlling the deformation of rocks. The study of the state of stress in the Earth's crust and the rheological behavior of rocks ranges from near surface conditions down to mid crustal levels. Our current understanding of the rheology of the continental crust is based primarily on laboratory studies of rock strength under greatly simplified conditions. These studies indicate that two major processes control the mechanical behavior of crustal rocks: (1) At upper crustal levels, deformation causes brittle failure and rock strength is limited by frictional strength of preexisting faults or fractures. (2) At great depth, above a certain temperature or at low strain rates, rock strength is determined by ductile flow laws and decreases approximately exponentially with increasing temperature. This thesis studies the deformation of rocks in these two different deformation regimes and at two different scales, macro-fracture scale and crustal scale. The physical behavior at the macro-fracture scale is investigated though seismic responses; the ductile rheological behavior of rocks is investigated by examining their deformation at crustal and tectonic scales.

At lower temperatures and pressures, rock is a brittle material that will fail by fractures if the stress becomes sufficiently large. Fractures are widely observed in surface rocks of all types. When a lateral displacement takes place on a fracture, the break is referred to as a fault. Open-fractures develop as secondary features along and within fault zones and serve as conduits for the transport of hydrocarbons (Nelson, 1985), geothermal fluids (Takahashi and Abe, 1989) or groundwater (Long and Wood, 1986). In the petroleum industry, hydrocarbon reservoirs generally are composed of porous permeable zones interbeded with relatively impermeable shale beds. Vertically aligned fractures in reservoirs and shale beds overlying the reservoirs significantly affect the flow characteristics of reservoirs; and densities and orientations of fracture sets are of great interest. In sedimentary

basins, the fracture orientations are dominated by structural patterns. Fractures open at depth tend to be oriented normal to the direction of minimum in-situ compressive stress. The presence of vertically aligned fractures leads to seismic anisotropy, and the use of seismic anisotropy to determine the orientation of fracture sets is of considerable interest. Consequently, understanding the relationships between the response of seismic anisotropy and fracture properties is a first order problem for predicting the flow of fluids through reservoirs and aquifers.

Several theoretical studies of fracture-induced anisotropy have been reported in the literature (O'Connel and Budiansky, 1976; Budiansky and O'Connel, 1976; Hoenig, 1979; Hudson, 1980, 1981, 1986; Crampin et al., 1986; Hudson, et al., 1996). How the presence of the fracture sets affect the elastic modulus of fractured rocks has been discussed in the literature (Schoenberg and Sayers, 1995; Thomsen, 1995; Liu et al., 1996). Based on the simplifying assumption of linear and elastic behavior, it is the background elastic modulus and fracture parameters (fracture density, aspect ratio and saturating fluid) that determine the behavior of seismic waves which propagate through, and are reflected from, the reservoirs.

The development of fracture models has advanced our understanding of major physical features such as the azimuthal P- and S-wave velocity variations with fracture parameters. Owing to the high cost of multicomponent surveys, data quality control and their processing techniques, the possibility of using P-waves to investigate properties of fractured reservoirs becomes very promising. The azimuthal variations in P-wave velocity and reflectivity in homogeneously fractured reservoirs as a function of anisotropic parameters are described by Tsvankin (1996), Ruger (1995, 1998) and Al-Dajani and Tsvankin (1998). These anisotropic parameters are related to fracture parameters through the elastic stiffness tensors. In principle, azimuthal AVO responses can be used to detect fractures. Successful use of azimuthal variation of P-wave AVO signatures to determine the principal fracture orientation and density have been reported in the literature (Lynn et al., 1995; Lynn et al., 1996; Perez and Gibson, 1996). Studies of the major effects of fractures on anisotropic parameter properties and P-wave azimuthal AVO response can help explorationists to use this technology when only P-wave information is available.

In principle, the distribution of fractures in reservoir zones can be treated as homoge-

neous. In practice, the number and variability of small-scale fractures are so large that recovering significant information from P-wave seismic data requires that the distribution characteristics be averaged over the reservoir zone, which leads to a statistical representation. For our simulation to be simple and practical, we assume that fracture density does not vary with depth in the reservoir. The basis for the stochastic treatment is to consider the fractures to be a sample of a two-dimensional random process described by a set of observable statistics. The processes, represented as random fields defined over a continuous set of geographic coordinates, are considered. Heterogeneity due to spatial variations of fracture density could result in spatial variations of velocity anisotropy. Our studies of waves propagating in heterogeneously fractured reservoirs concentrate on identifying the coherent features in reflected seismic data. These features are often used as major seismic characteristics in exploration geophysics. The small incoherent arrivals which occur between the major reflections also contain information about the media, but these features are often treated as "noise." The stack technique, for example, suppresses these arrivals.

Analytic approaches such as Born approximation have received great attention for both forward and inverse modeling in seismic scattering studies. However, theoretical assumptions as a result of this approach violate the law of energy conservation, which is discussed in detail by Charrette (1991). The 3-D finite difference modeling technique is effective in studying the azimuthal AVO response and scattering characteristics in heterogeneously fractured media. Although grid memory requirements make computations very expensive and grid dispersion effects limit finite-difference models to small regions, this approach has been successfully used to model energy diffracted at highly irregular interfaces (Lavender and Hill, 1985; Dougherty and Stephen, 1987), to study fluid-filled borehole wave propagation problems in anisotropic formations (Cheng et al., 1995), and to study the scattering in isotropic media (Frankel and Clayton, 1986; Coates and Charrette, 1993, Zhu, 1997). Additionally, unlike boundary integral techniques, lateral velocity variations can be easily incorporated (Stephen, 1984, 1988).

When oblique incident waves are reflected at the top and the base of fractured reservoirs, their scattering shows different characteristics in both the time domain and frequency domain because of differences in wave propagation paths and transmitting processes. Reflected waves from the base of fractured media have been refracted at the top

of an interface and transmitted through fractured media. In addition to reflectivity variations, velocity variations are imposed on the transmitting and reflection processes. Unlike scattering studies in heterogeneously isotropic media, in which transmitted waves mainly are considered, we consider coherent reflected waves. Therefore, techniques with better resolution and better frequency estimation characteristics than general spectral techniques, such as autoregressive or Prony, are required to provide asymptotically unbiased estimations of signals. Moreover, investigating scattering characteristics of heterogeneously fractured reservoirs in the frequency domain is very important both in theoretical studies and field data analyses.

Azimuthal AVO variations have been used in fracture detection and density estimation (Perez, 1997; Ramos and Davis, 1997). However, the sensitivity of reflected P-waves to the discontinuity of elastic properties at a reflected boundary and to the spatial resolution makes it difficult to interpret this attribute unambiguously. The motivation of this thesis is to explore the efficiency, benefits and limitations of using P-waves to characterize fractured reservoirs, theoretically and practically. The major goal of this thesis is to study the possibility of using P-waves to investigate properties of fractured reservoirs and the diagnostic ability of the P-wave seismic data in fracture detection. Quantitatively characterizing fractured reservoirs is difficult when only the P-wave seismic signatures are available. The multicomponent technique may become promising.

Science progresses by postulating hypotheses, then testing these hypotheses with new experiments and observations. Our study of the rheological behavior of rocks at a crustal scale is based on observation and modeling of continental deformation, in particular deformation of the Tibetan plateau. The Tibetan plateau is the most conspicuous feature of continental topography on Earth and resulted from the north-south convergence between the Indian and Eurasian plates (Molnar and Tapponnier, 1975). Considerable effort has been made to understand its uplift and deformation for the purpose of understanding its history and its impact on climate. Despite the efforts made to investigate this collision zone, little consensus has developed with regard to the mechanisms of the Tibetan plateau uplift since the onset of the collision about 50 Ma (Sandvol, et al, 1997). It is now generally recognized that the high elevations of the region have been caused by mechanical thickening of the crust and flow in the mantle and several mechanisms have been proposed for the geo-

dynamic evolution of the Tibet-Himalayas collision zone (Xu, 1981; Molnar, 1988; England and Houseman, 1989; Burchfiel and Royden, 1991; Harrison et al., 1992; Jin et al, 1994; Hirn et al, 1995).

Several early calculations of collision related to deformation have concentrated on the crustal thickness distribution without a quantitative treatment of the deformation, such as strain rate and finite rotation. Tapponnier and Molnar (1976) study infinitesimal strains while neglecting vertical strain. Vilotte et al. (1982) compute small strains and neglect the influence of gravity acting on crustal thickness contrasts. The updated finite strain calculations by Houseman and England (1986) are based on a rheologically simple continuum model for the continental lithosphere to calculate stresses, strain rates, and strains. Recent calculations of Tibetan plateau uplift and its deformation have been proposed by Houseman and England (1993), Royden (1996) and Royden et al. (1997). Many of these studies have different tectonic implications.

Using quantitative deformation features, we can test models for continental deformation. Comparing the calculated results with the geophysical, geodetic and geological observation can lead to an understanding of the dynamics of continental deformation. This part of the thesis explores the relationship between the viscous properties of the crust, crustal thickening and associated surface deformation at a crustal scale in the Tibetan Plateau. This study is made using a three-dimensional analytic solution for crustal flow (Royden, 1996) that incorporates depth-dependent rheology with a geodynamic model of plateau formation. This analytic solution is derived from solutions of the fundamental equations that govern fluid flow in viscous media.

Organization

Chapters 2, 3 and 4 in this thesis are concerned with fracture studies by using P-wave reflected data. We regard the theoretical studies and investigations as the building block upon which field seismic data analysis is based. The work in the chapter 5 of the thesis is concerned with crustal thickening and deformation studies based on the theoretical frame of a three dimensional analytical solution. A list of abbreviations and symbols is given following the thesis abstract for easy reference.

Chapter 2 and Appendix 2-A constitute the theoretical foundation of seismic anisot-

ropy and the procedure for estimating elastic stiffness tensors in fractured media. In this chapter, we study the effects of fracture parameters, including fracture density, fracture aspect ratio and fracture fluid content, on adapted anisotropic parameters and NMO velocities. The study provides quantitative physical information regarding fracture properties. Reflectivity is directly related to the elastic discontinuity at a reflected boundary. The 3-D finite difference modeling technique is used to simulate the P-wave azimuthal AVO responses to investigate the influence of elastic properties of isotropic background rocks, overburden anisotropy and fractured reservoir properties (fracture density and fluid content) on these responses.

Chapter 3 and Appendixes 3-A and 3-B present the results of scattering characteristics at the top and the base of fractured reservoirs with a spatial variation in fracture density. We assume that the stochastic component of fracture density has a Gaussian probability distribution, described by its first and second moments (the mean and autocorrelation function). A frequency estimator is used to extract the offset-dependent attributes from coherent reflected seismic waveforms generated from 3-D finite difference modeling. We present results that vertically aligned fractures lead to both amplitude and frequency variations with azimuth. We compare scattering characteristics in the time domain and in the frequency domain and investigate the functional relationships between the scattering characteristics and background elastic contrasts, scattering strength, and correlation length of the fracture density field.

Chapter 4 shows the application of what has been learned from the forward modeling studies and estimation procedure to real data analyses. We study the seismic morphology and classify them into two groups: near-offset and far-offset and estimate the amplitude versus offset (AVO) and the frequency versus offset (FVO) from field seismic data in the Maporal field in the Barinas basin in southwestern Venezuela. We discuss the validity of by using azimuthal variations of AVO and FVO in fracture detection with the tuning distortion and spatial resolution stretch. Based on the theoretical studies and calculations, we relate statistic characteristics of these attributes to the principal fracture orientation. Inverted, offset-dependent velocities and theoretical calculations in reflectivity are used to predict lithological heterogeneity in reservoir zones and study the influence of reservoir heterogeneity on AVO signatures. This study interprets the scatter distribution in the AVO

gradients in the fracture strike direction of reservoir zones.

Chapter 5, as the part II of the thesis, is concerned with crustal thickening and deformation studies based on the theoretical frame of a three dimensional analytical solution. This chapter is organized following the chronological evolution of the modeled Tibetan plateau. This chronological evolution is composed of the following sequence of events: (1) the assumption of the collision between India and Eurasia about 40 Ma; (2) early mountain building phase; (3) late plateau phase; (4) present surface deformation and characteristics.

REFERENCES

Al-Dajani, A., and Tsvankin, I, 1998, Nonhyperbolic reflection moveout for horizontal transverse isotropy, Geophysics, 63, 1738-1753.

Budianksy, B., and O'Connel, R., 1976, Elastic moduli of a cracked solid: International J. Solids Struct., 12, 81-87.

Burchfiel, B. C., and Royden, L. H., 1991, Tectonics of Asia 50 years after the death of Emile Argand, Eclogae Geol. Helv. 84, 599-629.

Burchfiel, B. C., Chen, Z., Liu, Y., and Royden, L. H., 1996, Tectonics of the Longmen Shan and adjacent regions, International Geological Review, 37, 661-735.

Charrete, E. E., 1991, Elastic wave scattering in random media, Ph.D. Thesis, Massachusetts Institute of Technology.

Cheng, N., Cheng, C. H., and Toksoz, M. N., 1995, Borehole wave propagation in three-dimensions, J. Acoust. Soc. Am., 97, 3483-3493.

Coates, R. T., and Charrette, E. E., 1993, A comparison of signal scattering and finite difference synthetic seismograms in realizations of 2-D elastic random media, Geophys. J. Int., 113, 463-482.

Crampin, S., McGonigle, R., and Ando, M., 1986, Extensive-dilatancy anisotropy beneath Mount Hood, origin and the effect of aspect ratio on seismic velocities through aligned cracks, J. Geophys. Res., 91, 12703-12710.

Dougherty, M. E., and Stephen, R. A., 1987, Geoacoustic scattering from seafloor features in the ROSE area, J. Acoust. Soc. Am., 82, 238-256.

England, P., and Houseman, G., 1989, Extension during the continental convergence, with

application to the Tibetan Plateau, J. Geophys. Res., 98, 17561-17579.

Frankel, A., and Clayton, R. W., 1986, Finite-difference simulations of seismic scattering: Implications for the propagation of short-period seismic waves in the crust and models of crustal heterogeneity, J. Geophys. Res., 91, 6465-6489.

Jin, Y., McNutt, M. K., and Zhu, Y. S., 1994, Evidence from gravity and topography data for folding of Tibet, Nature, 371, 669-674.

Harrison, T. M., Copeland, P., Kidd, W. S. F., and Yin, A., 1992, Raising Tibet, Science 255, 1663-1670, 1992.

Hirn, A., Jiang, M., Sapin, M., Diaz, J., Nercessian, A., Lu, Q. T., Lepine, J. C., Shi, D. N., Sachpazi, M., Pandey, M. R., Ma, K., and Gallart, J., 1995, Seismic anisotropy as an indicator of mantle flow beneath the Himalayas and Tibet, Nature, Vol. 375, 571-574.

Hoenig, A., 1979, Elastic moduli of a non-randomly cracked body: International J. Solids Struct., 15, 137-154.

Houseman, G., and England, P., 1986, Finite strain calculations of continental deformation, 1, methods and general results for convergent zones, J. Geophys. Res., 91, 3651-3663.

Houseman, G., and England, P., 1993, Crustal thickening versus lateral expulsion in the Indian-Asian continental collision, J. Geophys. Res., 98, 12233-12249.

Hudson, J. A., 1980, Overall properties of a cracked solid: Math. Proc. Camb. Phil. Soc., 88, 371-384.

Hudson, J. A., 1981, Wave speeds and attenuations of elastic waves in material containing cracks, Geophys. J. Roy. Astr. Soc., 64, 133-150.

Hudson, J. A., 1986, A higher order approximation to the wave propagation constants for a cracked solid: Geophys. J. Roy. Astr. Soc., 87, 265-274.

Hudson, J. A., Liu, E., and Crampin, S., 1996, Transmission properties of a plan fault, Geophys. J. Int., 125, 559-566.

Lavender, A. R., and Hill, N. R., 1985, P-SV resonances in irregular low velocity surface layers, Bull. Seism. Soc. Am., 75, 847-864.

Liu, E., MacBeth, C., Point, C., and Hudson, J. A., 1996, The effective elastic compliance of fractured rock, 66th Ann. Internat. Mtg., Soc. Expl. Geophys., Expanded Abstracts, 1842-1845.

Lynn, H. B., Bates, C. R., Simon, K. M., and van Dok, R., 1995, The effects of azimuthal anisotropy in P-wave 3-D seismic, 65th Ann. Internat. Mtg., Soc. Expl. Geophys., Expanded Abstracts, 723-730.

Lynn, H. B., Simon, K. M., and Bates, C. R., 1996, Correlation between P-wave AVOA and S-wave traveltime anisotropy in a naturally fractured gas reservoir, The Leading Edge, 15, 931-935.

Long, P. E., and Wood, B. J., Structures, textures and cooling histories of Columbia River basalt flows, Geol. Soc. Am. Bull., 97, 1144-1155, 1986.

Molnar, P., and Tapponnier, P., 1975, Cenozoic tectonics of Asia: Effects of a continental collision, Science, 189, 419-426, 1975.

Nelson, R. A., 1985, Geological analysis of naturally fractured reservoirs, Gulf, Houston, Tex.

O'Connel, R., and Budianksy, B., 1976, Seismic velocities in dry and saturated cracked solids: J. Geophys. Res., 79, 5412-5426.

Perez, M., 1997, Detection of fracture orientation using azimuthal variation of P-wave AVO response, M.S. thesis, 95 pp., Mass. Inst. of Technol., Cambridge.

Perez, M., and Gibson, R., 1996, Detection of fracture orientation using azimuthal variation of P-wave AVO responses: Barinas field (Venezuela), 66th Ann. Internat. Mtg., Soc. Expl. Geophys., Expanded Abstracts, 1353-1356.

Ramos, A. C. B., and Davis, T. L., 1997, 3-D AVO analysis and modeling applied to fracture detection in coalbed methane reservoirs, Geophysics, 62, 1683-1695.

Royden, L., 1996, Coupling and decoupling of crust and mantle in convengent orogens: Implications for strain partitioning in the crust, J. Geophys. Res., 101, 17679-

Royden, L., Burchfiel, B. C., King, R. W., Wang, E., Chen, Z., Shen, F., and Liu, Y., 1997, Surface Deformation and Lower Crustl Flow in Eastern Tibet, Science, 276, 788-790.

Ruger, A., 1995, P-wave reflection coefficients for transversely isotropic media with vertical and horizontal axes of symmetry: 65th Ann. Internat. Mtg., Soc. Expl. Geophys., Expanded Abstracts, 278-281.

Ruger, A., 1998, Variation of P-wave reflectivity with offset and azimuth in anisotropic media, Geophysics, 63, 935-947.

Sandvol, E., Ni, J., Kind, R., and Zhao, W., 1997, Seismic anisotropy beneath the southern

Himalayas-Tibet collision zone, J. Geophys. Res., 102, 17813-17823.

Schoenberg, M., and Sayers, C. M., 1995, Seismic anisotropy of fractured rock, Geophysics, 60, 204-211.

Stephen, R. A., 1984, Finite-difference seismograms for laterally varying marine models, Geophys. J. R. Astr. Soc., 79, 185-198.

Stephen, R. A., 1988, Lateral heterogeneity in the upper oceanic crust at DSDP Site 504, J. Geophys. Res., 93, 6571-6584.

Takahashi, H., and Abe, H., 1989, Fracture mechanics applied to hot, dry rock geothermal energy, in Fracture Mechanics of Rock, edited by Atkinson, B., K., pp. 241-276, Academic, San Diego, Calif.

Tapponnier, P., and Molnar, P., 1976, Slip-line field theory and large-scale continental tectonics, Nature, 264, 319-324.

Thomsen, L., 1995, Elastic anisotropy due to aligned cracks in porous rock, Geophysical Prospecting, 43, 805-829.

Tsvankin, I., 1996, P-wave signatures and notation for transversely isotropic media: An overview, Geophysics, 61, 467-483.

Vilotte, J. P., Diagnieres, M., and Madariaga, R., 1982, Numerical modeling of intraplate deformation: Simple mechanical models of continental collision, J. Geophys. Res., 87, 10709-10728.

Xu, R., 1981, in Geology, Geological History and Origin of Qinghai-Xizang Plateau (Since Press, Beijing, 1981), Vol. 1, pp. 139-144.

Zhu, X., 1997, 3-D Numerical Modeling of the P and SV wave reflections from fractured reservoirs, M.S. thesis, 55 pp., Massachusetts Institute of Technology, Cambridge.

CHAPTER 2

Effects of fractures on NMO velocities and P-wave azimuthal AVO response

2.1 ABSTRACT

The effects of fracture parameters on anisotropic parameter properties and P-wave NMO velocities are investigated based on developed effective medium models and crack models. Anisotropic parameters of the equivalent VTI model, $\delta^{(v)}$ and $\varepsilon^{(v)}$, have different characteristics in gas- and water-saturated, fractured sandstones. When fractures are gas-saturated, $\delta^{(v)}$ and $\varepsilon^{(v)}$ vary with the fracture density alone. In water-saturated, fractured sandstones, both $\delta^{(v)}$ and $\varepsilon^{(v)}$ depend on fracture density and crack aspect ratio. $\delta^{(v)}$ is related to the Vp/V_S of background rocks and $\varepsilon^{(v)}$ is a function of the Vp of background rocks. Studies show that the shear wave splitting parameter, $\gamma^{(v)}$, is most sensitive to crack density and insensitive to saturated fluid content and crack aspect ratio. Properties of P-wave NMO velocities in a horizontally layered medium are the function of $\delta^{(v)}$. The effects of fracture parameters on P-wave NMO velocities are comparable with the influences of $\delta^{(v)}$.

P-wave azimuthal AVO variations are not necessarily correlated with the magnitude of fracture density. Our studies show that the elastic properties of background rocks have an important effect on P-wave azimuthal AVO responses. Results from 3-D finite difference modeling show that azimuthal AVO variations at the top of gas-saturated, fractured reservoirs which contain the same fracture density are significant in the reservoir model with small Poisson's ratio contrast. As shown in our analytic solutions, azimuthal AVO variations are detectable when fracture-induced reflection coefficients can generate a noticeable perturbation in the overall reflection coefficients. Varying fracture density and saturated fluid content can lead to variations in AVO gradients in off fracture strike directions. Our numerical results also show that AVO gradients may be significantly distorted in the pres-

ence of overburden anisotropy caused by VTI media, which suggests that the inversion of fracture parameters based on an individual AVO curve would be biased without correcting this influence. By using primarily P-wave data, our studies indicate that though studying azimuthal AVO variations could be effective for detecting fractures, model analysis studies and combination of P-wave NMO velocities are more beneficial than using reflection amplitude data alone.

2.2 INTRODUCTION

Owing to the high cost of multicomponent surveys, data quality control and their processing techniques, the possibility of using P-waves to investigate properties of fractured reservoirs is very promising. Natural fractures in tight, low-porosity, low permeability reservoirs have very important influence on the flow characteristics of reservoirs. The fracture density and its principal orientation are of great interest. Azimuthal anomalies of P-wave stacking velocities and reflection amplitudes induced by fractures have been observed in field seismic data and studied in theory.

Seismic P-wave travel time and stacking velocity anomalies induced by fractures have been used in determining the fracture orientation. Paul (1993) attributes anomalously low stacking velocities to the presence of localized fractures. In the Wind River Basin in central Wyoming, Lynn et al. (1995) note that azimuth-dependent stacking velocities are related to the presence of fractures. Corrigan et al. (1996) present a case study to show the substantial azimuthal variations in NMO velocities in fractured reservoirs. In theoretical studies, Thomsen (1988) presents the weak-anisotropy approximation for NMO velocities of P- and S-waves from a horizontal reflector in the symmetry plane of HTI media that contains the symmetry axis. Recently, Tsvankin (1997) presents an exact equation for NMO velocities of pure modes valid for any orientation of the survey line over an HTI layer. Sayers and Ebrom (1997) present a nonhyperbolic traveltime equation which can be used for velocity analysis in the presence of azimuthally anisotropic layered media. These theoretical studies make it possible for us to find the crack orientation and, in some cases, estimate the crack density in fractured reservoirs by using P-wave NMO velocity data.

Numerical simulations and physical experiments show that the existence of vertical fractures leads to azimuthal AVO variations, which can be used to determine the principal

direction of fractures (Mallick and Frazer 1991; Sayers and Rickett, 1997; Chang and Gardner, 1993). Lynn et al. (1996) present field data examples showing a correlation between azimuthal difference in P-wave AVO and S-wave anisotropy, demonstrating the potential of using P-waves to characterize fractured reservoirs. Based on a 3-D AVO technique, Ramos and Davis (1997) show spatial variations of crack density in coal bed methane reservoirs. Mallick et al. (1998) use periodic azimuthal dependence of P-wave reflection amplitudes to identify two distinct cases of anisotropy detection.

Interpretation and inversion of azimuthal anomalies of P-wave NMO velocities and amplitudes over fractured reservoirs are difficult without understanding the dependence of anisotropic parameters and NMO velocities on fracture parameters. Additionally, azimuthal anomalies of P-wave amplitudes depend on discontinuities in elastic properties and anisotropy at a reflection boundary. The question is raised of how fracture parameters (fracture density, fracture aspect ratio and saturated-fluid content), elastic properties of isotropic background rocks, and overburden anisotropy induced by VTI media affect the P-wave reflection anomalies. We begin to answer this question in this chapter. We also investigate how much detail can be interpreted reliably from our seismic data. This question is particularly pertinent to fractured reservoirs, where geological control and other source information are scarce.

To gain insight into anisotropic reflectivity and obtain relationships between the model parameters and reflection amplitudes, the P-P reflection coefficients need to be calculated. One way to calculate the P-P reflection coefficients is based on derived approximate equations of reflection coefficient (Ruger, 1995; Ruger 1998; Haugen and Ursin, 1996). These equations are based on assumptions of weak anisotropy and a boundary with small discontinuities in elastic properties. To avoid assumptions and limitations common to analytical studies and to obtain accurate seismic amplitudes from anisotropic media, we mainly use the 3-D finite difference modeling technique in this chapter. Although computationally very expensive, we favor this technique because it is accurate over a wide range of anisotropy regimes, all wave types (direct wave, reflected wave, multiply scattered waves, converted waves, etc.) are included, and it produces synthetic seismograms for any point on the grid and covers any azimuth.

In this chapter, seismic anisotropy due to vertically aligned fractures is reviewed first

and the 'equant porosity' model (Thomsen, 1986) is not considered. We investigate and discuss effects of fracture parameters on properties of anisotropic parameters of the equivalent VTI model and on NMO velocities. Based on our numerically modeled results, we study how the elastic property contrasts of background media affect the azimuthal AVO signatures at the top of fractured reservoirs. Supplemented by approximate, analytical solutions of reflection coefficients, we analyze the anisotropic contributions induced by fractures to overall azimuthal AVO variations. We also model the effect of overburden anisotropy, generated by VTI media, on azimuthal AVO responses. The objective of this chapter is to provide some insights into the relationship between the medium parameters and seismic signatures and to help better use P-wave seismic data to characterize fractured reservoirs.

2.3 SEISMIC ANISOTROPY AND NMO VELOCITIES IN FRACTURED RESERVOIRS

2.3.1 Estimation of the effective elastic modulus

For an isotropic medium containing a single set of vertically aligned fractures, the effective compliance tensor of fractured rocks can be written as the sum of the compliance tensor of unfractured background rock and the excess compliance tensor induced by fractures (see the appendix 2-A):

$$s_{ijkl} = s_{ijkl}^{b} + s_{ijkl}^{f} . \qquad (1)$$

Assuming the fracture is invariant with respect to the rotation about the axis along the fracture normal direction, the fracture compliance tensor depends on only two fracture compliance tensors: the fracture normal compliance tensor and the tangential compliance tensor (Schoenberg and Sayers, 1995). These two fracture compliance tensors can be related to Hudson's fracture models (1981, 1996), as shown in the appendix. Finally, the fracture compliance tensor can be written as

$$s_{ijkl}^{f} = \frac{\eta}{4\mu}[U_{11}(\delta_{ik}n_i n_j + \delta_{jk}n_l n_i + \delta_{il}n_k n_j + \delta_{jl}n_k n_i) + 4(U_{33} - U_{11})n_i n_j n_k n_l] \qquad (2)$$

where η is the fracture density, which is equal to the number density (the number of fractures per unit volume) times the cube of the average radius of a circular shaped crack, and μ is a Lame parameter of unfractured rocks. Expressions for U_{11} and U_{33} are given by Hudson (1981) for fluid-filled cracks.

$$U_{11} = \frac{16}{3}\left(\frac{\lambda + 2\mu}{3\lambda + 4\mu}\right)(1 + M)^{-1} \tag{3a}$$

where

$$M = \frac{4}{\pi}\left(\frac{a\mu'}{c\mu}\right)\left(\frac{\lambda + 2\mu}{3\lambda + 4\mu}\right) \quad , \tag{3b}$$

and

$$U_{33} = \frac{4}{3}\left(\frac{\lambda + 2\mu}{\lambda + \mu}\right)(1 + K)^{-1} \tag{4a}$$

where

$$K = \frac{1}{\pi}\frac{a\left(\kappa' + \frac{4}{3}\mu'\right)}{c\mu}\left(\frac{\lambda + 2\mu}{\lambda + \mu}\right) \quad , \tag{4b}$$

where c/a in equations 3b and 4b is the crack aspect ratio (fracture shape), λ and μ are Lame parameters of unfractured rocks, λ' and μ' (μ'=0 for non-viscous fluid) are Lame parameters of the fluid content. U_{11} and U_{33} are the displacement discontinuities generated by the response of a circular crack to shear and normal stresses, respectively. The elastic stiffness tensor can be obtained by inverting the compliance tensor calculated in equation (1).

Based on equations (2), (3) and (4), the seismic anisotropy is a function of fracture density, fluid content and crack aspect ratio (crack shape) (denoted as fracture parameters). With an increase in fracture density, the increasing of the fracture compliance tensor leads to a decrease in the elastic stiffness tensor of a fractured medium. In fluid saturated fractures, M vanishes due to the zero shear modulus of the fluid (equation 3b). The discontinuity in transverse displacement, U_{11}, is a function of the Lame parameters of unfractured rocks alone. Fluid bulk modulus affects the discontinuity in normal displacement, U_{33}, through K (equation 4a). Therefore, characteristics of P- and S-wave seismic anisotropy are different in fluid-saturated, fractured rocks.

When the wave propagates through a vertically aligned fractured reservoir, shear wave splitting is observable. The split shear waves are denoted as "$S_{\parallel}$" and "$S_{\perp}$". Fracture

parameters only alter the properties of body waves with particular displacement (polarizations) that intersect the faces of the cracks. The shear mode $S_{||}$, the fast shear wave with polarization parallel to fracture strike plane, propagates at the velocity of the unfractured rock. The shear model $S_{\perp}$, the slow shear wave with polarization perpendicular to the fracture strike plane, propagates at the velocity of the fractured rock. Crampin et al. (1986) show that, to the first order, the group velocities of qP and $S_{\perp}$ vary with fracture density alone and have 2θ variations and that, in water-saturated fractures, in addition to the effect of fracture density, crack aspect ratio also has an important effect on qP-wave group velocities and that $S_{\perp}$ group velocities. Recent studies from Thomsen (1995) show that the angular dependence of qP-wave phase velocity is qualitatively dependent on the aspect ratio and that of the angular dependence $S_{\perp}$ phase velocity is quantitatively dependent on the aspect ratio. The difference in velocity variations in water-saturated, fractured rocks can be attributed to the fact that water has a larger bulk modulus than gas. The effect of crack aspect ratio is often coupled with fluid bulk modulus as shown by equation (4b).

Thomsen (1995) gives a much stronger condition, with the approximation of $c/s \leq \frac{1}{30}$, than is usually understood by the term 'thin crack'. Nevertheless, by using Hudson's theory (1981), Crampin et al. (1986) show that the overall patterns of velocity variations for large crack densities and large aspect ratios will be similar to the patterns of variations for smaller crack densities and aspect ratios.

2.3.2 Effects of fracture parameters on properties of anisotropic parameters and P-wave NMO velocities

In exploration geophysics, the velocity that can be measured from surface seismic data is normal moveout (NMO) velocity. To understand the effect of fracture parameters on NMO velocities, we need to understand effects of fracture parameters on anisotropic parameter properties. Studies find that the generic Thomsen notation is not well suited to describe normal-moveout velocities in transversely isotropic media with a horizontal symmetry axis (HTI media), and that NMO and AVO in HTI media are best described by adapting Thomsen's notation for transversely isotropic media with a vertical symmetry axis (VTI media) (Tsvankin, 1996; Ruger and Tsvankin, 1997). Tsvankin (1996) intro-

duces another set of dimensionless anisotropic parameters of the equivalent VTI model that are more convenient in characterizing moveout velocities for HTI media than generic Thomsen parameters. These parameters (denoted with the superscript v) are represented through the stiffness coefficient C_{ij}. Thus, the five elastic stiffness coefficients can be replaced by

$$\delta^{(v)} = \frac{(C_{13} + C_{55})^2 - (C_{33} - C_{55})^2}{2C_{33}(C_{33} - C_{55})} \quad , \tag{5}$$

$$\varepsilon^{(v)} = \frac{C_{11} - C_{33}}{2C_{33}} \quad , \tag{6}$$

$$\gamma^{(v)} = \frac{C_{66} - C_{44}}{2C_{44}} \quad , \tag{7}$$

$$V_{P\ vert} = \sqrt{\frac{C_{33}}{\rho}} \quad , \tag{8}$$

and

$$V_{S_{\perp vert}} = \sqrt{\frac{C_{55}}{\rho}} \tag{9a}$$

or

$$V_{S||vert} = \sqrt{\frac{C_{44}}{\rho}} = \frac{V_{S_\perp}}{\sqrt{1 + 2\gamma^{(v)}}} \quad . \tag{9b}$$

$\delta^{(v)}$ is responsible for near-vertical P-wave velocity variations in the crack normal direction. $\varepsilon^{(v)}$ defines so called the "P-wave anisotropy". $\delta^{(v)}$ and $\varepsilon^{(v)}$ are typically negative in HTI media. $\gamma^{(v)}$ is the shear-wave splitting parameter which governs the degree of shear-wave splitting at vertical incidence.

The equation for $\delta^{(v)}$ [equation (5)] can be rewritten in terms of $Vp/V_{S\perp}$ and the ratio

C_{13}/C_{55}, by dividing each term at the right side of equation (5) by C_{55}. We have

$$\delta^{(v)} = \frac{\left(\frac{C_{13}}{C_{55}}+1\right)^2 - \left(\left(\frac{V_{Pvert}}{V_{S_{\perp vert}}}\right)^2 - 1\right)^2}{2\left(\frac{V_{Pvert}}{V_{S_{\perp vert}}}\right)^2\left(\left(\frac{V_{Pvert}}{V_{S_{\perp vert}}}\right)^2 - 1\right)} \quad . \tag{10}$$

Equation (10) shows that $\delta^{(v)}$ is the function of $Vp_{vert}/V_{S\perp}$ and C_{13}/C_{55}. Since fluid content has a more significant effect on C_{13}/C_{55} than $Vp_{vert}/V_{S\perp}$, $\delta^{(v)}$ has different characteristics in gas- and water-saturated, fractured rocks. The elastic parameters of five sandstones, summarized in Table 1 and two aspect ratios, 0.01 and 0.05, are used in our calculations. $\delta^{(v)}$ as a function of fracture density in gas- and water-saturated, fractured sandstones is shown in Figure 2-1. With gas-saturated fractures, the five sandstones have approximately the same negative $\delta^{(v)}$ values that vary with the crack density alone and are insensitive to the aspect ratio. However, with water-saturated fractures, absolute values of $\delta^{(v)}$ increase with fracture density and crack aspect ratio. We also note that $\delta^{(v)}$ is dependent on Vp/Vs of isotropic, unfractured sandstones. The smaller the Vp/Vs, the larger the absolute value of $\delta^{(v)}$ obtained. This may be explained by the fact that C_{13}/C_{55} is more dependent on Vp/Vs in water-saturated fractures than in gas-saturated ones, so the Vp/Vs of the isotropic background medium indirectly affects $\delta^{(v)}$. Gas-saturated, fractured sandstone has a larger absolute value of $\delta^{(v)}$ than water-saturated sandstone.

$\varepsilon^{(v)}$ shows similar characteristics to $\delta^{(v)}$. The difference is that $\varepsilon^{(v)}$ is the function of the Vp of the background medium. In gas-saturated, fractured sandstones, $\varepsilon^{(v)}$ is sensitive to fracture density alone. In water-saturated, fractured sandstone the absolute value of $\varepsilon^{(v)}$ increases with both fracture density and aspect ratio. The smaller the Vp, the smaller the absolute value $\varepsilon^{(v)}$ obtained. $\varepsilon^{(v)}$ as a function of crack density and aspect ratio in gas- and water-saturated, fractured sandstones is shown in Figure 2-2.

Parameter $\gamma^{(v)}$ is different from both $\delta^{(v)}$ and $\varepsilon^{(v)}$ in that it measures the degree of shear wave splitting at vertical incidence. The calculated $\gamma^{(v)}$ shows that it has little dependence on fluid bulk modulus and crack aspect ratio (Figure 2-3) and is the parameter most

directly related to fracture density. Therefore, for parallel, penny-shaped cracks, the shear wave splitting parameter, $\gamma^{(v)}$, can provide direct information about fracture density with smaller ambiguity than other two anisotropic parameters, $\varepsilon^{(v)}$ and $\delta^{(v)}$.

The effect of fractures on NMO velocities is studied based on the equation for the normal moveout velocity for horizontal reflection in HTI media derived by Tsvankin (1997):

$$V_{nmo}^2 = V_{Pvert}^2 \frac{1+A}{1+A(\sin\alpha)^2} \qquad (11)$$

where

$$A[P-wave] = 2\delta^{(v)}, \qquad (12)$$

where α is the azimuth of the CMP line with respect to the symmetry axis, and A is an anisotropic term. Equation (11) is valid for HTI media with any strength of anisotropy and can be used for all three pure modes (P, $S_{||}$, and $S_{\perp}$). P-wave NMO velocity is determined by vertical P-wave velocity, principal crack orientation and the parameter $\delta^{(v)}$. Grechka and Tsvankin (1998) show that the azimuthal variation of NMO velocity represents an ellipse in the horizontal plane, with the orientation of the axes determined by the properties of the medium and the direction of the reflection normal. A minimum of three azimuthal measurements is needed to make the best-fit ellipse and obtain NMO velocity in any azimuth direction. As mentioned above, the parameter $\delta^{(v)}$ is typically negative in HTI media, any NMO velocities in off fracture strike directions are smaller than the vertical P-wave velocity, while the NMO velocity in the crack strike direction is the same as the vertical P-wave velocity because there is no fracture influence. Therefore, the orientation of the long axis in NMO velocity ellipse indicates the principal orientation of fractures.

Since the P-wave NMO velocity is directly affected by $\delta^{(v)}$, the NMO velocity is expected to have similar properties to $\delta^{(v)}$. The larger the negative $\delta^{(v)}$, the smaller the NMO velocities obtained in off fracture strike directions. Parameters of fives sandstones in Table 1 with 10% crack density are used in the estimation of NMO velocities. Figure 2-4 shows that, in gas-saturated, fractured sandstones, P-wave NMO velocities are insensitive to crack aspect ratio and are controlled by fracture density alone and that, in water-saturated, fractured sandstones, P-wave NMO velocities are dependent on the crack aspect

ratio. Therefore, fluid contents still have a great effect on P-wave NMO velocities. Because $\delta^{(v)}$ has a large absolute value in gas-saturated, fractured sandstone, the NMO velocity ellipses in gas-saturated, fractured sandstones are more elliptical than those in water-saturated, fractured sandstones. This result suggests that azimuthal NMO velocity variations are more easily detected in gas-saturated, fractured reservoirs than in water-saturated, fractured ones.

As mentioned above, the relationship between $\delta^{(v)}$ and fracture density is complicated which makes the inversion of fracture density from $\delta^{(v)}$ ambiguous. Tsvankin (1997) discussed the possibility of obtaining the fracture density through shear-wave splitting parameters by using the NMO velocities of P- and $S_{\perp}$-waves to obtain the information about fracture density.

2.4 EFFECTS OF BACKGROUND MEDIA ON P-WAVE AZIMUTHAL AVO RESPONSES

It is known that if anisotropy, caused by vertically aligned fractures, is present on either side of the reflecting boundary, reflection at an interface has an azimuthal variation for a certain range of incident angles. Koefoed (1955) indicates that the reflectivity of plane longitudinal waves incident at oblique angles on boundaries is strongly influenced by the values of the Poisson's ratio of the two media. The approximate expression for the P-wave reflection coefficient in isotropic media, derived by Shuey (1985), shows that near normal incidence seismic data provides information about the change in acoustic impedance between adjacent layers and that large offset seismic data provides information about the contrast in Poisson's ratio across an interface. The anisotropy induced by fractures has an angular dependence effect on amplitudes. Its important influence is the distortion of AVO gradients. Therefore, the elastic properties controlling the AVO gradient of isotropic background rocks, i.e. contrast in Poisson's ratio, would be one factor significantly effecting the azimuthal AVO signatures of fractured reservoirs. If a transversely isotropic medium with a vertical axis of symmetry (VTI) overlies a fractured reservoir, the influence of the anisotropy on wave propagation to and from a reflector may have a direct influence on the character of AVO anomalies. AVO signatures (e.g., AVO gradient) in

anisotropic media are distorted by the redistribution of energy along the wavefront of the wave traveling down to the reflector and back up to the surface (Tsvankin, 1995). To understand the effects of isotropic background media, fracture parameters and overburden anisotropy on azimuthal AVO response, we use 3-D finite difference modeling to compute synthetic seismograms and analyze the P-wave azimuthal AVO variations at the tops of fractured reservoirs.

The 3-D time domain, staggered grid finite difference method is used to obtain accurate seismograms in this chapter. This method has fourth-order accuracy in space and second-order accuracy in time (Cheng et al., 1995). Seismograms with azimuth 0^o (crack normal direction), 45^o and 90^o (strike direction) are considered. The minimum offset is 0 and the maximum offset is approximated to a 30^o incident angle. An explosive source is used, and the dominant frequency of the source wavelet is 45Hz. All edges of the grid have absorbing boundary conditions to suppress artificial reflections.

2.4.1 Effects of elastic properties in background media on P-wave azimuthal AVO variations

In order to compare modeled results, we use two isotropic models with different elastic property contrasts, whose isotropic background parameters (Vp, Vs and ρ) are listed in Table 2. Model 1 has a large Poisson's ratio contrast and corresponds to an isotropic shale, Mesaverde, over a fractured sandstone, Taylor. Elastic properties are taken from the table published by Thomsen (1986). Model 2 has a weak Poisson's ratio contrast and corresponds to an isotropic shale over a fractured sandstone. Elastic parameters are adapted from laboratory measurements (Teng and Mavko, 1996). The fractured sandstones in the two models are assumed to be gas-saturated, with the same fracture density (10%) and the same crack aspect ratio (0.01). The elastic stiffness tensors are obtained by inverting the compliance tensors calculated from equations (1) through (4), which are summarized in Table 3.

Azimuthal AVO variations are expected to occur at the tops of fractured reservoirs. Peak to peak amplitudes are obtained from seismograms generated by 3-D finite difference modeling. We use the same definition as Kim et al. (1993) to define AVO response as the absolute value of the difference between amplitude at a certain incidence and that at

normal incidence; i.e. $|A(\theta)-A(0)|$. The P-wave AVO responses for two models at three azimuths are shown in Figure 2-5. AVO curves in model 1 with large Poisson's ratio contrast show hardly any azimuthal variations and almost coincide at 0^o, 45^o, and 90^o (Figure 2-5a). However, in model 2 with weak Poisson's ratio contrast, reflection amplitude curves show obvious azimuthal variations and are well separated at three azimuths (Figure 2-5b). The highest rate of decrease of reflection amplitudes with offset (AVO gradient) is in the crack normal direction (azimuth 0^o), and the lowest rate is in the crack strike direction (azimuth 90^o). Azimuthal AVO variations can be observed in model 2 when the incident angle is larger than 7^o. Results indicate that, in model 2, the presence of fractures causes apparent anisotropic behavior in the P-wave reflection amplitudes.

Although the two fractured reservoirs have the same crack parameters (density, fluid content and crack aspect ratio), they show different P-wave azimuthal AVO response. We also note that model 1 has a larger AVO gradient (the rate of amplitudes varying with offset) than model 2 in the crack strike direction due to its large Poisson's ratio contrast. The difference in azimuthal AVO responses of the two models can be attributed to the difference in elastic properties of isotropic background media. Numerical results reveal that azimuthal variations of P-wave AVO are not necessarily correlated with the magnitude of fracture density and cannot be related simply to the strength of anisotropy. Their visibility could be masked by background AVO response.

Numerical modeling provides the straight forward and accurate overall azimuthal AVO response. To gain insight into anisotropic reflectivity and to understand relative contributions of anisotropy to overall azimuthal AVO response, we use approximated analytic solutions to calculate azimuthal reflection coefficients. An exact generalization of Zoeppritz equations to elastic VTI media was presented by Daley and Hron (1977). Banik (1987) simplified their expression for reflection coefficients by linearizing it in terms of elastic parameters. More recently, Daley and Hron's expression for the P-P reflection coefficient between two elastic VTI media have been reduced by Thomsen (1993). Based on Thomsen's work, Ruger (1995) obtains the P-wave reflectivity formulas for HTI media by adding symmetry conditions. The P-wave reflection coefficient in HTI media at an arbitrary azimuth is given by Ruger (1998) and can be written as follows:

$$R_p(i,\phi) = \frac{1}{2}\left(\frac{\Delta V_p}{V_p} + \frac{\Delta\rho}{\rho}\right) + \frac{1}{2}\left(\frac{\Delta V_p}{V_p}\sin^2 i\right) - 2\left(\frac{V_s}{V_p}\right)^2\left(\frac{\Delta\rho}{\rho} + 2\frac{\Delta V_s}{V_s}\right)\sin^2 i +$$
$$\frac{1}{2}\frac{\Delta V_p}{V_p}\sin^2 i\tan^2 i + \frac{1}{2}\Delta\delta^{(v)}\sin^2 i\cos^2\phi + 4\left(\frac{V_s}{V_p}\right)^2\Delta\gamma\sin^2 i\cos^2\phi +$$
$$\frac{1}{2}\Delta\varepsilon^{(v)}\sin^2 i\tan^2 i\cos^4\phi + \frac{1}{2}\Delta\delta^{(v)}\sin^2\phi\cos^2\phi\sin^2 i\tan^2 i \qquad (13)$$

where

$$\gamma = -\frac{\gamma^{(v)}}{1+2\gamma^{(v)}}$$

and $\Delta\rho$, ΔVp, and ΔVs refer to contrasts of rock density, P-wave velocity, and S-wave velocity across the reflection boundary, respectively. ρ, Vp, and Vs are averages. $\Delta\varepsilon^{(v)}$ and $\Delta\delta^{(v)}$ are contrasts of anisotropic parameters of the equivalent VTI model. $\Delta\gamma$ can be expressed through the equivalent VTI parameter $\Delta\gamma^{(v)}$. Anisotropic parameters can be calculated by using equations (1) through (4) and (5) through (9), which are listed in Table 3. i and ϕ denote the incident phase angle and azimuthal phase angle, respectively. The terms in equation (13) without anisotropic parameters represent the reflected coefficients generated by isotropic background rocks. The rest of the terms in equation (13) with anisotropic parameters represent the reflected coefficients induced by fractures. It can be understood that azimuthal AVO variation depends on the relative contributions by reflection coefficients generated by anisotropy. Equation (13) also shows that the anisotropic parameters are modified not only by incident phase angle but also by azimuthal phase angle. Therefore, the effect of fractures on reflected coefficients is a function of these two angles.

Reflection coefficients for model 1, generated by fractures only (defined as fracture-induced reflection coefficients) and by both isotropic background rocks and fractures (defined as overall reflection coefficients), as a function of the incident angle and azimuth are shown in Figures 2-6a and 2-6b, respectively. The same results for model 2 are shown in Figures 2-7a and 2-7b. Both Figures 2-6a and 2-7a show that fracture-induced reflection coefficients increase with increasing incident angle. The AVO gradients increase from zero in the crack strike direction to their maximum in the crack normal direction. How-

ever, the overall reflection coefficients versus the incident angle and the azimuth have different variation patterns from fracture-induced reflection coefficients in the two models. Figure 2-6b shows that overall AVO gradients have little variation from the fracture strike direction to the fracture normal direction. On the other hand, in Figure 2-7b, AVO gradients of overall reflection coefficients vary with the azimuth and the highest gradient is in the crack normal direction. The overall AVO curves in model 2 are displaced upward with increasing incident angle in non-fracture-strike directions. Figure 2-7b also demonstrates that fracture-induced reflection coefficients generate a noticeable perturbation in the overall reflection coefficients. Results from numerical modeling and analytical solutions are qualitatively consistent with each other. Therefore, although P-wave azimuthal AVO variations could be an effective tool in fracture detection, fracture induced azimuthal AVO variations cannot always be observable in overall azimuthal AVO variations. Elastic properties of isotropic background rocks have an important effect on the visibility of the overall azimuthal AVO responses.

2.4.2 Effects of the fluid content and the fracture density on P-wave azimuthal AVO variations

To investigate the effects of fluid content on P-wave azimuthal AVO responses, the 3-D finite difference modeling technique is also used to calculate the azimuthal AVO response at the tops of water-saturated, fractured reservoirs. We use the same isotropic background models (model 1 and model 2), fracture density, and crack aspect ratio as those in the modeling of gas-saturated, fractured reservoirs. The only difference in modeling is changing the fluid content from gas to water. The azimuthal AVO responses at the tops of water-saturated, fractured reservoirs are shown in Figures 2-8a and 2-8b, respectively. In model 1, azimuthal AVO response cannot be observed at the water-saturated, fractured reservoir top, while results from model 2 has more noticeable azimuthal AVO variations than those in gas-saturated, fractured reservoirs as shown in Figure 2-5b. AVO gradients in crack normal and azimuth 45^0 directions in Figure 2-8b become larger than those in Figure 2-5b.

Absolute values of $\delta^{(v)}$ and $\varepsilon^{(v)}$ become small in water-saturated, fractured reservoirs, while γ has positive values and is insensitive to fluid contents. Since anisotropic parame-

ters, $\delta^{(v)}$ and γ, have the first order influence on AVO gradients and $\varepsilon^{(v)}$ dominates only at large incident angles, varying the saturated fluid content can result in the variation of $\delta^{(v)}$ and $\varepsilon^{(v)}$. Therefore, the enlarged azimuthal AVO variations can be attributed to the fact that small values of anisotropic parameters, $\delta^{(v)}$ and $\varepsilon^{(v)}$, lead to an increase in the positive, fracture-induced reflection coefficients and that the contribution of anisotropy to the azimuthal overall azimuthal variations becomes large.

By changing the fracture density, we model the azimuthal AVO responses in the water-saturated, fractured reservoir of model 2. We find that, with increasing fracture density, AVO gradients increase in non-fracture-strike directions followed by obvious P-wave reflection anisotropic behavior.

As mentioned above, the azimuthal AVO variations can be increased by changing fluid contents. The numerical results indicate that increasing fracture density can generate the same physical phenomena. Although the large azimuthal AVO variation is helpful in detecting fractures, the interpretation of fracture density by using this signature alone is ambiguous. Therefore, the alternative P-wave seismic signature, NMO velocity, would be very useful in lessening the ambiguity in interpreting fracture density and in discriminating fluid contents.

2.4.3 Effects of transversely isotropic shale on P-wave azimuthal AVO response

In our previous modeling, the overlying shale is assumed to be isotropic. If the upper shale is a transversely isotropic medium with a vertical axis, P-wave AVO responses would be affected. The influence of transverse isotropy on the P-wave reflection coefficient at the tops of isotropic gas-saturated sands are discussed by Kim et al. (1993) and Blangy (1994). In this chapter, we investigate the effect of overburden anisotropy of VTI media on azimuthal AVO variations at the top of fractured reservoirs. In this study, we use the same isotropic background models, fracture density, and fracture aspect ratio as those in our previous modeling. The fractured reservoirs are water-saturated. The overburden shale is a transversely isotropic medium with a vertical axis rather than an isotropic medium.

Five independent elastic coefficients, needed to describe the vertically transverse isot-

ropy (C_{11}, C_{33}, C_{44}, C_{66} and C_{13}), can be replaced by vertical velocities Vp_0 and Vs_0, and three dimensionless anisotropic parameters, ε, δ, and γ (Thomsen, 1986). In our modeling, the anisotropic parameters for the overlying shale are taken from Thomsen's (1986) table for oil shale, ε=0.20, δ=0.10, and γ=0.145. Clearly, the introduction of ε, δ, and γ in overlying shale changes the contrasts of anisotropic parameters across the interface of reflection.

The azimuthal AVO responses with the overlying anisotropic shale for the two water-saturated, fractured reservoir models are shown in Figures 2-9a and 2-9b. Compared with Figure 2-8a, overburden anisotropy does not show a significant effect on azimuthal AVO response of model 1 because of its significant contrasts in isotropic elastic properties (Poisson's ratio contrast) (Figure 2-9a). However, Figure 2-9b is different from Figure 2-8b, which shows that AVO gradients increase in three azimuths and that the effects of overlying anisotropy become pronounced from moderate to larger incident group angles. As mentioned above, in anisotropic media, the overall reflection coefficient is the sum of the reflection coefficient from isotropic background rocks and from the anisotropy contained in background rocks. The contribution of transverse isotropy with a vertical axis to P-wave kinematic and dynamic signatures is controlled by just two anisotropic parameters, ε and δ and the influence of overburden anisotropy is controlled mostly by the difference between the anisotropic parameters, ε and δ, in VTI media (Tsvankin, 1995). The variations of AVO gradients can be explained by the fact that adding oil shale anisotropy varies the contrasts of these two anisotropic parameters across the reflection boundary. The numerical results show that both the overburden anisotropy and the fracture-induced anisotropy can lead to variations in AVO gradients. Therefore, the interpretation of crack density based on the individual azimuthal AVO gradient can be biased without considering the effect of overburden anisotropy.

However, some differences between the effect of overburden anisotropy and the effect of vertically aligned fractures should be pointed out. One is that the effect of transversely isotropic shale with a vertical axis on AVO responses does not vary with azimuth and only varies with incident angle. This characteristic allows us to eliminate the effect of overburden anisotropy by considering the difference in AVO signatures between an arbitrary azimuth and the crack strike direction rather than by inverting parameters from an individual

AVO response, for instance. Another is that the P-wave source produces only P- and SV-waves coupling in a VTI medium, so only the parameters ε and δ are involved and the parameter γ is excluded. This characteristic shows that the parameter γ is still the one most related to the fracture system even with the influence of the overlying anisotropy induced by VTI media. Therefore, γ is the least ambiguous anisotropic parameter for estimating the fracture density. Note that the overburden anisotropy can increase or decrease the AVO gradient depending on the anisotropic parameters. Note also that when the overburden anisotropy is not a VTI medium, as is the case when HTI or orthorhombic media are present, P-wave azimuthal AVO responses in a fractured reservoir would become more complicated.

2.5 DISCUSSION AND CONCLUSIONS

The P-wave seismic signatures given in this chapter include properties of anisotropic parameters of the equivalent VTI model, NMO velocities, and azimuthal AVO variations. To gain insight into the effects of fracture parameters (fracture density, fracture aspect ratio, and saturated fluid content) on these seismic signatures, we model the seismic responses, analyze numerical results, and interpret them with analytic solutions.

If anisotropy is caused by parallel, penny shaped cracks, the anisotropic parameters of the equivalent VTI model are related to the fracture parameters through elastic stiffness tensors of fractured media. The variations of parameters $\delta^{(v)}$ and $\varepsilon^{(v)}$ are sensitive to fluid content. If fractures are gas-saturated, $\delta^{(v)}$ and $\varepsilon^{(v)}$ vary with the fracture density alone; if fractures are water-saturated, the magnitudes of $\delta^{(v)}$ and $\varepsilon^{(v)}$ depend on fracture density, crack aspect ratio, and elastic properties of background rocks. On the other hand, the shear wave splitting parameter, $\gamma^{(v)}$, is insensitive to fluid content and crack aspect ratio. It is the parameter most related to crack density. P-wave NMO velocity is controlled by the vertical P-wave velocity, angle between crack normal and survey line, and the parameter $\delta^{(v)}$. The effects of fracture parameters on NMO velocities is comparable with those on $\delta^{(v)}$.

The azimuthal variation of P-wave reflection amplitudes (coefficients) is an important seismic signature in detecting fractures. Our results show that the P-wave reflection anisotropy caused by fractures does not necessarily correlate with azimuthal AVO variations.

Elastic properties of background rocks influence their visibility. Azimuthal AVO variations can be significant at the tops of fractured reservoirs, which have small Poisson's ratio contrasts in their isotropic background rocks. The approximated analytical solutions indicate that fracture-induced reflection coefficients can make noticeable perturbations in overall reflection coefficients in this kind of fractured reservoir.

Although AVO gradients in off fracture strike directions increase with increasing fracture density, different fluid content (bulk modulus) can also cause variations of AVO gradients in these directions. We also note that the AVO gradient in the crack normal direction is not always larger than that in the crack strike direction, the magnitude of AVO gradients in the two directions also depends on the elastic properties of background rocks. For example, for the fractured reservoir of class 1 gas sandstone, the maximum AVO gradient is in the crack strike direction rather than in crack normal direction (also see results from Sayers and Rickett, 1997).

Azimuthal AVO gradients are also influenced by the overlying anisotropic (VTI) medium. Since this influence does not vary with the azimuth, fracture detection is still valid based on azimuthal AVO variations. However, the inversion of fracture parameters based on an individual, azimuthal AVO response would be distorted without correcting this effect.

Our studies show that though azimuthal AVO variations could be useful for detecting fractures, modeling studies and a combination of different types of data are more beneficial in interpreting the properties of fractured reservoirs than using P-wave reflection amplitudes alone. For example, azimuthal NMO velocity variations are different from azimuthal reflection amplitude variations. In general, azimuthal variations of NMO velocities are elliptic in the horizontal plane. The maximum NMO velocity is always located along the principal crack strike direction. This characteristic is useful in detecting the principal orientation of fractures. NMO velocities can also be combined with azimuthal AVO data to qualitatively interpret the reservoir properties and locate the top and the base of the fractured reservoir. Ruger and Tsvankin (1997) indicate that NMO data together with azimuthal AVO data can be used to estimate the shear wave splitting parameter, γ.

The interpretation of azimuthal variations of amplitudes is reference based because these variations are relative to a fixed, certain azimuth. Therefore, the systematic errors

and non azimuth dependent effects (such as tuning and overlying VTI media) would be eliminated by subtracting the azimuthal attributes. Considering the difference between azimuthal AVO signatures may help us obtain robust, qualitative interpretation of fractured reservoirs. On the other hand, quantitative interpretation would be difficult when using the P-wave seismic signatures alone because of the variables discussed above.

ACKNOWLEDGEMENTS

We thank Enru Liu in British Geological Survey for help discussion and valuable help. We appreciate the help discussion with Dan Burns at M.I.T for help discussion. We acknowledge our reviews, especially our second review, for help comments and recommendations on an earlier draft. This research was supported by the Borehole Acoustics and Logging/Reservoir Delineation Consortium at M.I.T.

REFERENCES

Banik, N. C., 1987, An effective anisotropy parameter in transversely isotropic media, Geophysics, 52, 1654-1164.

Blangy, J. P., 1994, AVO in transversely isotropic media - An overview: Geophysics, 59, 775-781.

Chang, C. H., and Gardner, G. H. F., 1993, Effects of vertically aligned fractures on reflection amplitudes: An Amplitudes-Versus-Offset study, 63rd SEG meeting (Washington D. C.), Expanded Abstracts, 769-771.

Cheng, N., Cheng, C. H., and Toksoz, M. N., 1995, Borehole wave propagation in three-dimensions, J. Acoust. Soc. Am., 97, 3483-3493.

Corrigan, D., Withers, R., Darnall, J., and Skopinski, T., 1996, Fracture mapping from azimuthal velocity analysis using 3-D surface seismic data: 66th Ann. Internat. Mtg., Soc. Expl. Geophys., Expanded Abstracts, 1834-1837.

Crampin, S., McGonigle, R., and Ando, M., 1986, Extensive-dilatancy anisotropy beneath Mount Hood, origin and the effect of aspect ratio on seismic velocities through aligned cracks, J. Geophys. Res., 91, 12703-12710.

Daley, P. T., and Hron, F., 1977, Reflection and transmission coefficients for transversely isotropic media, Bull. Seis. Soc. Am., 67, 661-675.

Grechka, V., and Tsvankin, I., 1998, 3-D description of normal moveout in anisotropic inhomogeneous media, Geophysics, 63, 1079-1092.

Haugen, G., and Ursin, B., 1996, AVO-A analysis of a vertically fractured reservoir underlying shale, 66th Ann. Internat. Mtg., Soc. Expl. Geophys., Expanded Abstracts, 1826-1829.

Hill, R., 1963, Elastic properties of reinforced solid: some theoretical principles, J., Mech. Phys. Solid, 11, 357-352.

Hudson, J. A., 1981, Wave speeds and attenuations of elastic waves in material containing cracks, Geophys. J. Roy. Astr. Soc., 64, 133-150.

Hudson, J. A., Liu, E., and Crampin, S., 1996, Transmission properties of a plan fault, Geophys. J. Int., 125, 559-566.

Kim, K. Y., Wrolstad, K. H., and Aminzadeh, F., 1993, Effects of transverse isotropy on P-wave AVO for gas sands, Geophysics, 58, 883-888.

Liu, E., MacBeth, C., Point, C., and Hudson, J. A., 1996, The effective elastic compliance of fractured rock, 66th Ann. Internat. Mtg., Soc. Expl. Geophys., Expanded Abstracts, 1842-1845.

Koefoed, O., 1955, On the effect of Poisson's ratios of rock strata on the reflection coefficients of plane waves, Geophysical Prospecting, 3, 381-387.

Lynn, H. B., Bates, C. R., Simon, K. M., and van Dok, R., 1995, The effects of azimuthal anisotropy in P-wave 3-D seismic, 65th Ann. Internat. Mtg., Soc. Expl. Geophys., Expanded Abstracts, 723-730.

Lynn, H. B., Simon, K. M., and Bates, C. R., 1996, Correlation between P-wave AVOA and S-wave traveltime anisotropy in a naturally fractured gas reservoir, The Leading Edge, 15, 931-935.

Mallick, S., and Frazer, L. N., 1991, Reflection/transmission coefficients and azimuthal anisotropy in marine seismic studies, Geophys. J. Int., 105, 241-252.

Mallick, S., Craft, K. L., Meister, L. J., and Chambers, R. E., 1998, Determination of the principal directions of azimuthal anisotropy from P-wave seismic data, Geophysics, 63, 692-706.

Paul, R. J., 1993, Seismic detection of overpressure and fracturing: an example from the Qaidam Basin, People's Republic of China, Geophysics, 58, 1532-1543.

Ramos, A. C. B., and Davis, T. L., 1997, 3-D AVO analysis and modeling applied to fracture detection in coalbed methane reservoirs, Geophysics, 62, 1683-1695.

Ruger, A., 1995, P-wave reflection coefficients for transversely isotropic media with vertical and horizontal axes of symmetry: 65th Ann. Internat. Mtg., Soc. Expl. Geophys., Expanded Abstracts, 278-281.

Ruger, A., 1998, Variation of P-wave reflectivity with offset and azimuth in anisotropic media, Geophysics, 63, 935-947.

Ruger, A., and Tsvankin, I., 1997, Using AVO for fracture detection: Analytic basis and practical solutions, The Leading Edge, 16, 1429-1434.

Sayers, C. M., and Ebrom, D. A., 1997, Seismic Traveltime analysis for azimuthally anisotropic media: Theory and experiment, Geophysics, 62, 1570-1582.

Sayers, C. M., and Kachanov, M., 1995, Microcrack-induced elastic wave anisotropy of brittle rocks, J. Geophys. Res., 100, 4149-4156.

Sayers, C. M., and Rickett, J., 1997, Azimuthal variation in AVO response for fractured gas sands, Geophysical Prospecting, 45, 165-182.

Schoenberg, M., and Sayers, C. M., 1995, Seismic anisotropy of fractured rock, Geophysics, 60, 204-211.

Shuey, R. T., 1985, A simplification of the Zoeppritz equations, Geophysics, 50, 609-614.

Teng, L., and Mavko, G., 1996, Fracture Signatures on P-wave AVOZ, 66th Ann. Internat. Mtg., Soc. Expl. Geophys., Expanded Abstracts, 1818-1821.

Thomsen, L., 1986, Weak elastic anisotropy, Geophysics, 51, 1954-1966.

Thomsen, L., 1988, Reflection seismology over azimuthally anisotropic media, Geophysics, 53, 304-313.

Thomsen, L., 1993, Weak anisotropic coefficients, in Castagna, J., and Backus, M., eds., Offset dependent reflectivity, Soc. Expl. Geophys.

Thomsen, L., 1995, Elastic anisotropy due to aligned cracks in porous rock, Geophysical Prospecting, 43, 805-829.

Tsvankin, I., 1995, Body wave radiation patterns and AVO in transversely isotropic media, Geophysics, 60, 1409-1425.

Tsvankin, I., 1996, P-wave signatures and notation for transversely isotropic media: An overview, Geophysics, 61, 467-483.

Tsvankin, I., 1997, Reflection moveout and parameter estimation for horizontal transverse isotropy, Geophysics, 62, 614-629.

Appendix 2-A: Estimation of the fracture compliance tensor

Using average strain concepts (Hill, 1963), Sayers and Kachanov (1995) and Schoenberg and Sayers (1995) present a method of estimating the effective elastic modulus for fractured media.

$$\varepsilon_{ij} = \left(s_{ijkl}^{\ b} + s_{ijkl}^{\ f}\right)\sigma_{kl} \qquad \text{(A-1)}$$

where ε_{ij} is the average strain tensor over a representative volume V; $s_{ijkl}^{\ b}$ is the compliance tensor of the unfractured background rock; $s_{ijkl}^{\ f}$ is the excess compliance tensor induced by fractures, and σ_{kl} is the average stress tensor. The excess strain tensor is defined by

$$s_{ijkl}^{\ f}\sigma_{kl} = \frac{1}{2V}\left(\sum_{r=1}^{N^f}\int_{S_r}([u_i]n_j + [u_j]n_i)\right)dS \qquad \text{(A-2)}$$

where $[u_i]$ and $[u_j]$ are the ith and jth components of the displacement discontinuity on the fracture surface, respectively, S_r is the surface of the rth fracture lying within V, and n_i and n_j are the components of the local unit normal to the surface, S. If we assume all fractures in V are identical with each having a surface area S, a linear slip boundary condition given by Liu et al. (1996) is:

$$[u_i] = Z_{ip}\sigma_{pq}n_q \ . \qquad \text{(A-3)}$$

Inserting (A-3) into (A-2), we can obtain

$$s_{ijkl}^{\ f}\sigma_{kl} = \frac{N^f S}{4V}(Z_{ip}n_q n_j + Z_{jp}n_q n_i)(\delta_{pk}\delta_{ql} + \delta_{pl}\delta_{qk})\sigma_{kl} \ . \qquad \text{(A-4)}$$

Assuming the fracture is invariant with respect to the rotation about the axis along the fracture normal direction, the fracture behavior can be described by the fracture normal compliance tensor (Z_N) and tangential compliance tensor (Z_T) (Schoenberg and Sayers, 1995) as

$$Z_{ij} = Z_T \delta_{ij} + (Z_N - Z_T) n_i n_j . \tag{A-5}$$

Liu et al. (1996) have shown that several different fracture models can be cast into a unified equivalent form, including fractures modeled as a planar distribution of small isolated areas of slip, as a distribution of imperfect facial contacts, and as thin, continuous layers filled with soft material. For anisotropy caused by penny-shaped, aligned fractures, the compliance tensors can be written as the following, based on Hudson et al. (1996) and Liu et al. (1996):

$$Z_T = \frac{\Upsilon a^3}{\mu} U'_{11} \tag{A-6a}$$

$$Z_N = \frac{\Upsilon a^3}{\mu} U'_{33} \tag{A-6b}$$

where γ is the number of elementary fractures per area, and a is the average radius of a circular shaped crack. Inserting (A-5) and (A-6) into (A-4), we have

$$s_{ijkl}^{f} = \frac{N^f S}{4V}[Z_T(\delta_{ik}n_i n_j + \delta_{jk}n_l n_i + \delta_{il}n_k n_j + \delta_{jl}n_k n_i) + 4(Z_N - Z_T)n_i n_j n_k n_l] \tag{A-7a}$$

and

$$_{ijkl}^{f} = \frac{N^f S \Upsilon a^3}{4V\mu}[U'_{11}(\delta_{ik}n_i n_j + \delta_{jk}n_l n_i + \delta_{il}n_k n_j + \delta_{jl}n_k n_i) + 4(U'_{33} - U'_{11})n_i n_j n_k n_l] \tag{A-7b}$$

η is fracture density and can been proven as the following:

$$\eta = \frac{N^f S \Upsilon a^3}{4V} = \frac{N^f S a^3}{4V}\frac{N^s}{S} = \frac{N a^3}{V} \tag{A-8}$$

Equation (7b) can be written as

$$s_{ijkl}^{f} = \frac{\eta}{4\mu}[U'_{11}(\delta_{ik}n_i n_j + \delta_{jk}n_l n_i + \delta_{il}n_k n_j + \delta_{jl}n_k n_i) + 4(U'_{33} - U'_{11})n_i n_j n_k n_l] \quad \text{(A-9)}$$

Table 1: Elastic Parameters Of Five Rocks

No. Sandstones	Vp (m/s)	Vs (m/s)	ρ (g/cm^3)	Vp/Vs	references
No. 1	3368	1829	2.50	1.84	Thomsen (1986)
No. 2	4405	2542	2.51	1.73	Thomsen (1986)
No. 3	4539	2706	2.48	1.68	Thomsen (1986)
No. 4	4476	2814	2.50	1.59	Thomsen (1986)
No. 5	4860	3210	2.32	1.51	Teng and Mavko (1996)

Table 2: Elastic Parameters And Fracture parameters of Model 1 and Model 2

Model	Vp (m/s)	Vs (m/s)	ρ (g/cm^3)	Fracture density(%) and aspect ratio	Poisson's ratio	Type Of Rocks
Model 1	4358	3048	2.81		0.021	Mesav-erde Shale
	3368	1829	2.50	10 0.01	0.291	Taylor sandstone
Model 2	4561	2988	2.67		0.124	Shale
	4860	3210	2.32	10 0.01	0.113	Sandstone

Table 3: Fracture Parameters, Elastic Coefficients, and Anisotropic Parameters of Model 1 and Model 2

Fracture Parameters,	Model 1	Model 1	Model 2	Model 2
Elastic Coefficients & Anisotropic Parameters	Mesaverde Shale	Taylor sandstone	Shale	Sandstone
Fracture Density (%)		10		10
Fracture Aspect Ratio		0.01		0.01
Fluid Content		Gas		Gas
C_{11} (GPa)	53.3680	17.2058	55.5433	35.3921
C_{12} (GPa)	1.1565	7.0576	7.8670	4.5123
C_{22} (GPa)	53.3680	26.4821	55.5433	54.4820
C_{13} (GPa)	1.1565	7.0576	7.8670	4.5123
C_{23} (GPa)	1.1565	9.7558	7.8670	6.6710
C_{33} (GPa)	53.3680	26.4821	55.5433	54.4820
C_{44} (GPa)	26.1058	8.3631	23.8381	23.9055
C_{55} (GPa)	26.1058	6.7902	23.8381	18.9362
C_{66} (GPa)	26.1058	6.7902	23.8381	18.9362
$\varepsilon^{(v)}$		-0.175		-0.175
$\delta^{(v)}$		-0.188		-0.184
γ		0.116		0.131

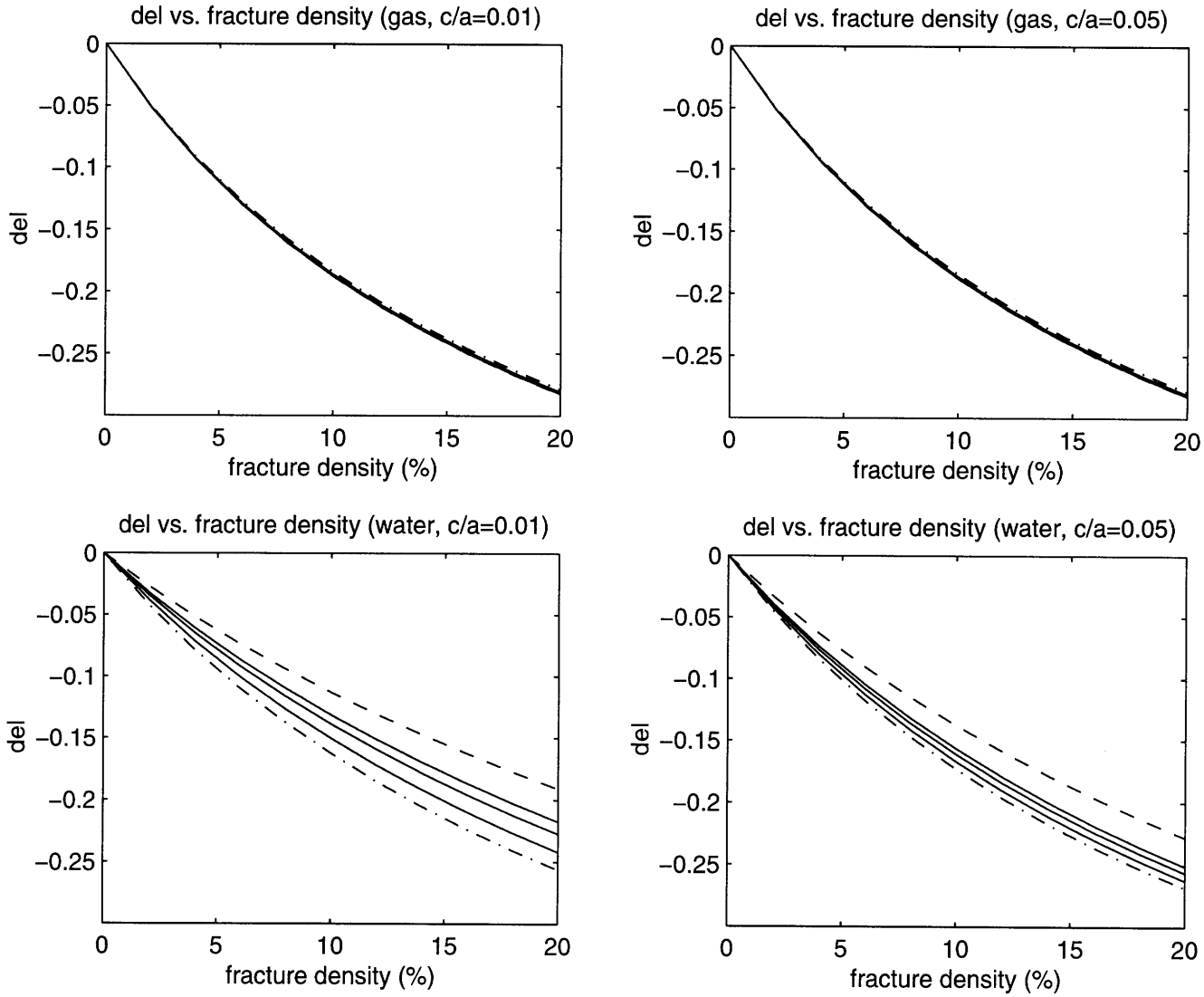

Figure 2-1 The anisotropic parameter $\delta^{(v)}$ varies with fracture density in fractured rocks. (a) in gas-saturated sandstones with fracture aspect ratio 0.01; (b) in gas-saturated sandstones with fracture aspect ratio 0.05; (c) in water-saturated sandstones with fracture aspect ratio 0.01; and (d) in water-saturated sandstones with fracture aspect ratio 0.05. Dash line represents sandstone No.1; solid lines represents sandstone No.2, No3 and No4; solid line with dots represent sandstone No.5.

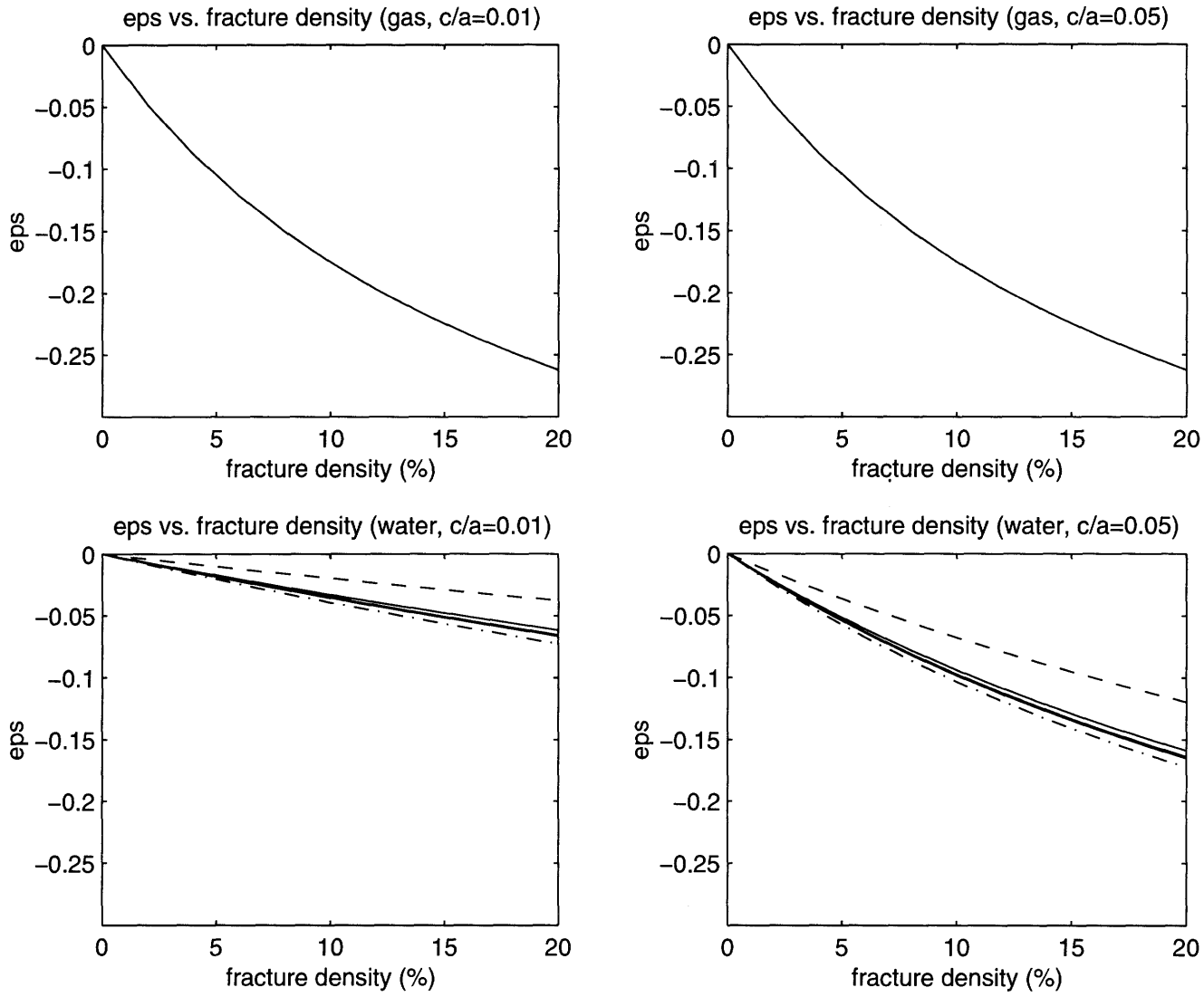

Figure 2-2 The anisotropic parameter $\varepsilon^{(v)}$ varies with fracture density in fractured rocks. (a) in gas-saturated sandstones with fracture aspect ratio 0.01; (b) in gas-saturated sandstones with fracture aspect ratio 0.05; (c) in water-saturated sandstones with fracture aspect ratio 0.01; and (d) in water-saturated sandstones with fracture aspect ratio 0.05. Dash line represents sandstone No.1; solid lines represents sandstone No.2, No3 and No4; solid line with dots represent sandstone No.5.

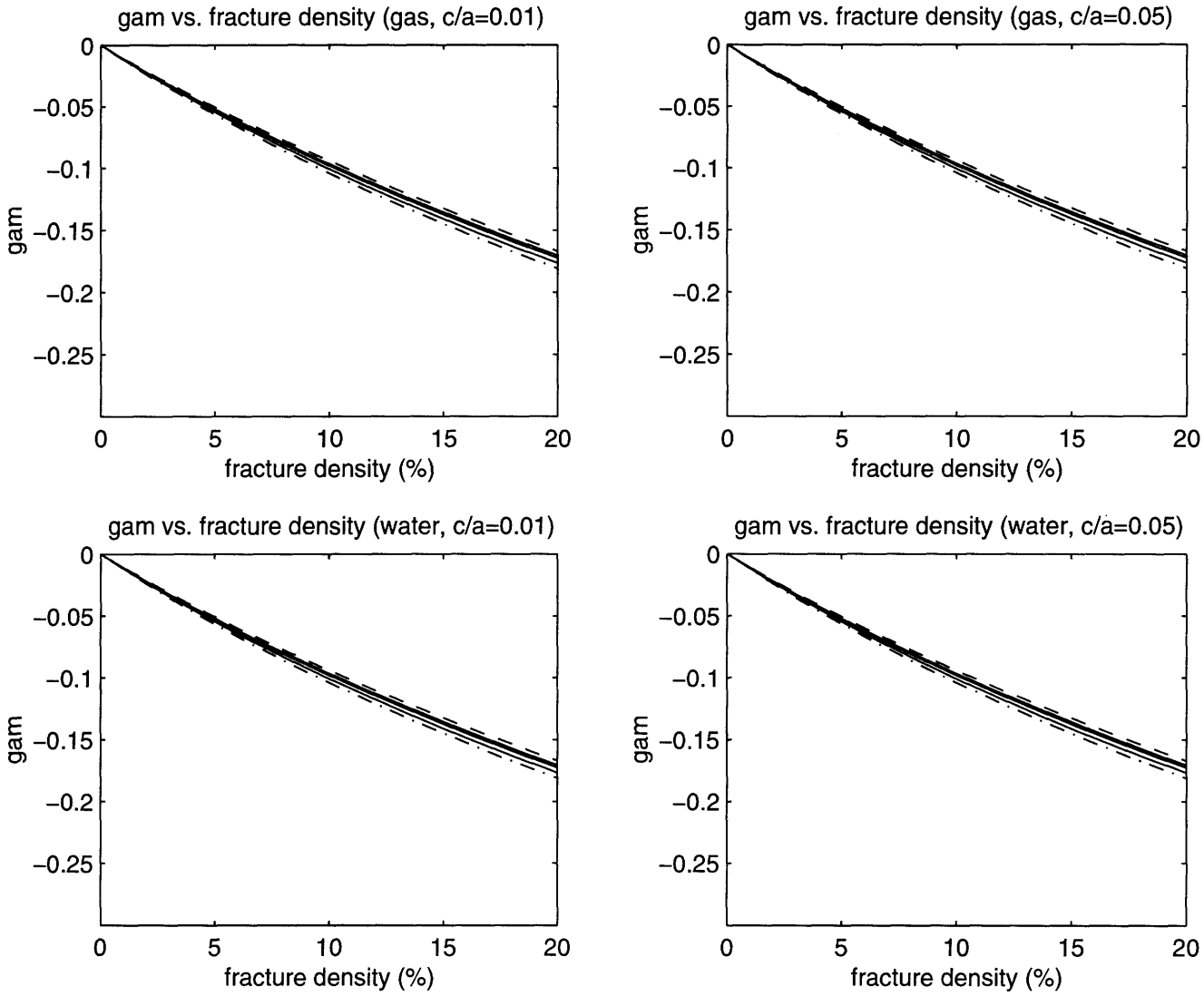

Figure 2-3 The anisotropic parameter $\gamma^{(v)}$ varies with fracture density in fractured rocks. (a) in gas-saturated sandstones with fracture aspect ratio 0.01; (b) in gas-saturated sandstones with fracture aspect ratio 0.05; (c) in water-saturated sandstones with fracture aspect ratio 0.01; and (d) in water-saturated sandstones with fracture aspect ratio 0.05. Dash line represents sandstone No.1; solid lines represents sandstone No.2, No3 and No4; solid line with dots represent sandstone No.5.

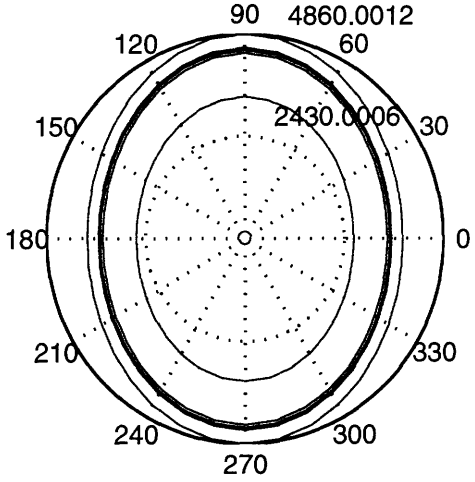

NMO velocity vs. azimuth (gas, c/a=0.001 and 0.05(black lines))

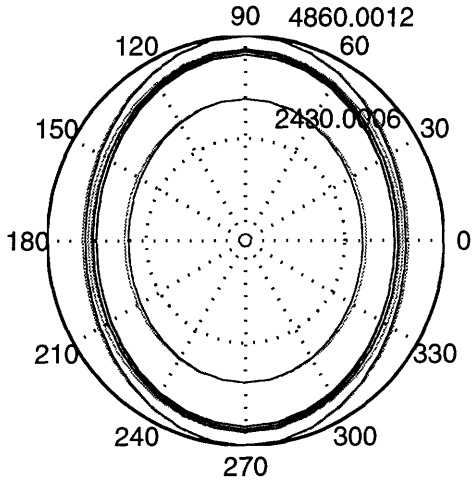

NMO velocity vs. azimuth (water, c/a=0.001 and 0.05(black lines))

Figure 2-4 NMO velocities vary with azimuth. (a) in gas-saturated sandstones with fracture aspect ratio 0.01 and 0.05; (b) in water-saturated sandstones with fracture aspect ratio 0.01 and 0.05.

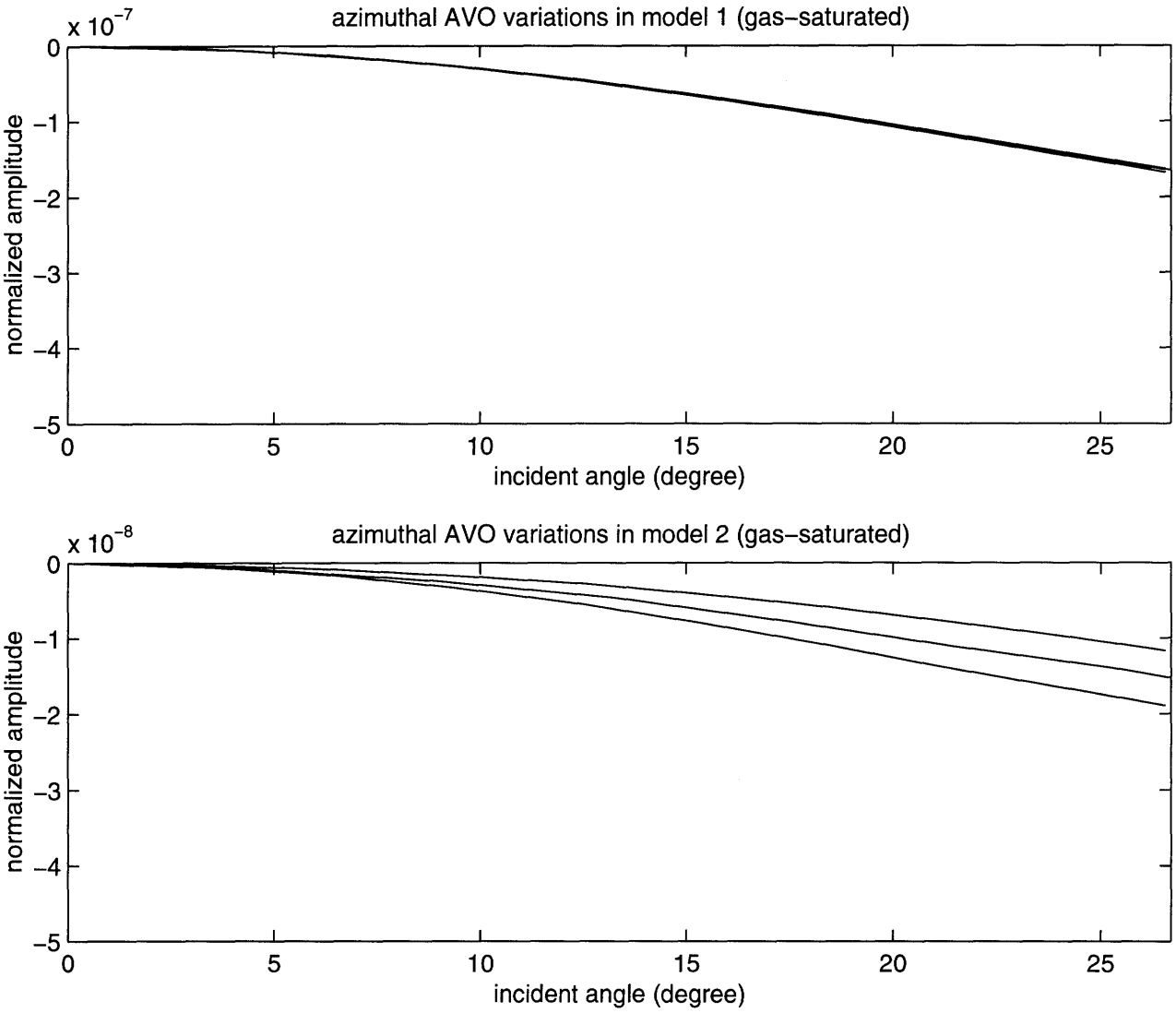

Figure 2-5 Azimuthal AVO response at the top of gas-saturated, fractured reservoirs. (a) azimuthal AVO response in model 1; (2) azimuthal AVO response in model 2. AVO response at azimuth 90^{o} (crack strike): top solid line; 45^{o}: middle solid line; 0^{o} (crack normal): bottom solid line.

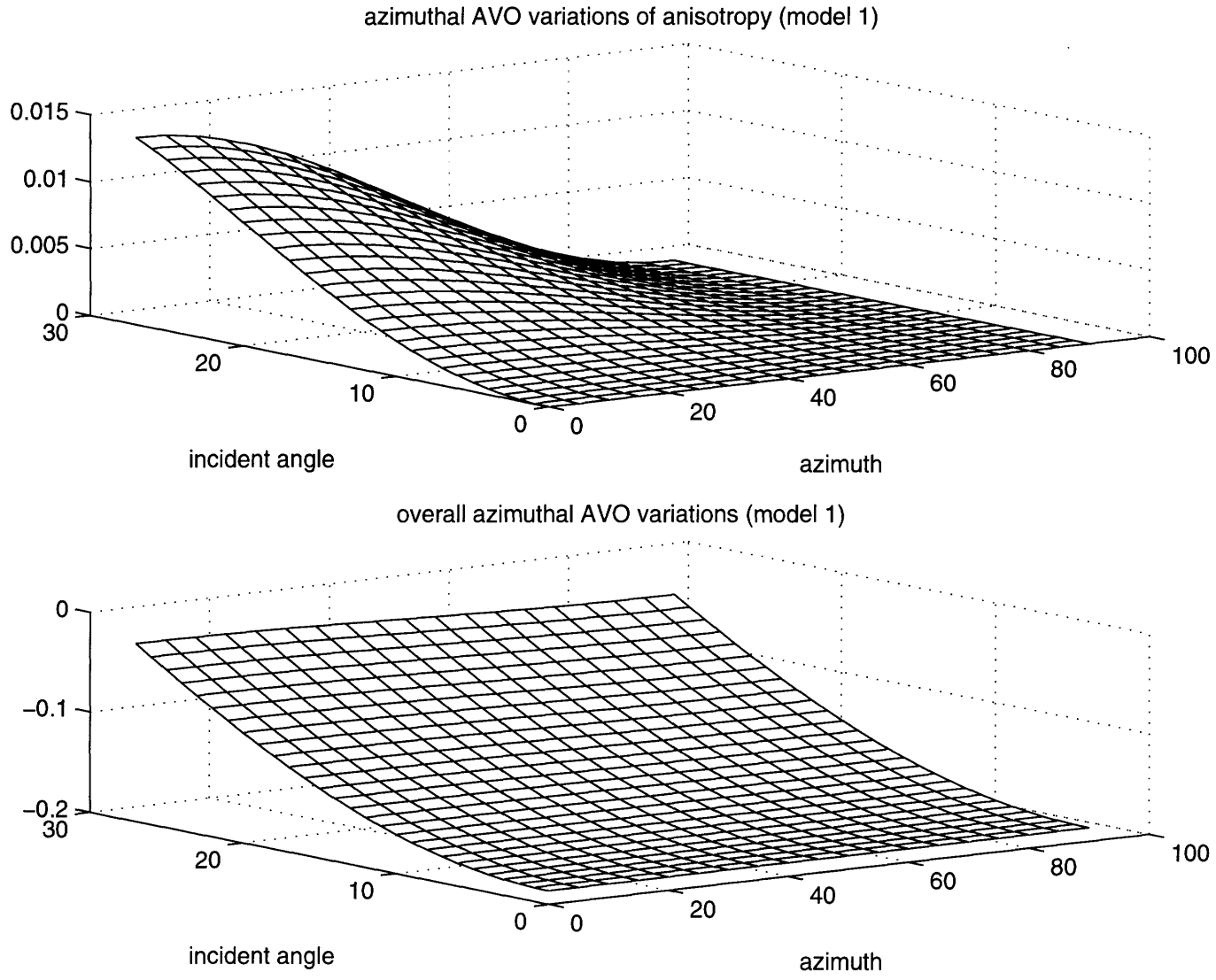

Figure 2-6 Reflection coefficient at the top of gas-saturated, fractured reservoir model 1. (a) fracture-induced azimuthal AVO response; (b) overall azimuthal AVO response.

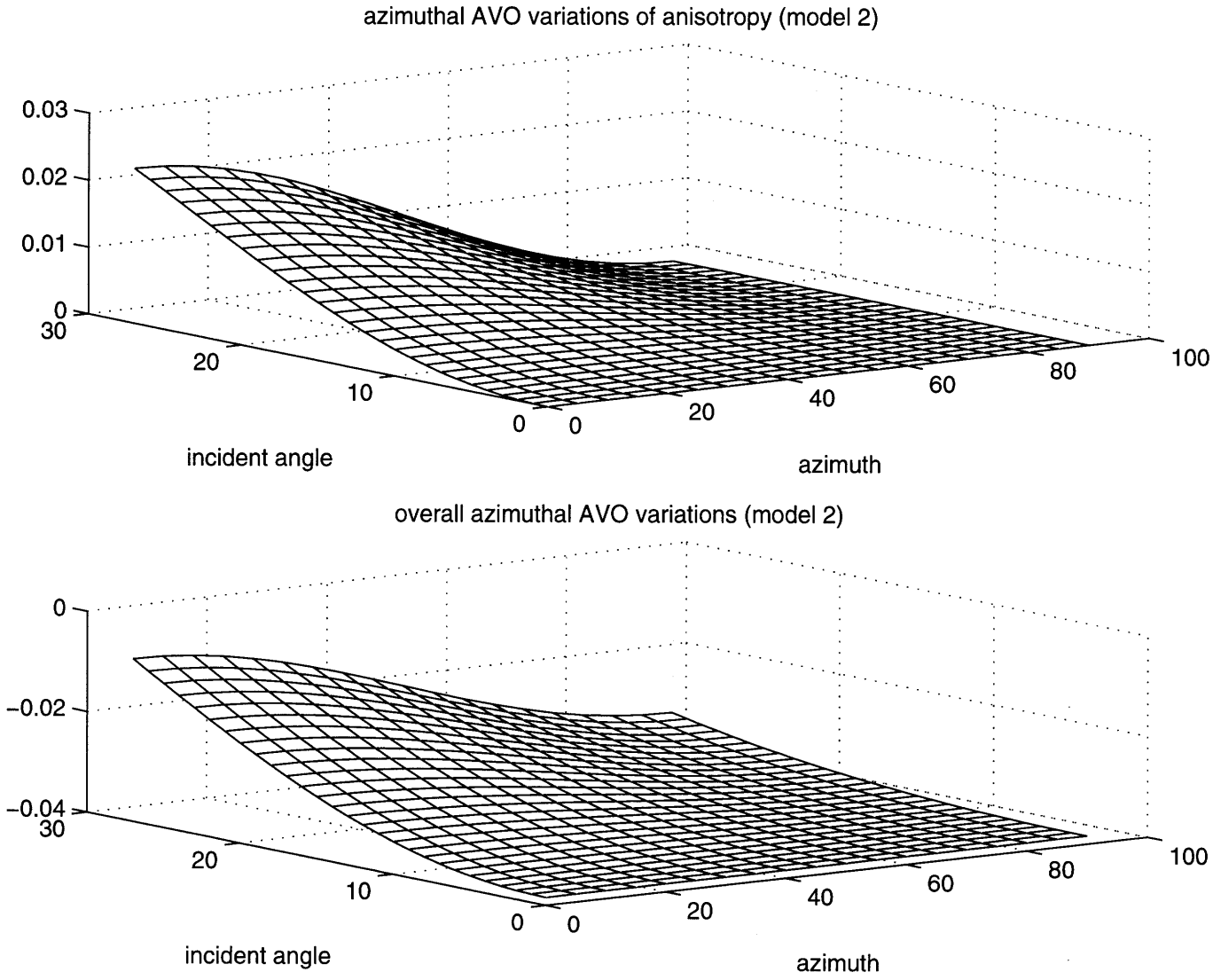

Figure 2-7 Reflection coefficient at the top of gas-saturated, fractured reservoir model 2. (a) fracture-induced azimuthal AVO response; (b) overall azimuthal AVO response.

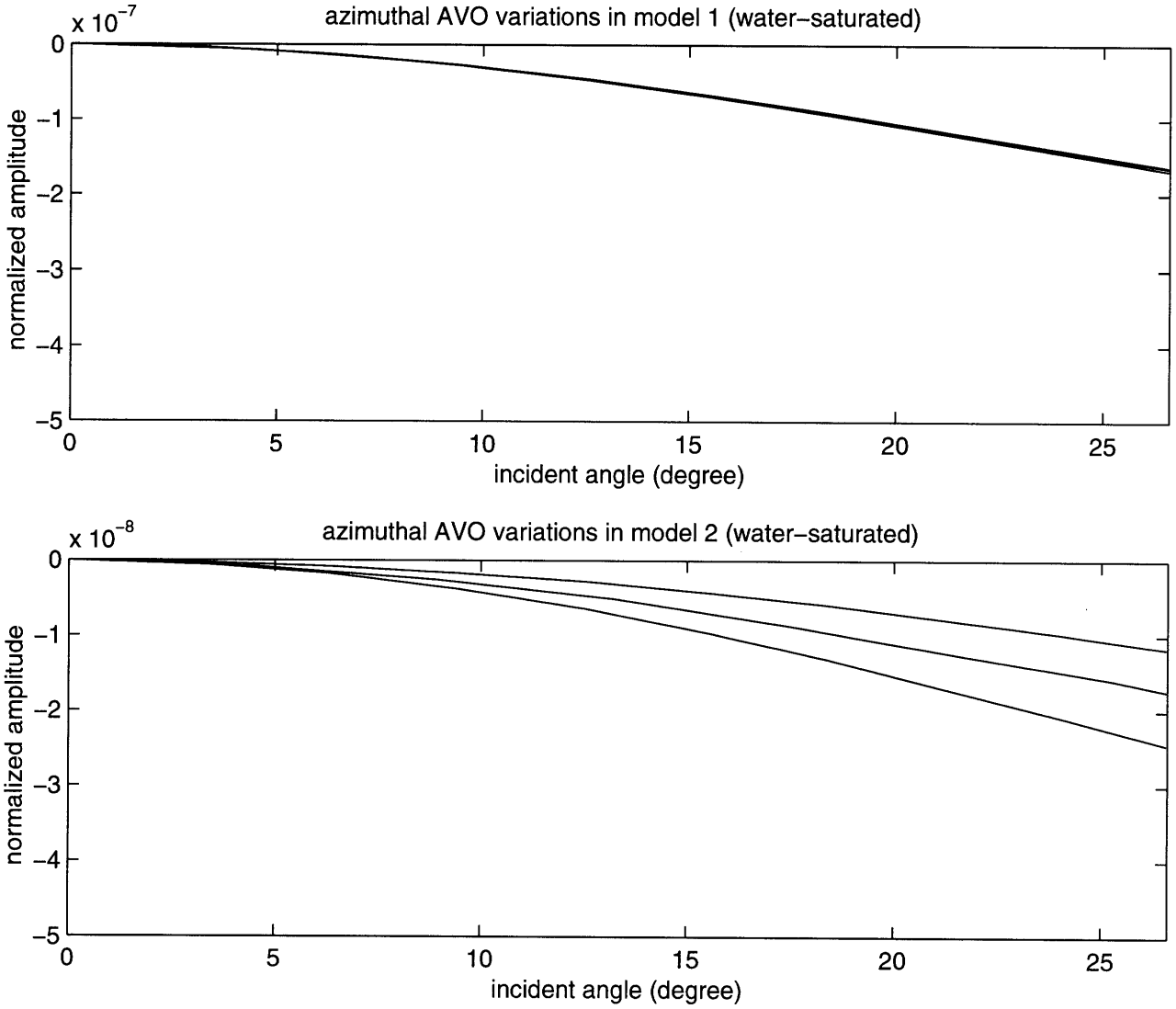

Figure 2-8 Azimuthal AVO response at the top of water-saturated, fractured reservoirs. (a) azimuthal AVO response in model 1; (2) azimuthal AVO response in model 2. AVO response at azimuth 90° (in crack strike): top solid line; 45°: middle solid line; 0° (crack normal): bottom solid line.

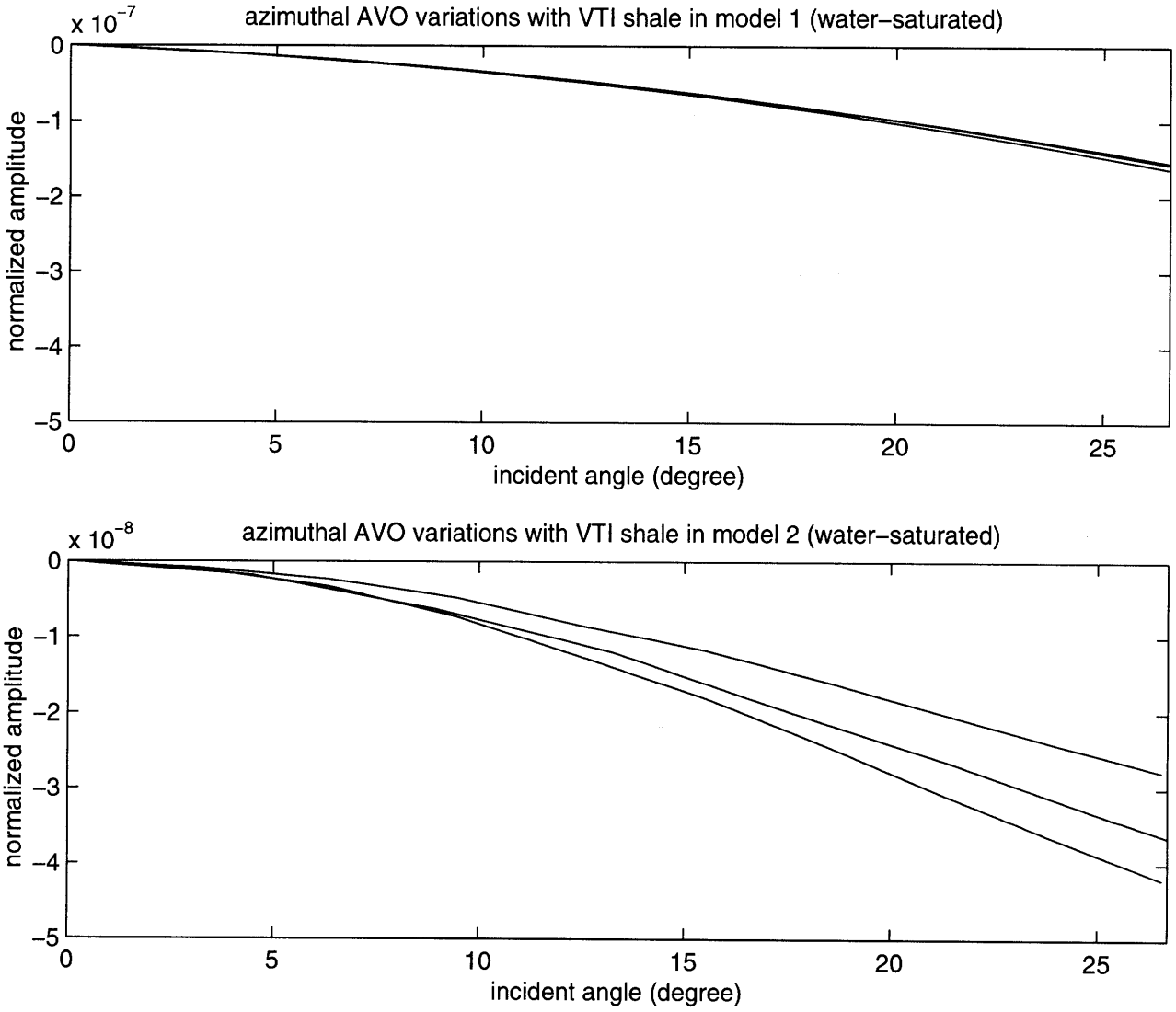

Figure 2-9 Azimuthal AVO response at the top of water-saturated, fractured reservoirs with overlying, transversely isotropic shale. (a) azimuthal AVO response in model 1; (2) azimuthal AVO response in model 2. AVO response at azimuth 90° (in crack strike): top solid line; 45°: middle solid line; 0° (crack normal): bottom solid line.

CHAPTER 3

Scattering Characteristics in Heterogeneous Fractured Reservoirs From Waveform Estimation

3.1 SUMMARY

Offset-dependent characteristics of seismic scattering are useful for interpreting fractured reservoirs. We use two models which have different background medium properties and different azimuthal AVO responses. Heterogeneous fracture density realizations are built through stochastic modeling. Synthetic seismograms generated by 3-D finite difference modeling are applied to studying elastic wave propagation and scattering in gas-saturated, heterogeneous fractured reservoirs. Waveforms in crack normal and strike directions are considered in this chapter. The multiple signal classification (MUSIC) frequency estimator is used in waveform estimation to provide frequency domain attributes related to seismic wave scattering by fractures. Our results indicate that the strength of the scattering field is a function of the background medium. The strength also increases with increasing fracture scatter density and with decreasing correlation length of spatial variations of fracture density. The scattering field is weak at the top of a fractured reservoir. The first order results are dominated by velocity anisotropy of a mean crack density field. However, the base of the fractured reservoir corresponds to a strong scattering field on which fracture heterogeneity has a larger effect.

Key words: heterogeneous fractured reservoirs, 3-D finite difference modeling, waveform estimation, offset, scattering characteristics

3.2 INTRODUCTION

Research in vertically aligned fractured media shows that the effect of fractures is a function of both incident angle and azimuth. Using a physical model, Chang and Gardner (1993) find that the magnitude of the reflection amplitude decreases with increasing offset and the rate of decrease is greatest for acquisition perpendicular to the features. Theoreti-

cal studies by Sayers and Rickett (1997) show that for gas-filled, open fractures in sandstone, the effect of fractures only becomes noticeable as the critical angle for the unfractured sandstone is approached. However, for reflections from the base of the fracture unit, the azimuthal AVO response is stronger and more visible at the conventional offset. Additionally, azimuthal AVO response in homogeneous fractured media is realized and applied to fracture detection in seismic data sets. Lynn et al (1995) and Perez and Gibson (1996) relate azimuth-dependent P-wave AVO response to open fracture orientation. As pointed out by Sayers and Rickett (1997), an azimuthal variation in AVO due to fractures in the overburden may be misinterpreted as due to the presence of aligned fractures in the reservoir. Therefore, other attributes correlated to fracture effects are helpful in constraining our interpretation and characterization of fractured reservoirs.

Seismic studies of fractured reservoirs indicate that fracture density variations can be present in these reservoirs. By studying P-S converted waves, Ata and Michelena (1995) generate anisotropy maps (fracture orientation and density) of the reservoirs and correlate their results with available well data. Based on a 3-D AVO technique, Ramos and Davis (1997) also show spatial variations of crack density in coal bed methane reservoirs. With any seismic data analysis and interpretation, however, we must consider the fundamental question of how much detail can be interpreted reliably from the data. This issue is particularly pertinent to fractured reservoirs, where geological control and other source information are scarce.

Previous studies show that effects of heterogeneity on scattering in isotropic media lead to the creation of coda waves (incoherent energy), damping of transmitted waves, and variation in coherent waveforms (Aki, 1969; Richards and Menke, 1983; Toksoz and Charette, 1990, Wu and Aki, 1990). However, as far as we know, effects of heterogeneity and associated characteristics on wave scattering in heterogeneous anisotropic (fractured) media remains, for the most part, unstudied. In heterogeneous fractured reservoirs with fracture density varying spatially, it is expected that fractures have different effects on wave scattering at the top and the base of reservoirs due to different wave propagation paths and transmission processing. Groenenboom and Snieder (1995) have characterized parameters of heterogeneities by determining the effects of heterogeneity on the phases and amplitudes of coherent waves. In this study, we also use coherent waveforms

(reflected waves) to quantify the effects of fracture heterogeneity. The scattering characteristics can be extracted from waveforms in the frequency domain. These characteristics help us understand the effects of the heterogeneous fracture density field on the seismic response and interpret fractured reservoir characteristics with estimated attributes.

Amplitudes can be directly estimated from seismic data or synthetic seismograms. However, higher resolution signal estimation techniques are needed both for investigating fracture effects on the frequency and energy of reflected waves and for understanding scattering characteristics in fractured reservoirs in more detail. We apply a technique--the multiple signal classification method (MUSIC)--to extract offset-dependent parameters from seismic waveforms in the frequency domain. The term multiple signal classification describes experimental and theoretical techniques involved in determining the parameters of multiple wavefronts arriving at an antenna array. These parameters are based on measurements of signals received at the array elements. The introduction of the MUSIC algorithm (Schmidt, 1979; Bienvenu and Kopp, 1980), which requires a one-dimensional search, was an attempt to more fully exploit the underlying data model. This method improves the resolution of bearing in passive sonar arrays, multiple emitter location and signal parameter estimation, and sensor array processing (Schmidt, 1979, 1986; Johnson and DeGraaf, 1982; Viberg and Ottersten, 1991). This technique has better resolution and better frequency estimation characteristics than spectral techniques such as autoregressive or Prony. MUSIC has received much attention and can provide asymptotically unbiased estimations of signals. The asymptotic properties of MUSIC are well documented in the literature (e.g., Jeffries and Farrier, 1985; Porat and Friedlander, 1988; Clergeot *et al.*, 1989).

In this chapter, we introduce the eigenvector based estimation technique, MUSIC, to the waveform estimation of synthetic seismograms, which are generated by 3-D finite difference modeling and reflected from the top and the base of fractured reservoirs in a frequency-offset domain. Frequency dependent signal signatures estimated by the frequency estimator are used to study properties of wave propagation through three-dimensional, gas-saturated, heterogeneous fractured reservoirs. By investigating the effects of fracture heterogeneity on reflected P-waves, we seek to explain and understand characteristics of seismic scattering by fractures. The objective of this chapter is to make clear which char-

acteristics related to scattering by fractures can be extracted from reflected waves and thus can be used in fracture interpretation.

3.3 SIGNAL PARAMETER ESTIMATION FUNCTION

This method is based on an eigenanalysis of an autocorrelation matrix. It separates information in the autocorrelation matrix into two vector subspaces, one a signal space and the other a noise space. Functions of the vector in either the signal or noise space can be used to create frequency estimators. The estimated number of spectral peaks by the frequency estimator represents the number of signals. The signal locations in the frequency range indicate the signal frequencies. A detailed discussion about the frequency estimator is in the appendix.

The frequency estimator function can be written as

$$F(f) = \frac{1}{\sum_{k=M+1}^{P+1} \alpha_k \left| e^H(f) v_k \right|^2} \qquad (1)$$

where α is the weighting function, M is the number of signals, v is a eigenvector and e is a complex sinusoid vector. The estimation causes the function *F(f)* to have very sharp peaks at the signal frequencies. Note that the frequency estimator is a pseudo spectrum estimator because the autocorrelation sequence cannot be recovered by Fourier transforming the frequency estimator. Setting $\alpha_k = 1$ for all k leads to the multiple signal classification algorithm (Schmidt, 1986)

$$F(f) = \frac{1}{e^H(f)\left(\sum_{k=M+1}^{P+1} V_k V_k^H \right) e^H(f)} \quad . \qquad (2)$$

Setting $\alpha_k = 1/\lambda_k$ for all k yields the eigenvector algorithm frequency estimator (Johnson and Degraaf, 1982)

$$F(f) = \frac{1}{e^H(f)\left(\sum_{k=M+1}^{P+1} \frac{1}{\lambda_k} V_k V_k^H \right) e^H(f)} \quad . \qquad (3)$$

3.4 SCATTERING CHARACTERISTICS IN TWO FRACTURED RESERVOIR MODELS

The background medium has a large effect on azimuthal AVO response in fractured reservoirs. Therefore, it is expected that the background medium is also an important parameter in affecting the strength of the scattering field. Based on the different azimuthal AVO response, we consider two kinds of representative reservoir models to study seismic scattering by heterogeneous fractures. Model 1 has strong azimuthal AVO response from both the top and the base of the reservoir. Model 2 has observable azimuthal AVO response only at the base of the fractured reservoir. The AVO responses for model 1 and model 2 in gas-saturated homogeneous fractured reservoirs are shown in Figure 1. The AVO responses are generated by 3-D finite difference modeling with 10% crack density. Isotropic background parameters in Model 1 are taken from laboratory measurements (Teng and Mavko, 1996); model 2 parameters are taken from a class 1 gas sand example (Rutherford and Williams, 1989). Model 1 has smaller property contrasts in the background medium than model 2. The parameters of background rocks and fractures for both models are listed in Table 1.

In this section, frequency dependent signal signatures, estimated by the frequency estimator from 3-D synthetic waveforms in crack normal and strike directions, are used to quantify the scattering characteristics for model 1 and model 2. Time domain characteristics, such as peak-to-peak amplitudes and travel times, can be obtained directly from synthetic seismograms. Travel times are determined by finding the time of the P-wave amplitude's first peak on the synthetic seismograms. The travel times are measured to an accuracy of the time step in the finite difference simulations.

3.4.1 3-D finite difference applied to model 1 and model 2

Most theoretical studies of seismic scattering are based on the first Born approximation and generalized Born approximation, which states that only single scattering occurs and that scattering losses from the primary wave can be neglected (Chernov 1960; Charrette, 1991; Coates and Charrette, 1993). Although these theories (for example, signal scattering theories) can give explicit relationships between the model parameters and observed seismograms, their application in complicated physical models is limited. To obtain accurate seismic waveforms from heterogeneous fractured media, we use a 3-D

finite difference scheme. The finite difference method is applied to study seismic wave scattering in random media (Richards and Menke, 1983; Frankel and Clayton, 1984, 1986; Ikelle *et al.*, 1993). The advantage in using this method is that it produces synthetic seismograms for any point on the grid, it is accurate over a wide range of scattering regimes, and all wave types (direct wave, reflection wave, multiply scattered waves, converted waves, etc.) are included.

The 3-D time domain, staggered grid finite difference method is used to obtain accurate seismograms. This method has fourth-order accuracy in space and second-order accuracy in time (Cheng *et al.*, 1995). Intrinsic attenuation is not included in these simulations. Effective medium and Hudson's crack models (Hudson, 1981, Hudson *et al.*, 1996) have been used in elastic tensor inversion, which has been studied in detail (Shen *et al.*, 1997). For simplicity, the fractured reservoir is assumed to have the same shale both above and below it. Seismograms in crack normal and strike directions are considered. There are 41 traces in each direction and the minimum offset is 0 and the maximum offset is approximated to a 30 degree incident angle relative to the first reflected layer. An explosion source is used, and the dominant frequency of the source wavelet is 45Hz. The physical model and source receiver configurations are shown in Figure 2. All edges of the grid have absorbing boundary conditions to suppress artificial reflections.

For statistically homogeneous-aligned fractures, velocity anisotropy is spatially uniform. Heterogeneity due to spatial variations of fracture density could result in spatial variations of velocity anisotropy. Statistical representation is used to describe small-scale inhomogeneities in seismological studies. In this study, for stochastic modeling to be practical, the fracture density field is modeled as a spatially stationary Gaussian random field. The Von Karman correlation function is used to model heterogeneity in the fracture density, which is specified by the function describing its amplitude, orientation, characteristic wave numbers and its roughness number. The properties of the Von Karman correlation function have been described by Goff and Jordan (1988) in detail. For our simulation to be simple and practical, we assume that fracture density does not vary with depth. For each model, we construct three heterogeneous fracture density realizations, which have the same characteristic wave number value, 0.0032, in the y direction and different characteristic wave number values, 0.08, 0.032 and 0.0128, in the x direction. The roughness num-

ber is 0.8. Figure 3 shows three fracture density realizations. Finite difference simulations are used to generate synthetic seismograms in heterogeneous fractured reservoirs with different fracture density realizations. Figures 4a, 4b and 4c show an example of vertical component synthetic seismograms in model 2 in the crack normal direction. The source coordinate in the x-y plane locates at grid point (50,50). Waveforms within time windows are used in parameter estimations, which correspond to reflections from the top and the base of gas saturated fractured reservoirs.

3.4.2 Scattering characteristics in fractured reservoir model 1

Scattering at the top of the reservoir

In model 1, the azimuthal AVO response from the top of the fractured reservoir is larger than that at the reservoir base due to the difference in incident angles. The highest AVO gradient is in the crack normal direction. Figure 5 shows the power spectral image versus offset and frequency, estimated from seismograms at the top of the heterogeneous fractured reservoirs in the crack normal direction. Each reservoir has a mean of 5% and a 5% standard deviation in crack density, but each has a different fracture density realization. The spectral image obtained in the crack strike direction is shown in the same diagram for comparison. Some major features are worth noting. In both crack normal and strike directions, signals distribute mainly at the dominant source frequency. With the increase in offset, frequencies of power spectral peaks (signal frequencies) in the crack normal direction shift toward a lower frequency range than those in the crack strike direction. In addition to the signal frequency varying with offset, the estimated power spectra also show some offset-dependent characteristics. Estimated signal power spectra decrease with increase of offset. The energy decay rate in each heterogeneous fractured sandstone normal direction is larger than that in the crack strike direction. However, in the crack normal direction, the variations of the power spectral image with offset do not show visible differences in the three heterogeneous fractured reservoirs. Therefore, the presence of fractures tends to lower signal frequencies and enhances the signal power decay rate at the top of model 1's fractured reservoir.

It also is instructive to compare characteristics of power spectra obtained in the frequency domain with amplitudes obtained in the time domain. The spectral variations with

offset obtained in the frequency domain are comparable and consistent with amplitude variations in the time domain. The amplitude variation gradient obtained in the crack normal direction is larger than that in the crack strike direction (with 0 crack density) (Figure 6a). Normalized peak to peak amplitudes obtained in the crack normal direction from three heterogeneous fractured reservoirs do not show observable differences (Figure 6a). Note also that, to the first order approximation, amplitude variations with offset obtained from heterogeneous fracture reservoirs are the same as AVO responses from homogeneous fractured reservoirs with 5% crack density. Considering the first order effects of fracture heterogeneity, neither the estimated power spectra nor the amplitudes show the spatial fracture heterogeneity at the top of the fractured reservoirs. Also, signal power (amplitude) variations with offset are dominated by velocity anisotropy of the mean crack density field. Another attribute obtained only in the time domain is the travel time azimuthal variation (Figure 6b). There is no travel time azimuthal variation because the presence of fractures only changes the reflectivity at the top of fractured reservoirs and because there is no velocity variation in the wave propagation paths.

Scattering at the base of the reservoir

The scattering characteristics of reflected waves at the base of fractured reservoirs differ from those at the top of fractured reservoirs not only in the frequency domain but also in the time domain. Variations in incident angles and fracture density result in velocity fluctuations. In addition to the reflectivity variations due to fractures, the velocity variations also are imposed on transmission and reflection processes. Because oblique incident waves have been transmitted downward through the fractured medium to its base and then reflected and retransmitted back up, effects associated with scattering strongly influence the reflected waves.

The spectral image, estimated from seismograms reflected from the base of the fractured reservoir, is shown in Figure 7. In the crack strike direction, observable signals distribute around the dominant source frequency. In the crack normal direction, however, higher frequency signals are visible and major signals distribute at the dominant source frequency. The secondary signal modes are most noticeable in the reservoir with the shortest correlation length of the fracture density realization. We infer from our results that the presence of secondary signal modes in the higher frequency range can be attributed to

wave scattering by fracture heterogeneity. Larger fracture density variations give rise to larger velocity variations. Therefore, the shortest correlation length of the spatial variations of fracture density tends to enhance the strength of the scattering field at the base of fractured reservoirs. The calculated normalized power spectra at the source frequency in the crack normal direction show a larger fluctuation along the offset than those in the crack strike direction. In addition, multiple waves exist in the propagation processes and thus would interfere with the fracture scattering field. Determining exactly how multiple scattering interferes with scattering of the fracture field is beyond the scope of this chapter.

Peak-to-peak amplitudes from the seismograms show that the effects of fracture heterogeneity are more observable at the base of the fractured reservoir than at the reservoir top (Figure 8a) and that the shorter the correlation length in fracture heterogeneity, the larger the amplitude oscillation. This amplitude variation is consistent with those of spectra estimated in the frequency domain. Additionally, it is expected that travel time fluctuations would occur at the reservoir base. Figure 8b shows that the travel time difference is observed at the far offset.

Effects from scatter density on scattering characteristics

We increase the scatter density by changing the mean of crack density from 5% to 10% and the standard deviation from 5% to 10%. The estimated power spectra from the reservoir top are shown in Figure 9. Compared with the results in Figure 5, the signal energy decay with offset becomes increasingly rapid from the middle to the far offset. The decrease of signal frequencies with offset is more observable in the far offset where the fracture effect becomes greatest. To illustrate these variations clearly, the signal frequencies and normalized spectral peaks, varying with offset, are calculated. Results indicate that, from the middle to the far offset, the frequency decay along the offset in each crack normal direction has a higher gradient than that in the crack strike direction. Results also indicate that the normalized spectral peaks decrease to 40% in the crack normal direction and 60% in the crack strike direction. These results are comparable with the normalized peak-to-peak amplitudes obtained in a homogeneous fractured model with 10% crack density (Figure 1). It can be found that, with the increase of scatter density, scattering characteristics become more and more observable.

The power spectrum image from the reservoir base also shows some differences (Fig-

ure 10). More and more secondary modes of higher frequency signals are generated in the fractured reservoir normal direction. The energy of these secondary modes still is strongest in the heterogeneous fracture reservoir with shortest correlation length in the fracture density field. Power spectra at the source frequency, in the crack normal direction, decrease with offset more quickly than those in crack strike direction.

Normalized amplitudes in the time domain still show similar oscillation patterns to those shown in Figure 6, but with larger amplitude decay rates. This similarity is expected because the realizations of the fracture heterogeneity are kept the same. Travel time shows larger azimuthal variation due to the increase of fracture density. It is shown, by comparison, that scattering characteristics by fractures become more obvious with increasing scatter density.

The scattering characteristics in model 1 show that: 1) at the top of the fractured reservoir reflected waves are characterized by lower frequency signal power, and 2) reflected waves at the base of the fractured reservoirs are characterized by the presence of secondary modes of high frequency signals.

3.4.3 Scattering characteristics in fractured reservoir model 2

Model 2 has different azimuthal AVO variations from model 1. Its Azimuthal AVO variations are only observable at the base of the reservoir. Normalized AVO has the highest decay rate in the crack strike direction.

Figure 11 shows the estimated power spectral image versus offset and frequency at the top of the fractured reservoir in the crack normal and strike directions. Signals distribute mainly at the source frequency in both directions. Signal frequency variations with offset do not show a detectable difference in the two directions. Normalized power spectra show almost identical azimuthal variations with offset. The decay rates of normalized amplitudes obtained in the time domain are consistent with those of spectral peaks estimated in the frequency domain. Neither signal power (amplitude) nor frequency show observable wave scattering characteristics by fractures at the top of the reservoirs in model 2.

At the base of the fractured reservoirs, signals distribute mainly around the source frequency (Figure 12). Azimuthal spectral variations can be observed at the base of the reservoir. The rate of decrease of spectral peaks with offset is greatest in the crack strike

direction. The variation gradients of normalized power spectra and peak-to-peak amplitudes along the offset are comparable to each other. The heterogeneity of the fracture density field is barely detectable either from the spectra estimated in the frequency domain or from peak-to-peak amplitudes in the time domain.

Again, we increase the mean crack density to 10% with a 10% standard deviation. As in the case with 5% mean crack density, there is no azimuthal difference at the top of the heterogeneous fractured reservoirs either in the signal frequency or in the normalized power spectrum. The power spectrum image at the base of the reservoir is shown in Figure 13. Signals at far offset are more centered around the source frequency. The energy decay rate in the crack normal direction becomes gentler than that in the case of 5% mean crack density. Note that in this model there are no secondary signal modes in the spectral image with the increase of scatter density. Normalized amplitudes in the time domain do not show noticeable differences at the base of the three heterogeneous fractured reservoirs. The travel time for 10% crack density has larger azimuthal variations than that of 5%.

Results from model 2 show that, at the top of fractured reservoirs, the effect of fractures is undetectable either in the time domain or in the frequency domain. At the base of fractured reservoirs, the strength of the scattering field becomes stronger, but only the azimuthal power spectrum, amplitude variations and azimuthal travel time show the effect of fractures. The heterogeneity of the fracture density field is not revealed by scattering characteristics.

The different scattering characteristics between model 1 and model 2 can be attributed to the properties of the background media. Owing to the smaller property contrasts in the background medium, the wave scattering by fractures are more noticeable in model 1 than in model 2. In model 1, both the signal energy and signal frequency indicate the different scattering characteristics by fractures at the top and the base of reservoirs. However, only the signal energy is effected by fractures in model 2. The effect of background medium is comparable with previous studies (Shen *et al.*, 1997).

3.5 DISCUSSION

Because most seismic data sets come from reflected P-waves, a detailed understanding of the effects of fracture density heterogeneity on P-wave seismic response is of primary

importance for fractured reservoir characterization. Although most studies of scattering by heterogeneity in isotropic media concentrate on transmitted waves, some studies use reflected P waves. Richards and Menke (1983) discuss reflected waves in randomly fluctuating models and indicate that a primary reflection can be understood to include all energy that has traveled in the leading pulse of a wave during transmission and has undergone one additional and identifiable reflection. It is difficult to quantify this idea rigorously, since the multiple scattering inherent in the transmission process interacts in too complex a way for a "reflection" to be singled out. Gibson and Levander (1988) use synthetic, 2-D reflected acoustic wave finite difference data sets to illustrate the effect of two mechanisms, irregular surface layer and deep zone of random velocity fluctuation, on seismic response in isotropic media. Levander *et al.* (1994) note that short-offset shot records demonstrate that the upper crust produces scattered waves which significantly disrupt signals reflected from deeper levels. Therefore, the damping of reflected waves, like damping of transmitted waves, can indicate heterogeneity.

Waveform variation, an important parameter in seismic scattering studies, has been noted by several authors. Richards and Menke (1983) observe similar numerical results from two different types of velocity fluctuations. The resulting pulse can be seen losing amplitude and broadening as transmitted waves propagate; this feature increases with the propagation path length. Frankel and Clayton (1986) quantify waveform variation by determining the cross correlation functions from finite difference synthetic seismograms. Thus, as a wave passes through a heterogeneous medium, its frequency and amplitude are affected by the inhomogeneities. These studies show that the variation of waveforms across seismic arrays is a useful observation that provides constraints on the heterogeneity. The high resolution estimation method is needed to extract robust attributes. The multiple signal classification method known as the frequency estimator can be applied to field seismic data analyses to estimate the number of signals, the frequency location of signals and the relative strength of signals.

Frequency domain attributes estimated from waveforms indicate that the scattering characteristics in fractured reservoirs vary in different background media. This is consistent with studies of AVO in transversely isotropic media by Blangy (1994). Blangy shows that anisotropic effects are more noticeable with small-contrasts in density when P- and S-

wave velocities exist and for a large incident angle. Our 3-D modeling studies also show that the smaller the background medium contrasts, the more observable azimuthal AVO responses appear in fractured reservoirs. In the examples presented above, scattering characteristics (spectrum and frequency vs. offset) can be detected easily from model 1. For instance, these characteristics can been found by comparing results of Figure 5 and Figure 11. An important implication for an interpreter is how the detectability of fractures depends on the geological setting of field-recorded data.

If the scattering indeed is caused by heterogeneity of the fracture density field, the characterization of the signal frequency variations with offset would discriminate the seismic response at the top and the base of fractured reservoirs. The presence of fractures tends to decrease the frequency of reflected waves from the top of fractured reservoirs. Also, the frequency decay with offset is smooth, which leads to a tendency for the coherent wave (reflected wave) field to become insensitive to the specific fracture distribution or the fracture heterogeneity. The first order effect on the offset-dependent frequency decay is the mean of fracture density. Contrary to the seismic response at the top of heterogeneous fractured reservoirs, high frequency secondary signal modes generated at the base of fractured reservoirs can be used to indicate scattering by heterogeneous fractures.

In the studies of wave scattering by heterogeneities in isotropic media, authors have noted that coda waves can be created in a number of different ways and with different frequencies. The characteristics of resulting frequencies of coda waves have been investigated carefully. Aki and Chouet (1975) indicate that while low frequency coda waves are dominated by surface waves, higher frequency coda waves are composed primarily of body waves that have been scattered at some depth. Coates and Charrette (1993) show that coda waves in impedance models have a lower frequency range and coda waves in velocity models have a higher and wider frequency range. The numerical results of Richards and Menke (1983) indicate that when scattering dominates over intrinsic friction, the coda of a transmitted wave contains higher frequencies than the initial pulse. Frankel and Clayton (1986) show that the presence of higher frequency seismic coda is a major constraint on the heterogeneity spectrum of the crust. All of these authors conclude that coda waves with high frequency result from strong scattering by inhomogeneities.

The spatial variations of heterogeneity is another factor affecting scattering character-

istics. Frankel and Clayton (1986) show that the coda amplitude decreases strongly for the exponential medium (equivalent to Von Karman function with roughness parameter 0.5) as the correlating distance increases. Our results show that the strongest scattering characteristics can be observed in model 1 with shortest correlation length in the fracture density realization.

While this chapter attempts to quantify the scattering characteristics in gas-saturated, heterogeneous fractured reservoirs, field reservoirs are, undoubtedly, even more complex. First, the background medium could be vertically and/or laterally heterogeneous. Second, anelastic attenuation is important in determining the strength of the scattered events in the field data. The relative roles of apparent and instrinsic attenuation, however are not well understood. Third, we must consider that some noise events may be caused by conversions between P-waves and S-waves. Relatively simple models, however, provide insights into the nature of scattering characteristics and effects of the fracture density heterogeneity on seismic responses.

3.6 CONCLUSIONS

The purpose of this chapter is to study the scattering characteristics of seismic waves reflected at the top and the base of fractured reservoirs and to extract useful attributes related to fracture properties.

We may draw four conclusions from the set of examples presented above. The first conclusion is that seismic wave scattering characteristics in heterogeneous fractured reservoirs can be studied with the coherent part of the seismic reflected waves, and these characteristics are offset dependent.

The second of these conclusions is that properties of the background medium dominate the scattering characteristics in heterogeneous fractured reservoirs. Owing to smaller contrasts of background properties, model 1 has a stronger scattering field. Signal frequency and power at the top and base of fractured reservoirs show specific scattering characteristics. However, model 2 has a weak scattering field, and only the signal power at the base of the reservoirs shows the effect of fractures on wave scattering.

The third conclusion is that wave scattering at the top of fractured reservoirs is insensitive to fracture heterogeneity. The scattering characteristics are comparable with proper-

ties of homogeneously fractured reservoirs with the same mean crack density. Fracture heterogeneity has a larger effect on the scattering field at the base of fractured reservoirs. The strength of the scattering field at the base of a fractured reservoir is inversely proportional to the correlation length of the fracture density field and proportional to the scatter (fracture) density.

The fourth conclusion is that scattering fields show different scattering characteristics at the top and the base of the fractured reservoirs. At the top of reservoirs, fractures only change the P-wave reflectivity, signals are characterized by low frequency and there are no visible azimuthal travel time variations. At the reservoir base, in addition to P-wave reflectivity variations, velocity fluctuations exist in the wave transmission and reflection processes. The presence of secondary, higher frequency signals is characteristic of a strong scattering field. Azimuthal travel time variations are observable at the base of fractured reservoirs. Both at the top and at the base of fractured reservoirs, the azimuthal power spectral variation is comparable with azimuthal amplitude response.

ACKNOWLEDGEMENTS

We appreciate Dan Burns at M.I.T. for his review this chapter and his helpful comments. We thank Jesus Sierra and Franklin Ruiz at M.I.T. for their helpful discussion. We specifically thank John Queen at Conoco Inc. for his enthusiastic encouragement and valuable comments. This research is supported by the Borehole Acoustics and Logging/Reservoir Delineation Consortium at M.I.T. and by Science Research Laboratory (Dept. of Energy Prime) grant # DE-82066-223II-1.

REFERENCES

Aki, K., 1969, Analysis of seismic coda of local earthquakes as scattered waves, J. Geophys. Res., 74, 615-631.

Aki, K., and Chouet, B., 1975, Origin of coda waves, source attenuation, and scattering effects: J. Geophys. Res., 80, 3322-3342.

Ata, E., and Michelena, R. J., 1995, Mapping distribution of fractures in a reservoir with P-S converted waves, The Leading Edge, 12, 664-676.

Bienvenu, G., and Kopp, L., 1980, Adaptivity to background noise spectral coherence for

high resolution passive methods, in Proc IEEE ICASSP (Denver, CO), 307-310.

Blangy, J. P., 1994, AVO in transversely isotropic media - An overview: Geophys., 59, 775-781.

Chang, C. H., and Gardner, G. H. F., 1993, Effects of vertically aligned fractures on reflection amplitudes: An Amplitudes-Versus-Offset study, 63rd SEG meeting (Washington D. C.), Expanded Abstracts, 769-771.

Charrete, E. E., 1991, Elastic wave scattering in random media, Ph.D. thesis, Massachusetts Institute of Technology, U. S. A.

Cheng, N., Cheng, C. H., and Toksoz, M. N., 1995, Borehole wave propagation in three-dimensions, J. Acoust. Soc. Am., 97, 3483-3493.

Chernov, L. A., 1960, Wave Propagation in a Random Medium, McGraw-Hill, New York.

Clergeot, H., Tressens, S., and Ouamri, A., 1989, Performance of high resolution frequencies estimation methods compared to the Cramer-Rao bounds, IEEE Transaction On Acoustics, Speech and Signal Processing, ASSP-37, 1703-1720.

Coates, R. T., and Charrette, E. E., 1993, A comparison of signal scattering and finite difference synthetic seismograms in realizations of 2-D elastic random media, Geophys. J. Int., 113, 463-482.

Frankel, A., and Clayton, R. W., 1986, Finite-difference simulations of seismic scattering: Implications for the propagation of short-period seismic waves in the crust and models of crustal heterogeneity, J. Geophys. Res., 91, 6465-6489.

Gibson, B. S., and Levander, A. R., 1988, Modeling and processing of scattered waves in seismic reflection surveys, Geophysics, 53, 466-478.

Goff, J. A., and Jordan,T. H., 1988, Stochastic modeling of seafloor-morphology: Inversion of sea beam data for second-order statistics, J. Geophys. Res., 93, 13589-13608.

Groenenboom, J., and Snieder, R., 1995, Attenuation, dispersion, and anisotropy by multiple scattering of transmitted waves through distributions of scatters, J. Acoust. Soc. Am., 98, 3482-3492.

Hudson, J. A., 1981, Wave speeds and attenuations of elastic waves in material containing cracks, Geophys. J. Roy. Astr. Soc., Soc., 64, 133-150.

Hudson, J. A., Liu, E. and Crampin, S., 1996, Transmission properties of a plan fault: Geophys. J. Int., 125, 559-566

Ikelle, L. T., Yung, S. K., and Daube, F., 1993, 2-D random media with ellipsoidal autocorrelation functions, Geophysics, 58, 1359-1372.

Jeffries, D. J., and Farrier, D. R., 1985, Asymptotic results for eigenvector methods, Proc. Inst. Elec. Eng., F, 132, 589-594.

Johnson, D. H., and DeGraaf, S. R., 1982, Improving the resolution of bearing in passive sonar arrays by eigenvalue analysis, IEEE Transaction On Acoustics, Speech and Signal Processing, ASSP-30, 638-647.

Levander, A., England, R. W., Smith, S. K., Hobbs, R. W., Goff, J. A., and Holliger, K., 1994, Stochastic characterization and seismic response of upper and middle crustal rocks based on the Lewisian gneiss complex, Scotland, Geophys. J. Int., 119, 243-259.

Lynn, H. B., Bates, C. R., Simon, K. M., and van Dok, R., 1995, The effects of azimuthal anisotropy in P-wave 3-D seismic, 65th Ann. Internat. Mtg., Soc. Expl. Geophys., Expanded Abstracts, 723-730.

Perez, M., and Gibson, R., 1996, Detection of fracture orientation using azimuthal variation of P-wave AVO responses: Barinas field (Venezuela), 66th Ann. Internat. Mtg., Soc. Expl. Geophys., Expanded Abstracts, 1353-1356.

Porat, B., and Friedlander, B., 1988, Analysis of the asymptotic relative efficiency of the MUSIC algorithms in resolving plabe waves in noise, IEEE Transaction On Acoustics, Speech and Signal Processing, ASSP-36, 532-544.

Ramos, A. C. B., and Davis, T. L., 1997, 3-D AVO analysis and modeling applied to fracture detection in coalbed methane reservoirs, Geophysics, 62, 1683-1695.

Richards, P. G., and Menke, W., 1983, The apparent attenuation of a scattering medium, Bull. Seismol. Soc. Am., 73, 1005-1022.

Rutherford, S. R., and Williams, M. W., 1989, Amplitude-Versus-Offset variations in gas sands, Geophysics, 54, 680-688.

Sayers, C. M., and Rickett, J., 1997, Azimuthal variation in AVO response for fractured gas sands, Geophysical Prospecting, 45, 165-182.

Schmidt, R., 1979, Multiple emitter location and signal parameter estimation, in Proc. RADC Spectral Estimation Workshop (Rome, NY), 243-258.

Schmidt, R., 1986, Multiple emitter location and signal parameter estimation, IEEE Transaction On Antennas and propagation, AP-34, 276-280.

Shen, F., Zhu, X., and Toksoz, M. N., 1997, Anisotropy of aligned fractures and P-wave azimuthal AVO response, 67th Ann. Internat. Mtg., Soc. Expl. Geophys., Expanded Abstracts, 2001-2004.

Teng, L., and Mavko, G., 1996, Fracture Signatures on P-wave AVOZ, 66th Ann. Internat. Mtg., Soc. Expl. Geophys., Expanded Abstracts, 1818-1821.

Toksoz, M. N., and Charette, E. E., 1990, Effects of random heterogeneities on seismic waves: Implications for determination of reservoir heterogeneities: Presented at Soc. Expl. Geophys. Japan Int. Conf. on Geotomography.

Viberg, M., and Ottersten, B., 1991, Sensor array processing based on subspace fitting, IEEE Transaction On Signal Processing, 39, 1110-1121.

Wax, M., and Kailath, T., 1985, Detection of signals by information theoretic criteria, IEEE Transaction On Acoustics, Speech and Signal Processing, ASSP-33, 378-392.

Wax, M., and Ziskind, I., 1989, On unique localization of multiple sources by passive sensor arrays, IEEE Transaction On Acoustics, Speech and Signal Processing, ASSP-37, 996-1000.

Wu, R. S., and Aki, K., eds., 1990, Scattering and Attenuation of Seismic Waves (Birkhauser, Basel), Vol 132.

APPENDIX 3-A: FREQUENCY ESTIMATORS

Seismic signals can be described as the convolution of the reflection sequence $\{a_i\}$ with the wavelet $W_i(t)$,

$$Y(t) = \sum_{i=0}^{P} a_i W_i(t-\tau_i) \quad . \tag{A1}$$

Because our interest is in the frequency domain, consider the Fourier transform of the seismic signals over time

$$Y(f) = \sum_{i=0}^{P} a_i \exp(-j2\pi f \tau_i) W_i(f) \quad . \tag{A2}$$

Assuming we have equally sampled data, the delays τ_i will be of the form iT, so $Y(f)$ becomes

$$Y(f,T) = \sum_{i=0}^{P} a_i \exp(-j2\pi f_i T) W_i(f) \quad . \tag{A3}$$

We assume that recorded seismic waveforms $X(f,T)$ consists of $Y(f,T)$ and complex valued noise N(f)

$$X(f,T) = Y(f,T) + N(f) \quad . \tag{A4}$$

The eigenvectors of the autocorrelation matrix R_p calculated from X are defined by the property

$$R_p V_i = \lambda_i V_i \tag{A5}$$

$$i=1, 2,..., p+1$$

where λ_i is the eigenvalue associated with the eigenvector V_i. Assume that the output contains the signal and noise which are uncorrelated to each other. Matrix R_p can be expressed as the sum of a signal autocorrelation matrix and a noise autocorrelation matrix. If M independent signals are in white noise, the correlation matrix can be written

$$R_p = \sum_{i=1}^{M} \rho_i s_i s_i^H + \sigma_w I \tag{A6}$$

in which ρ_i is the power of the ith signal and σ_w is the power of the noise. I is a $(p+1)$x$(p+1)$ identity matrix and s_i is a signal vector of dimensional $p+1$ with the frequency information

$$s_i = \begin{bmatrix} 1 \\ \exp(j2\pi fiT) \\ \cdots \\ \exp(j2\pi fiPT) \end{bmatrix} \quad . \tag{A7}$$

The signal matrix will have the eigendecomposition. It can be shown that a matrix of dimension $P+1$ with rank $M<P+1$ will have $P-M+1$ zero eigenvalues. The M largest eigenvectors correspond to the signal terms and $P+1-M$ smallest are orthogonal to all of the signal direction vectors. Thus the signal autocorrelation matrix can been written as

$$S_p = \sum_{i=1}^{M} p_i s_i s_i^H = \sum_{i=1}^{M} \lambda_i V_i V_i^H \quad . \tag{A8}$$

The alternative expression of the identity matrix in terms of orthorgonal eigenvectors is

$$I = \sum_{i=1}^{P+1} V_i V^H i \quad . \tag{A9}$$

R_p can be written in the form of

$$R_p = \sum_{i=1}^{M} \lambda_i V_i V_i^H + \sum_{i=1}^{P+1} \sigma_w V_i V_i^H \qquad \text{(A10)}$$

$$R_p = \sum_{i=1}^{M} (\lambda_i + \sigma_w) V_i V^H{}_i + \sum_{i=M+1}^{P+1} \sigma_w V_i V_i^H \quad . \qquad \text{(A11)}$$

The eigenvectors $V_{M+1},..., V_{P+1}$ span the noise subspace of Rp, all with identical eigenvalues, σ_w. The principal eigenvectors $V_1, V_2,..., V_M$ span the signal subspace of both R_p and S_P with eigenvalues $(\lambda_i+\sigma_w)$. Note that eigenvectors are orthogonal and that the principal eigenvectors span the same subspace of the signal vectors. The signal vectors are orthogonal to all the vectors in the noise subspace, i.e.,

$$s_i^H(f)\left(\sum_{k=M+1}^{P+1} \alpha_k V_k\right) = 0 \quad . \qquad \text{(A12)}$$
$$(1 \le i \le M)$$

This property forms the basis of the noise subspace frequency estimators.

APPENDIX 3-B: MODEL ORDER SELECTION

Because the best choice for the number of signals is not generally known *a priori*, in practice it is usually necessary to estimate the model order M based on some theoretical criteria to make the M close to the actual value. Minimum description length (MDL) order selection criteria, expanded by Wax and Kailath (1985) and by Wax and Ziskind (1989), are used to handle the subspace separation problem. Assuming $\lambda_0>\lambda_1>,..., \lambda_P$ are eigenvalues of the autocorrelation matrix R and $M<P$, where M is the number of signals (model order), and N is the number of data samples,

$$MDL(M) = -Ln\left(\frac{\prod_{i=M+1}^{P} \lambda_i^{\frac{1}{(P-M)}}}{\frac{1}{P-M}\sum_{i=M+1}^{P} \lambda_i}\right)^{(P-M)N} + \frac{1}{2}M(2P-M)Ln(N). \qquad \text{(A13)}$$

The number of signals is determined as the value of M {0,1,2,..., P} for which MDL is minimized. Johnson and DeGraaf (1982) study the sensitivity of multiple signal classification and the eigenvector algorithm through simulations. Their results indicate that the

eigenvector algorithm estimator is less sensitive to the choice of M and produces fewer spurious peaks than multiple signal classification estimators for a given choice of order P. This low sensitivity is due to the use of inverse eigenvalues weighting. This estimator also tends to shape the noise spectrum better than multiple signal classification.

Table 4: Elastic Parameters And Fracture parameters of Model 1 and Model 2

Model	Vp (m/s)	Vs (m/s)	ρ (g/cm^3)	Fracture density (%)	Fracture aspect ratio	Vs/Vp
Model 1 shale	4561	2988	2.67			0.655
Model 1 sand	4860	3210	2.32	10	0.01	0.660
Model 2 shale	3300	1700	2.35			0.515
Model 2 sand	4200	2700	2.49	10	0.01	0.643

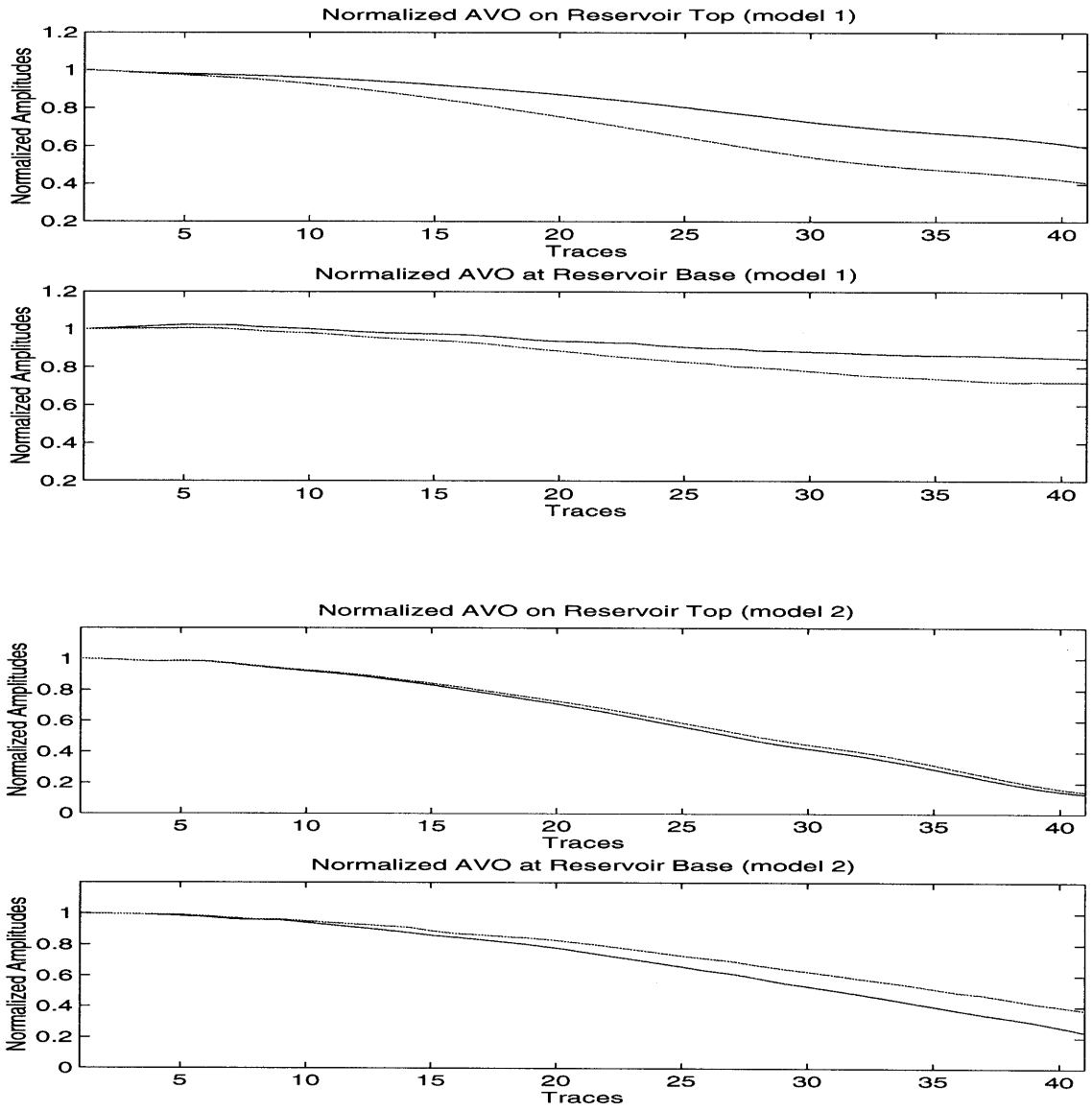

Figure 3-1 Normalized AVO response at the top and base of the fractured reservoir with 10% crack density in model 1 (upper plot) and model 2 (lower plot).

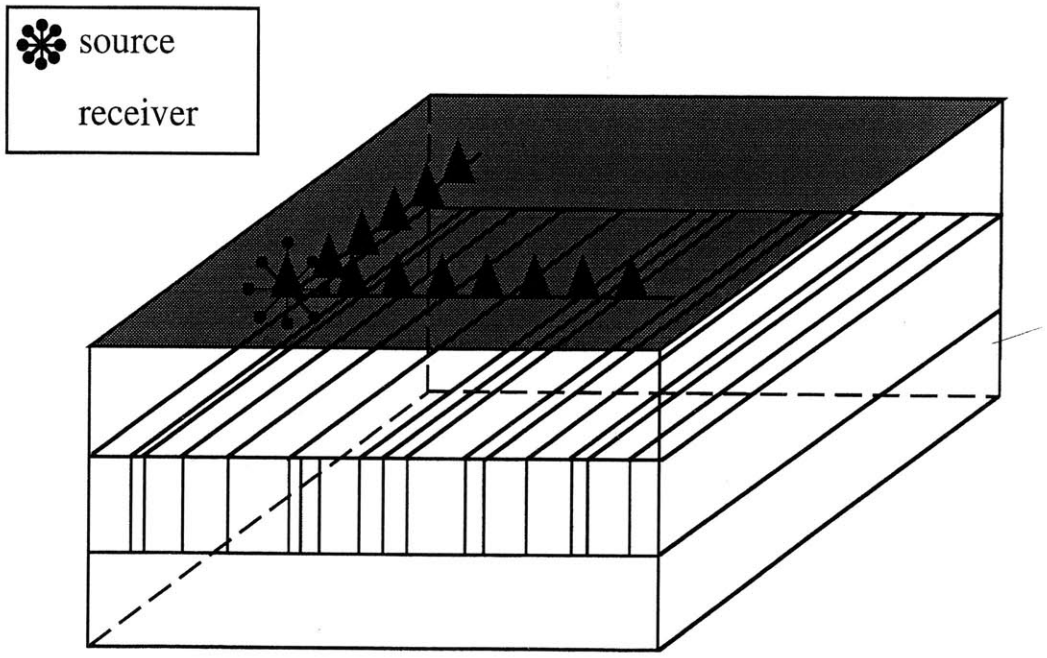

Figure 3-2 Source -receiver geometry and reservoir model used in numerical simulation.

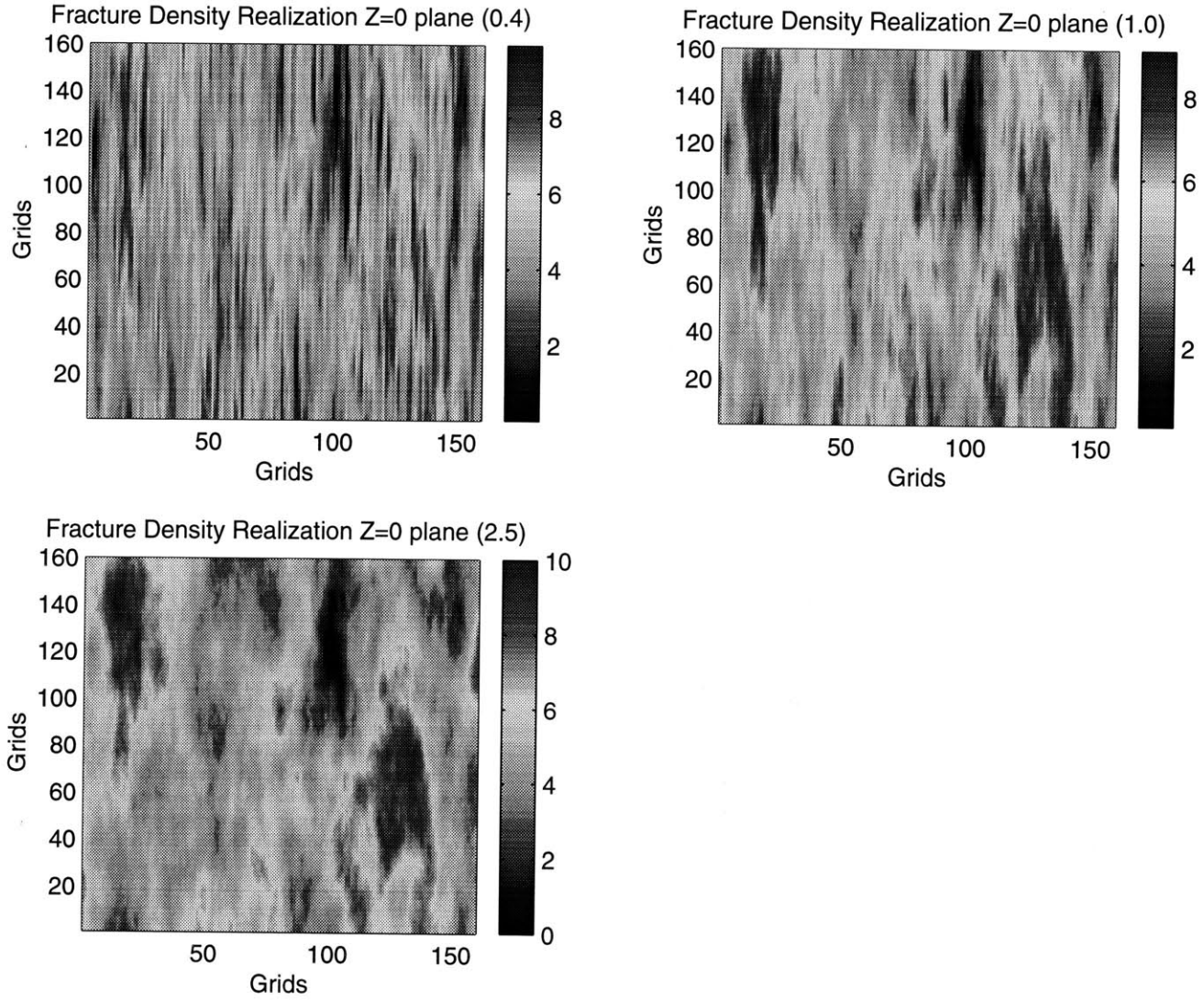

Figure 3-3 Fracture density realization with characteristic wave number values in x direction 0.08, 0.32 and 0.128, which are equivalent to correlation length 0.4, 1.0 and 2.5 wavelength.

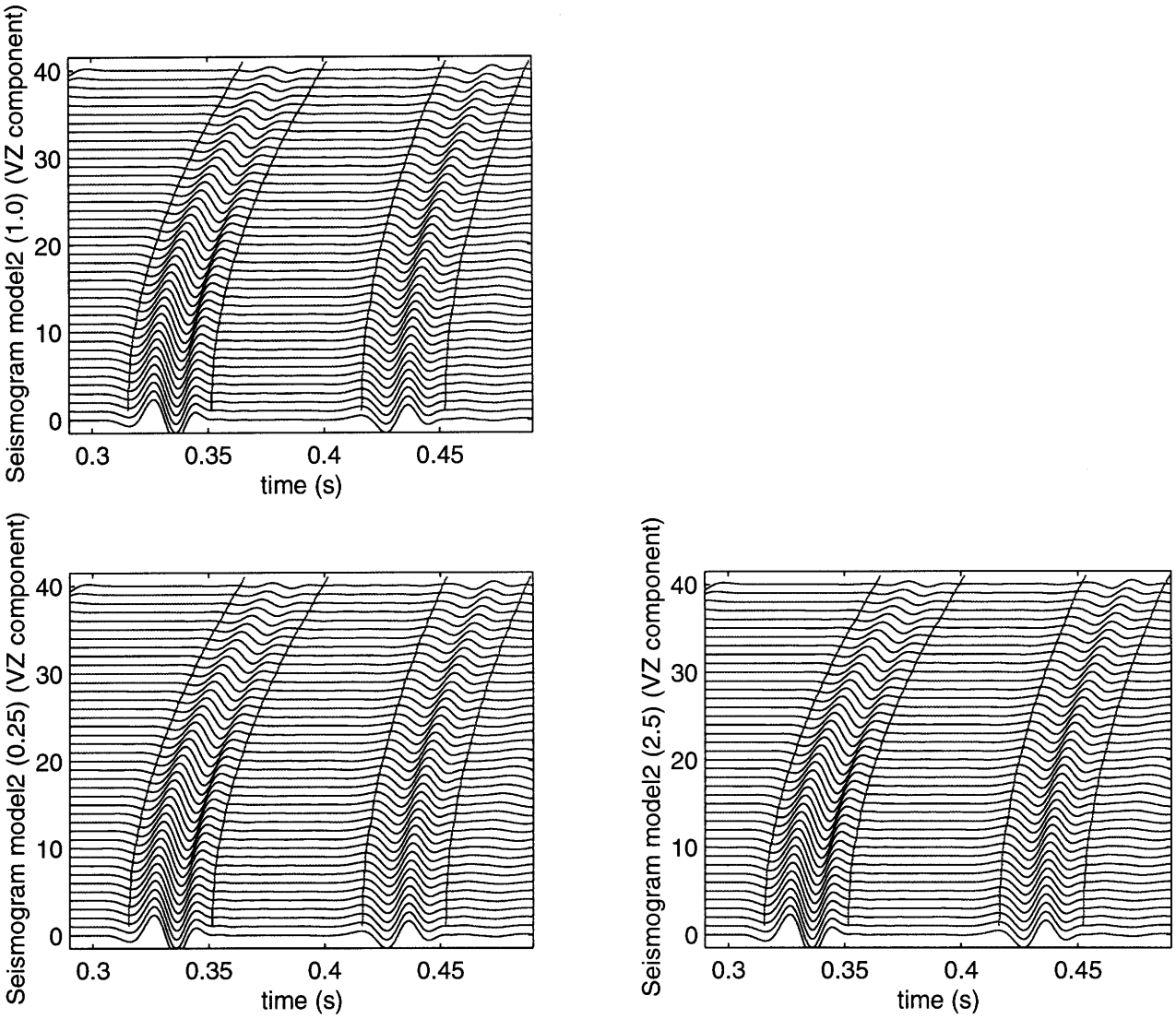

Figure 3-4 Vertical component seismograms generated from model 2 with the fracture density realization shown in figure 3.

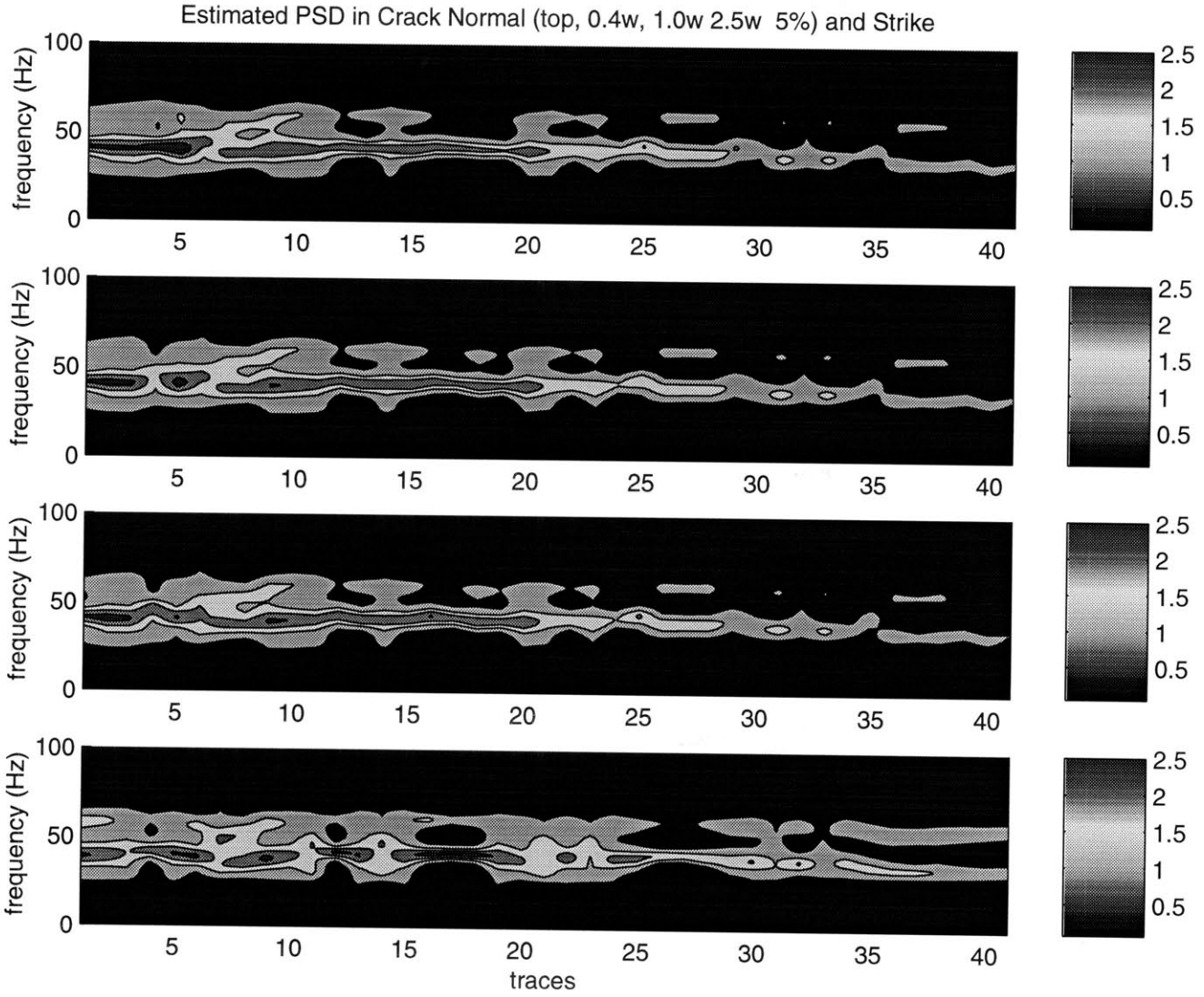

Figure 3-5 Power spectral image varies with frequency and offset (trace) at the top of the fractured reservoirs in model 1. From the top to the bottom, results are estimated from fracture realization models with correlation length 0.4, 1.0 and 2.5 wavelength and fracture strike direction.

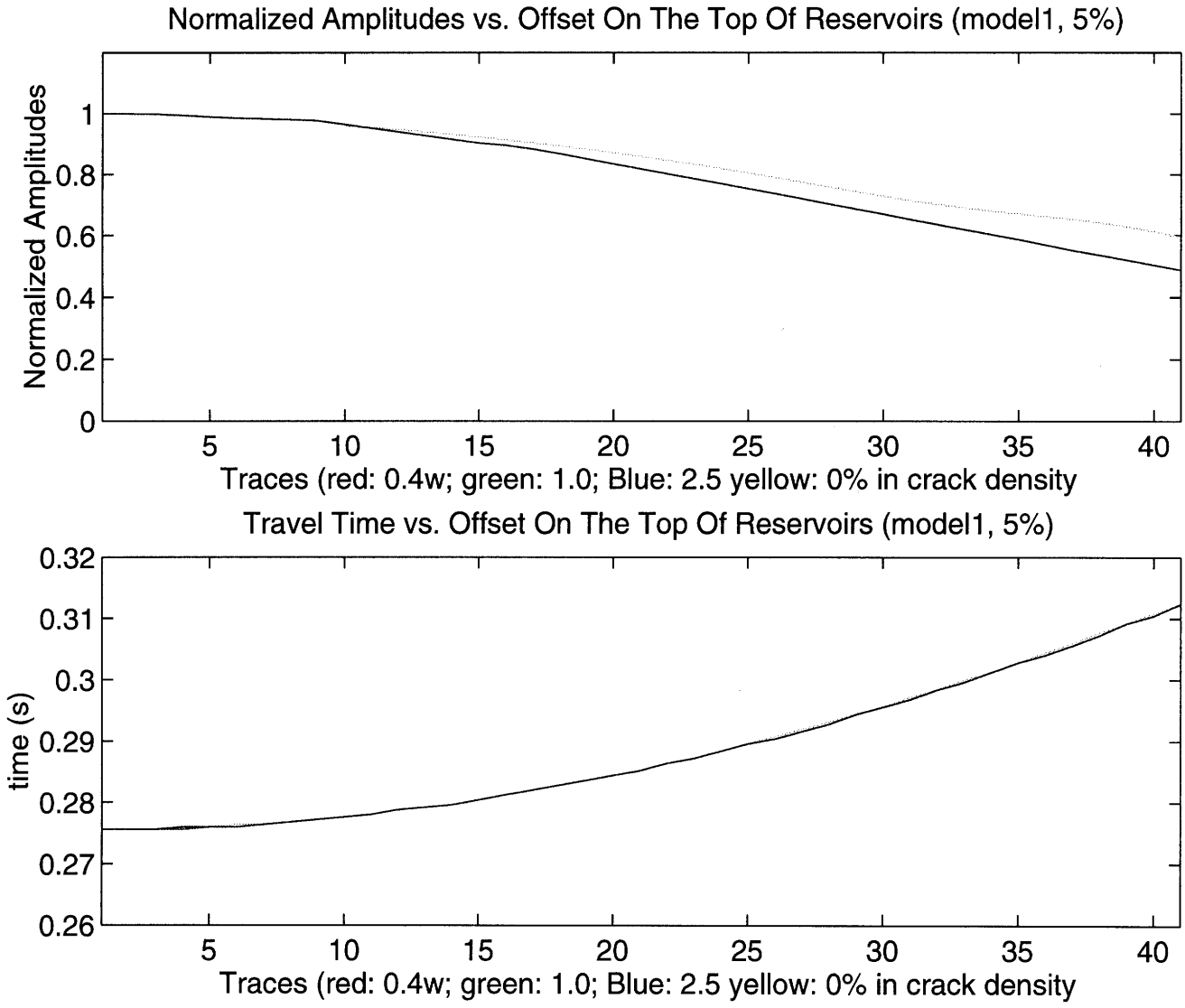

Figure 3-6 Normalized amplitudes vs. offset (trace) at the top of fractured reservoirs in model 1 from fracture realization models and fracture strike direction (upper plot, 6a). Travel time vs. offset (trace) at the top of fractured reservoirs in model 1 from fracture realization models and fracture strike direction (lower plot, 6b).

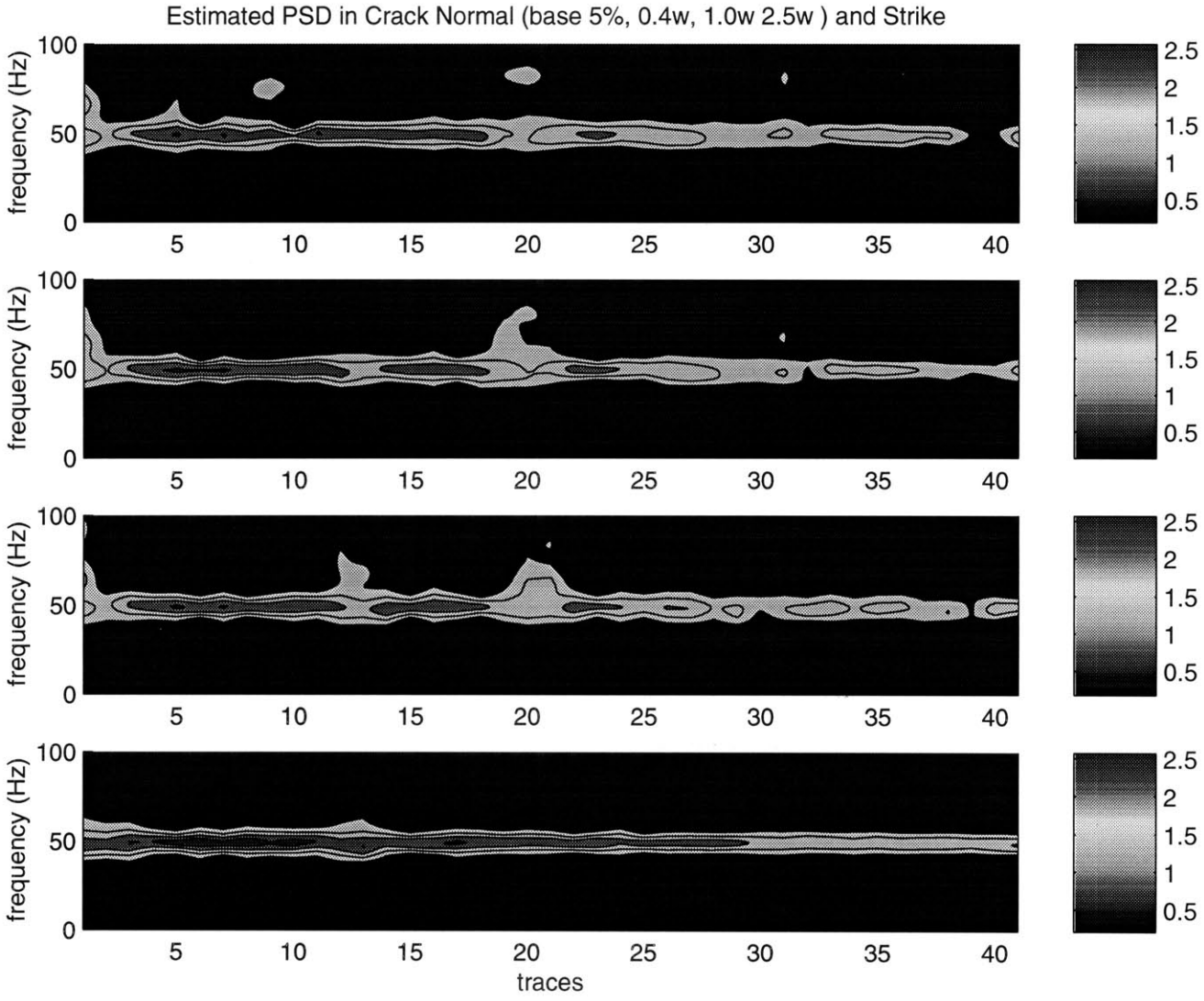

Figure 3-7 Power spectral image varies with frequency and offset (trace) at the base of the fractured reservoirs in model 1. From the top to the bottom, results are estimated from fracture realization models with correlation length 0.4, 1.0 and 2.5 wavelength and fracture strike direction.

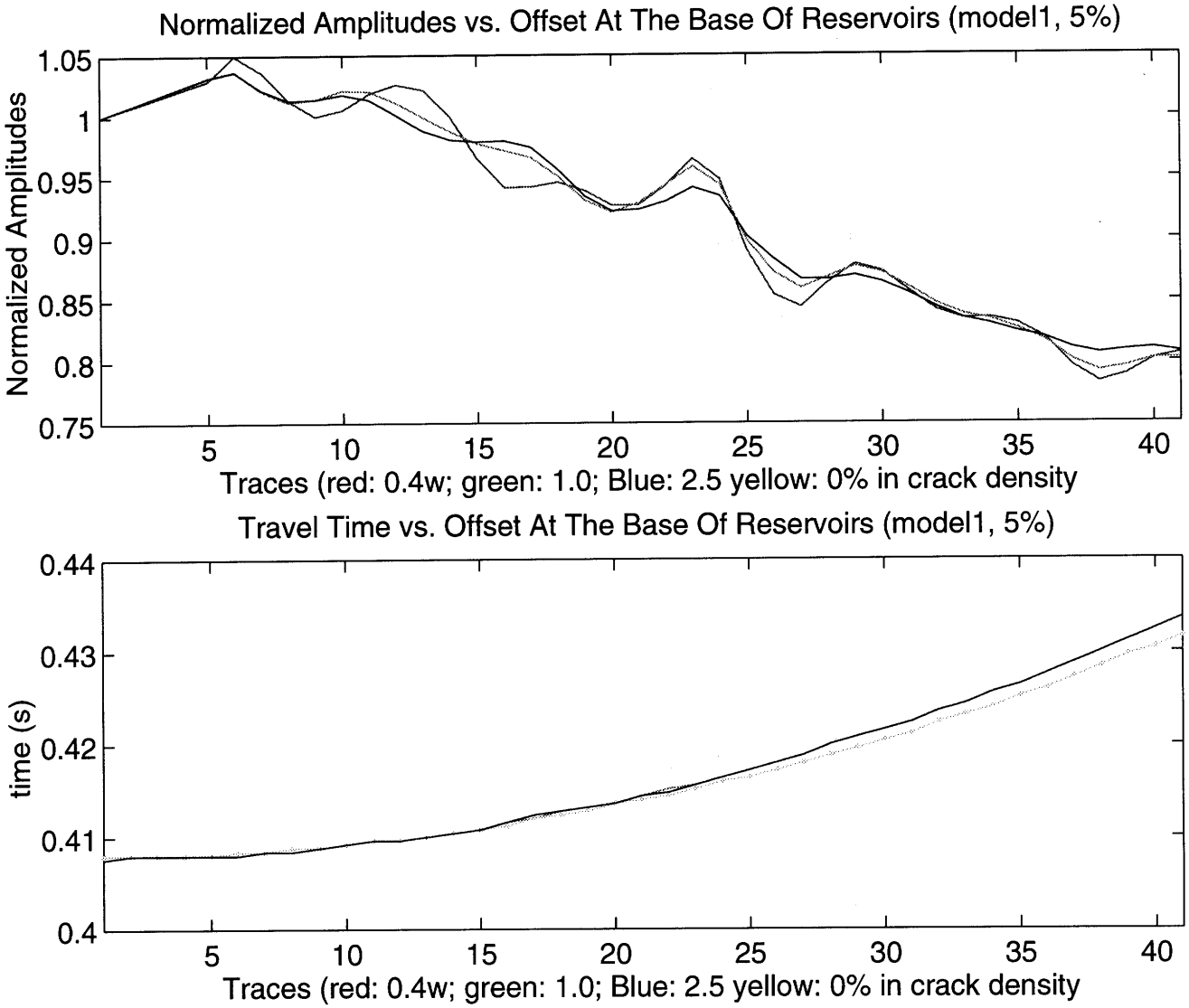

Figure 3-8 Normalized amplitudes vs. offset (trace) at the base of fractured reservoirs in model 1 from fracture realization models and fracture strike direction (upper plot, 8a). Travel time vs. offset (trace) at the base of fractured reservoirs in model 1 from fracture realization models and fracture strike direction (lower plot, 8b).

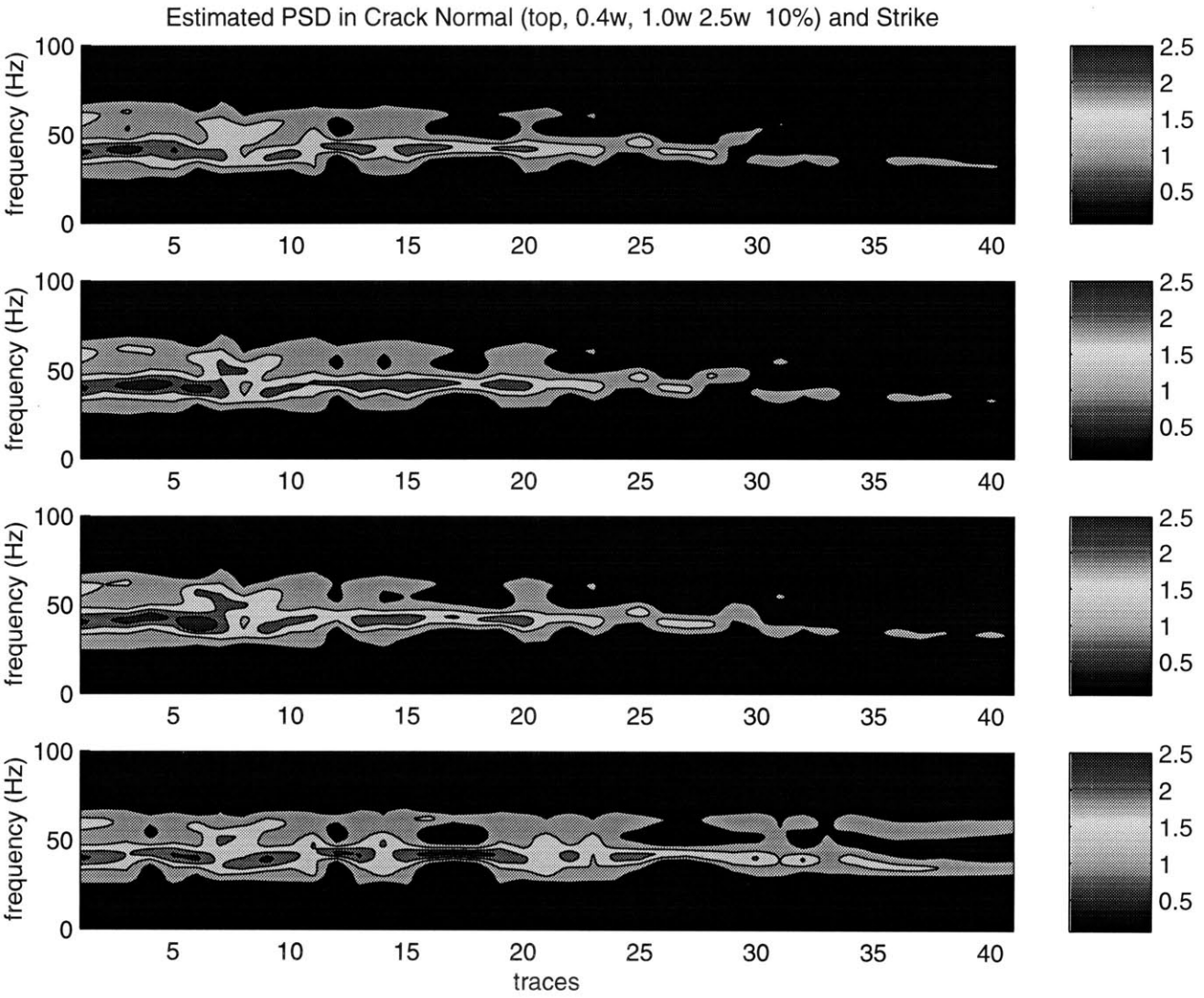

Figure 3-9 Power spectral image varies with frequency and offset (trace) at the top of fractured reservoirs in model 1 (with larger scatter density). From the top to the bottom, results are estimated from fracture realization models with correlation length 0.4, 1.0 and 2.5 wavelength and fracture strike direction.

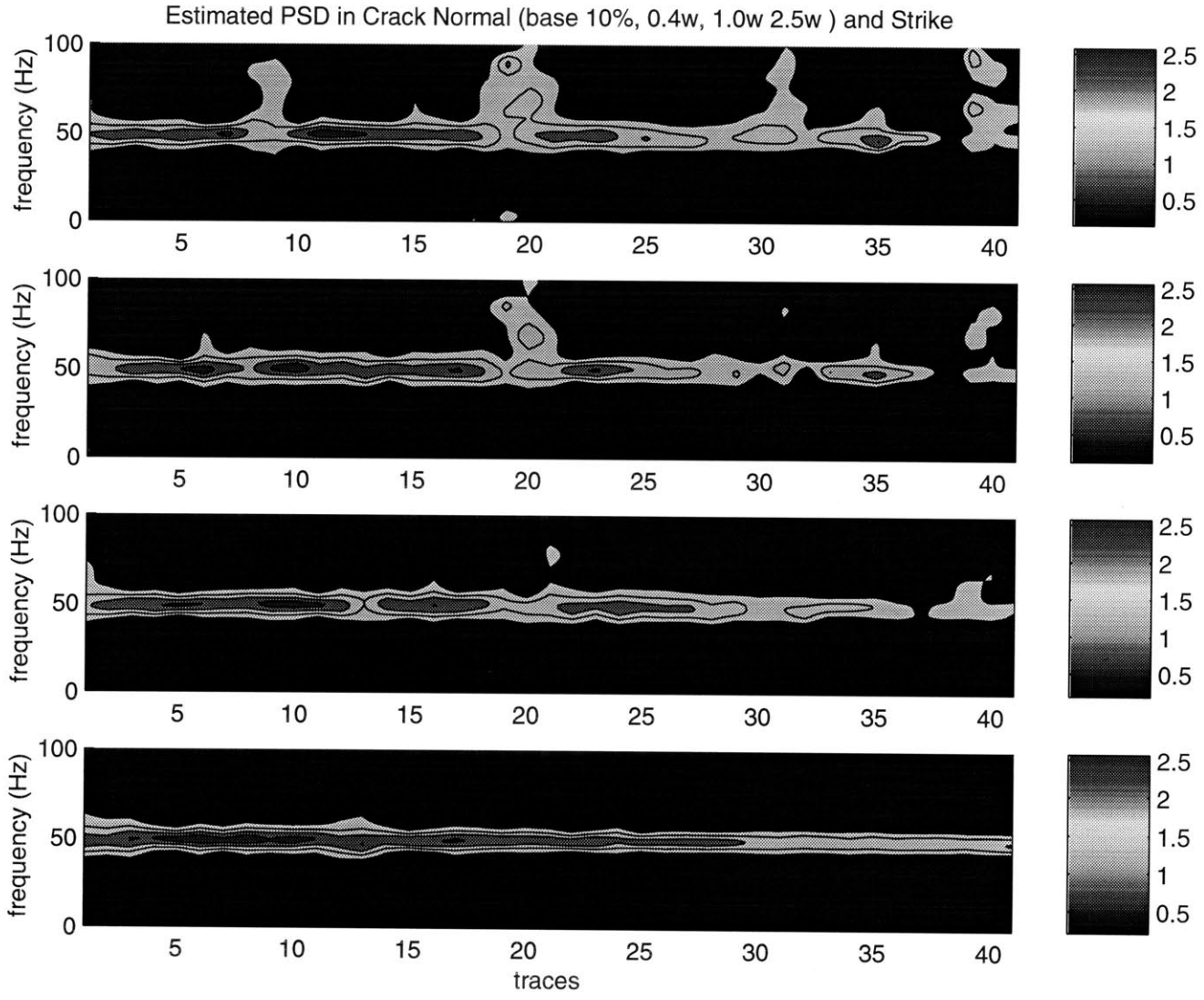

Figure 3-10 Power spectral image varies with frequency and offset (trace) at the base of the fractured reservoirs in model 1 (with larger scatter density). From the top to the bottom, results are estimated from fracture realization models with correlation length 0.4, 1.0 and 2.5 wavelength and fracture strike direction.

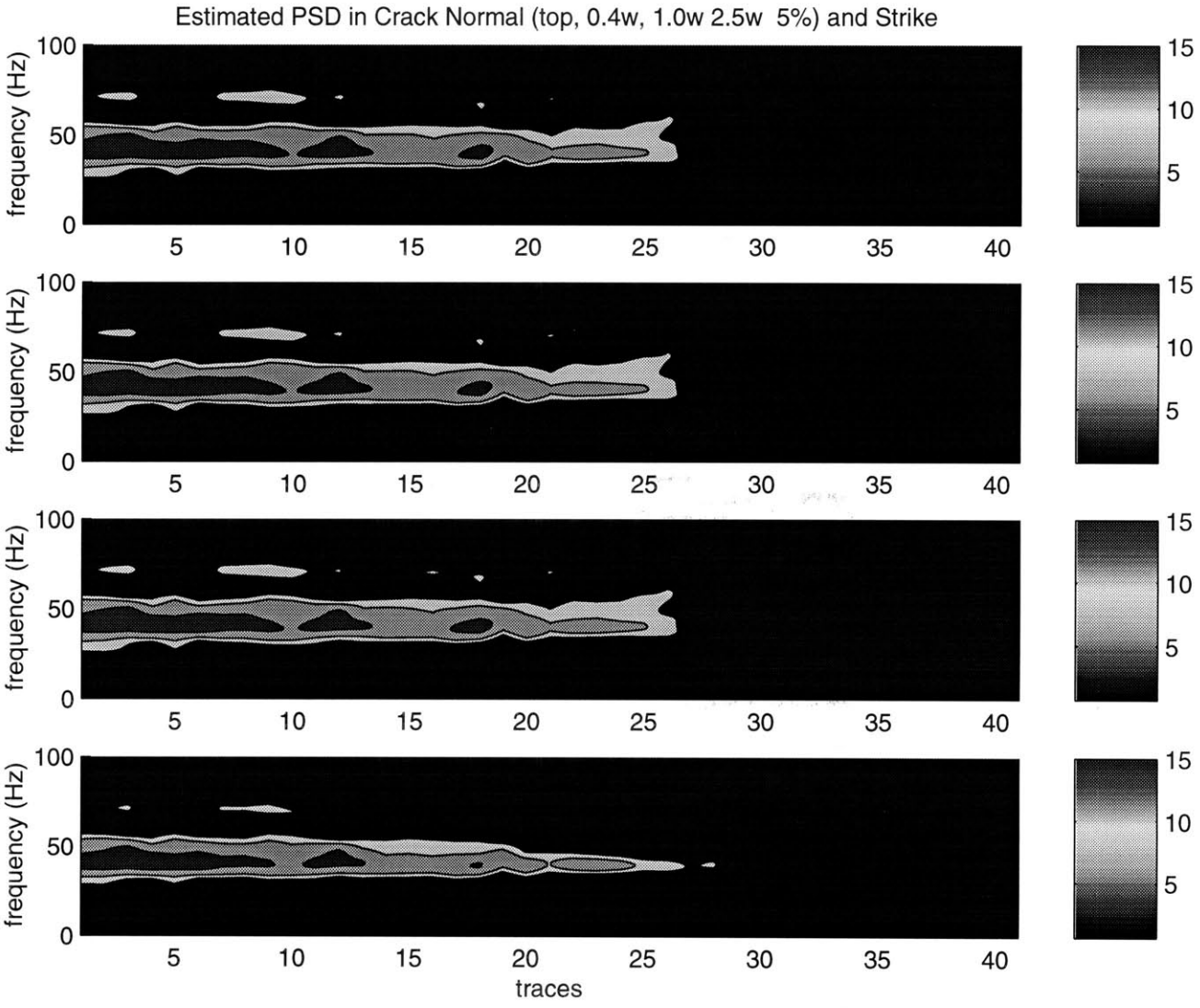

Figure 3-11 Power spectral image varies with frequency and offset (trace) at the top of the fractured reservoirs in model 2. From the top to the bottom, results are estimated from fracture realization models with correlation length 0.4, 1.0 and 2.5 wavelength and fracture strike direction.

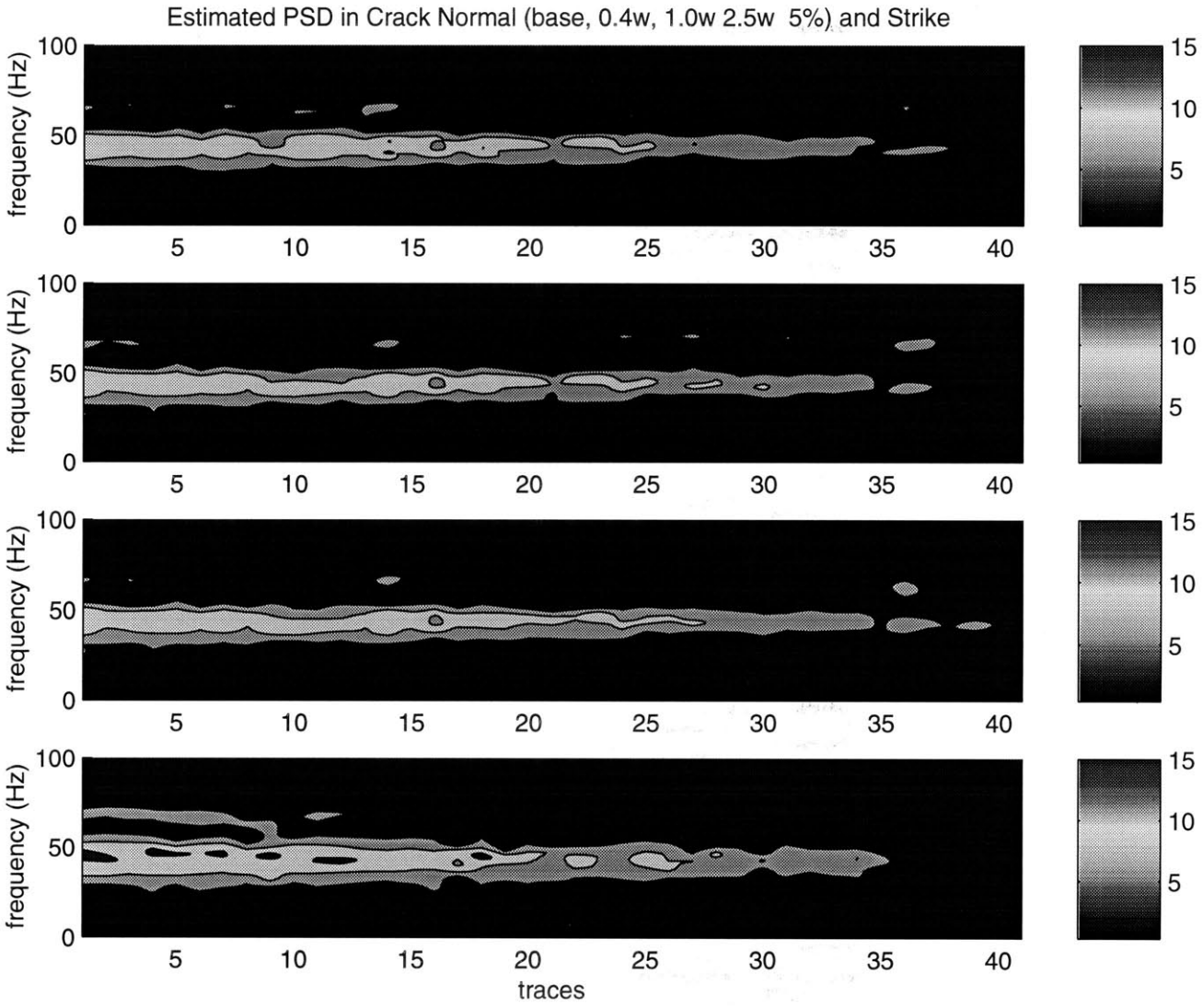

Figure 3-12 Power spectral image varies with frequency and offset (trace) at the base of the fractured reservoirs in model 2. From the top to the bottom, results are estimated from fracture realization models with correlation length 0.4, 1.0 and 2.5 wavelength and fracture strike direction.

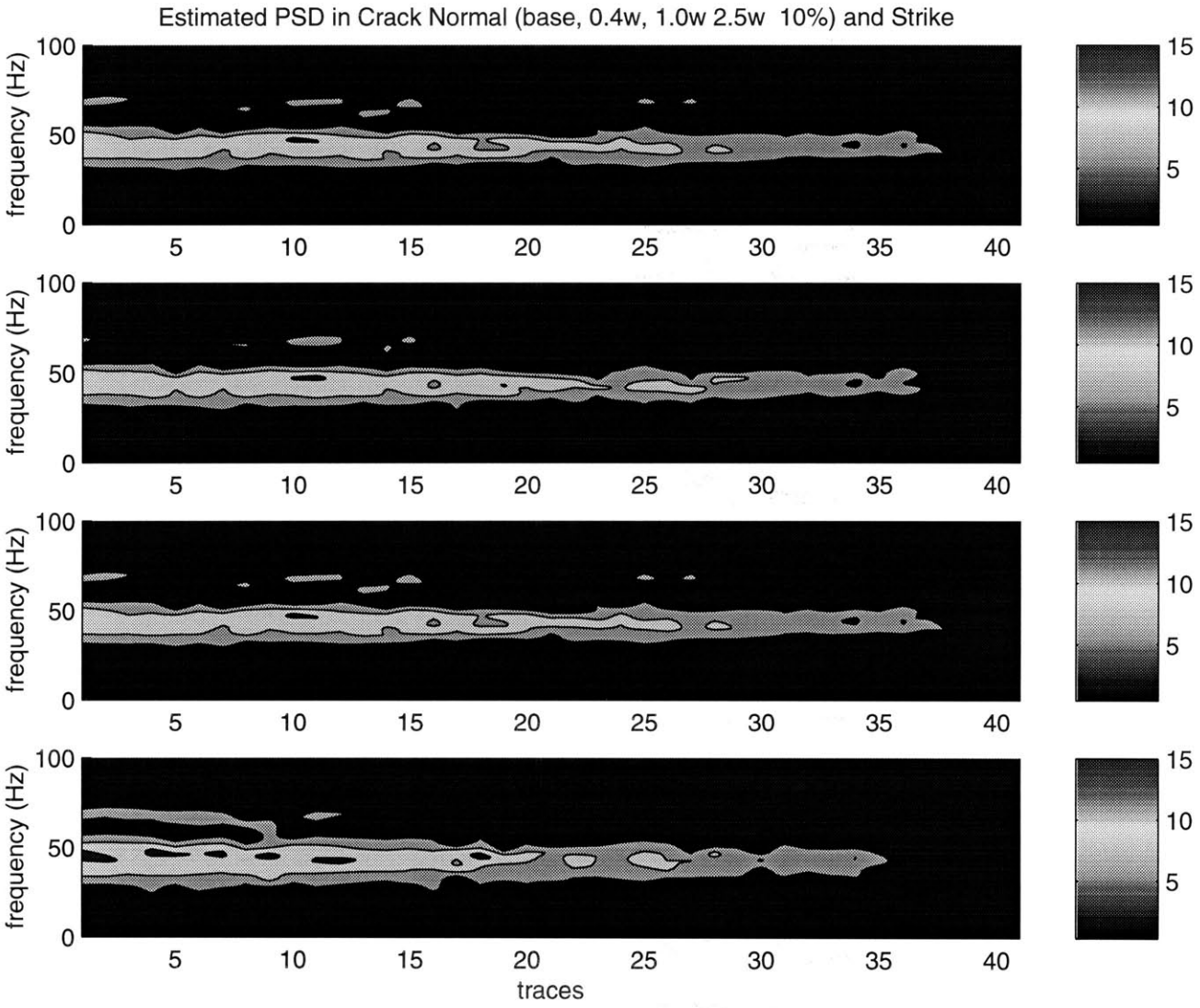

Figure 3-13 Power spectral image varies with frequency and offset (trace) at the base of the fractured reservoirs in model 2 (with larger scatter density). From the top to the bottom, results are estimated from fracture realization models with correlation length 0.4, 1.0 and 2.5 wavelength and fracture strike direction.

CHAPTER 4

Azimuthal offset-dependent attributes (AVO and FVO) applied to fracture detection

4.1 ABSTRACT

The possibility of the diagnostic ability of P-wave seismic data in fracture detection by using the amplitude versus offset (AVO) and the frequency versus offset (FVO) information is investigated. The offset-dependent attributes (AVO and FVO) are estimated by using an eigenvector based estimation technique, the multiple signal classification frequency estimator. These attributes are applied to the determination of principal orientation of fractures in carbonate fractured reservoirs located in the Maporal field in the Barinas basin in southwest Venezuela. Our studies show that P-wave reflectivity is characterized by a large increase of amplitude with offset (large positive AVO gradient) and a large frequency decay with offset (large negative FVO gradients) in the crack normal direction. In the crack strike direction, P-wave reflectivity is characterized by a wide variation range of AVO gradient but a small variation of FVO. The analyses of inverted offset-dependent velocities and theoretical calculations show that lateral heterogeneity in the reservoir zone leads to large variations of AVO gradients. The offset-dependent frequency attribute can help lessen the ambiguity in fracture detection. The combination of the offset-dependent frequency attribute is more beneficial than using the offset-dependent amplitude attribute alone.

4.2 INTRODUCTION

With advanced horizontal drilling technology, determining fracture orientation is very important. Well log data can be used for fracture detection but are limited to well locations. Geologic observations can be used to predict fracture orientation but only with certain assumptions. Seismic data have wider spatial coverage than well data, and this fracture estimation from seismic data becomes important for practicality. It is known that

vertically aligned fractures in a reservoir induce seismic anisotropy. Shear wave splitting can be observable in fractured reservoirs and is very sensitive to the fracture orientation and density. However, high acquisition cost of multicomponent data makes this method expensive to apply on a regular basin. In addition, processing of multicomponent data requires technology that the seismic industry has not yet fully developed. Using P-wave data to detect fractures is very promising and has been of growing interest to the exploration geophysical community over the past few years.

Studies show that the effect of vertically aligned fractures on P-wave reflectivity is a function of offset and cannot be detected by conventional normal incident seismic data. For this reason, fracture studies based on seismic data analysis have been extended to prestacked seismic data. Determining the principal orientations of vertically aligned fractures from P-wave data presently depends on velocity analysis studies for different common midpoint (CMP) locations and on AVO studies for different azimuthal angles. Neidell and Cook (1986) use the differential informational stacking velocity analysis method to identify subsurface fracture zones from P-wave data. They claim that the anomalous velocity zones are related to fractures. Paul (1993) attributes anomalously low stacking velocities to the presence of localized fractures. The similar phenomena of stacking velocity anomalies induced by fractures are observed by Lynn et al. (1995) and Corrigan et al. (1996). If the fracture layer has a small thickness, the application of P-wave stacking velocity is limited because the azimuthal travel time depends on fracture parameters and the thickness of the fractured reservoir. In contrast to stacking velocity analysis methods, azimuthal AVO studies, relying on the reflection amplitudes, have been used to detect fractures (Perez and Gibson, 1996; Ramos and Davis, 1997; Mallick et al., 1998). Generally, amplitudes are related to reflection coefficients and thus to elastic contrasts. The predication of fracture orientation based on azimuthal variations is still ambiguous when *a apriori* knowledge of some variables, such as layer thickness, fluid contents and spatial heterogeneity, are not available. Therefore, other seismic parameters, in addition to AVO, are needed to reduce the ambiguities and constrain solutions in the interpretation of fractured reservoirs. Finding additional parameters appears to be feasible in prestacked domains because the seismic signal can be parameterized in terms of amplitude, phase and frequency versus offset. Mazzotti (1991) applies instantaneous amplitude, phase and fre-

quency versus offset (APF.VO) indicators to investigate the possibility of a diagnostic value of seismic data and shows that modifying the velocities and thicknesses of a given target layer, by introducing different pore fluids or lithological conditions, produces changes in instantaneous APF.VO plots in synthetic seismograms. Moreover, Mazzotti (1991) finds that the amplitude indicator appears to be reasonably stable while the phase indicator has a higher spatial variability and a stronger sensitivity to noise.

Based on a 3-D finite difference modeling technique, studies in heterogeneous, fractured reservoirs show that, with increase in offset in addition to the azimuthal AVO variations, frequencies of power spectral peaks (signal frequencies) in the crack normal direction shift toward a lower frequency range than those in the crack strike direction. Additionally, at the top of fractured reservoirs, the characteristic of frequency versus offset (FVO) is dominated by the mean of fracture density (Shen and Toksoz, 1998).

In this chapter, we demonstrate the application of AVO and FVO analyses to the detection of the principal orientation of fractures from azimuthal P-wave seismic data in the Maporal field, in the north-central portion of the Barinas-Apure Basin, Venezuela. Our seismic data analysis consists of studying seismic trace morphology and estimating offset-dependent attributes by using a frequency estimator in three seismic survey lines. We relate these offset dependent attributes to fracture properties and analyze their lateral variations. By combining offset-dependent velocity analyses with theoretical calculations, we investigate the effects of background properties on AVO signatures. Our purpose in this study is to show that the combination of offset-dependent frequency attributes is more beneficial than using the offset-dependent amplitude attribute alone.

4.3 SEISMIC FIELD DATA

The Maporal field is located in the north-central portion of the Barinas-Apure Basin, in the southwestern part of Venezuela. Two-dimensional, three component seismic data were acquired in this field. Three 10 km seismic lines are centered over the areas of interest and cover three azimuths. There are two systems of normal faults: one runs northeast-southwest and the other northwest-southeast. The geometry of seismic lines and well log locations is shown in Figure 1. The azimuths of line 3 and line 1 are almost parallel to the northwest-southeast and northeast-southwest fault systems, respectively; the third line

(line 2) almost bisects them and forms an angle of approximately 40^{o} with line 1. A charge of one kilogram explosives at 10 m depth was used for the source. The shotpoint space intervals are 51m, and the source offset is 17m. The near offset is 17m and the far offset can extend to about 3600 m. The maximum fold is 33. The detailed survey parameters can be found in Table 2 of Ata and Michelena (1995).

Like acquisition operations, processing operations also play an important role in seismic data quality control. Ground coupling of sources and receivers, source-receiver patterns and near surface conditions are partial causes of distortion of true amplitudes. Our processing sequence aims to remove these distorting effects and increase the signal to noise ratio and preserve true amplitudes. We avoid adaptive processes such as signal-trace deconvolution, spectral whitening, and amplitude scaling. The processing sequence applied to the three lines includes true amplitude recovery, F-K filter, refraction statics, CMP sorting, normal moveout (NMO) and residual statics. This sequence is summarized in Figure 2. After a two-passes velocity analysis, the following steps are performed: trace editing and bandpass filtering. The reflection amplitudes are not biased by processing algorithms, so the amplitudes can be used to obtain offset-dependent seismic attributes to characterize fractured reservoirs. Considering that reservoirs are near the intersection point of the three lines and that azimuthal comparison of offset-dependent attributes are conveniently made, a subset of data is selected from the whole data set for this study. Sixty CDPs in each line are used in our attribute estimation from CDP 221 to CDP 280. The three lines intersect each other around CDP 224.

The reservoir is in the member 'O' of the upper Cretaceous Escandalosa formation at a depth of approximately 3000m. It consists of dolomitic carbonate and carbonate that contains primary fractures, revealed by televiewer logs. Member 'O' overlays members 'P' and 'R', which are composed mainly of sandstones and shales. To locate the target zone in the seismic profile, synthetic seismograms are generated by using sonic logs from wells that intersect or are close to these lines. The wavelet is extracted from the well logs. Figure 3 shows the synthetic seismograms generated from Well 13 and tied with the stacked P-wave section of line 1. The fractured limestone reservoir is around 2300 m/s in seismic profiles and characterized by strong reflectivity.

4.4 ESTIMATION OF OFFSET-DEPENDENT ATTRIBUTES

On average, the P-wave seismic data have a peak frequency around 25Hz at the reservoir zone. Using an interval velocity of about 5100 m/s, the corresponding tuning thickness is 39.2 m (with the thickness=λ/5.2, where λ is the wavelength of the seismic pulse at the peak frequency), or 15 ms in terms of travel time). The thickness of member 'O' does not vary greatly over the research CDP range (60 CDPs, 1.06km), averaging 30 m (12 ms in terms of travel time). Studies from Ramos and Davis (1997) show that tuning has an important effect on the magnitude of AVO gradients and that varying the thickness of a reservoir can lead to variations of AVO gradients when the maximum thickness is smaller than half a wavelength. To investigate the distortion of tuning on azimuthal variations of AVO and FVO, we use the same background model parameters as in previous studies (Shen and Toksoz, 1998) and decrease the thickness of the fractured reservoir to within λ/4. We find that tuning distorts AVO and FVO properties in homogeneous fractured reservoirs in the crack normal and strike directions. However, the azimuthal variations of AVO are still observable and frequency decay with offset (FVO) in the crack normal direction is still greater than that of the crack strike direction. Considering that the variations in the thickness of the reservoirs are small in our research area, the tuning effect should be similar for most of the data in our analysis; i.e., the tuning effect should produce similar changes in the magnitude of the AVO gradient in the three lines. The azimuthal variations of seismic attributes are still valid in detecting the principal orientation of fractures.

The prestacked CDP gathers in the reservoir target zone are characterized by increasing amplitudes from the near offset to the far offset. Anisotropic surface resolution arises from the oblique incident angles and leads to high resolution in near to middle offset traces and low resolution in far-offset traces. The spatial resolution variation can be explained by the fact that an impinging planar wave has maximum spatial resolving power in the direction of the propagation and no resolving power in the perpendicular direction. In between the two directions, the resolving power drops off as the cosine of the incident angle (Levin, 1998). Therefore, a real stretch is contained in nonzero offset data. However, for data with similar offset ranges, the stretch is approximately equal in our data. The azimuthal variations of seismic attributes are still valid in detecting the principal orientation

of fractures when the spatial stretch is considered.

Additionally, reflection seismic waveforms in the near to middle offset are different from those in the far offset in trace morphology and show large variations in amplitudes, lateral continuity, total energy and energy distributions. Based on the characteristics of CDP gathers in trace morphology, we classify CDP gathers in the three seismic survey lines into two groups: near-middle offset and far offset. The average far offset range for the three lines is from 2000 to 3550 m. CDP gathers with different characteristics in seismic morphology from CDP 245 to CDP 249 in the three lines are shown in Figure 4. It can be found from Figure 4 that far-offset data in CDP gathers are more stable and have smaller lateral variations in seismic morphology than these near-middle offset amplitudes.

Partial stack amplitudes over near-middle offset data are generated on the NMO corrected gathers (denoted as near-middle poststack amplitudes). Poststack amplitudes with far-offset data and with full range of offset data are also generated, respectively (denoted as far-offset poststack amplitudes and overall poststack amplitudes). These three kinds of stacked seismic profiles are shown in Figure 5. The characteristics of far offset, poststack amplitudes in line 1, line 2 and line 3 are comparable with those of overall poststack amplitudes. this similarity indicates that the contribution of far offset amplitudes to overall poststack amplitudes is greater than that of near-middle offset amplitudes and that far-offset amplitudes dominate the properties of overall poststack amplitudes. Moreover, near-offset amplitudes are most related to background lithological properties. In fractured reservoirs, the effects of fractures on reflection amplitudes in off fracture strike directions increase with increasing offset. Far offset reflection data contain more information about fractures than near-middle offset data. Therefore, offset dependent attributes estimated from seismic waveforms with approximately equal far offset ranges are still valid in detecting fractures.

In CDP gathers, far-offset traces are more stable and have smaller lateral variations in seismic morphology than those of near-middle offset. In order to obtain the robust offset-dependent attributes and decrease the errors caused by rapid lateral morphology variations in near-middle offset traces and caused by interference among reflections, classified far offset seismic waveforms are used to estimate offset-dependent attributes instead of seismic waveforms with the full range of offset. Because the time window corresponding to

the reservoir depth interval has little variation in the far-offset range, we analyze the CDP gathers in a constant time window of 40 ms, starting from the top of the reservoir trough and including 21 samples. Seismic attributes used to determinate fracture orientation are derived from these waveforms within the time window length. The measured seismic waveforms at the time gate of the reservoir zone actually correspond to an averaged medium composed of carbonates and interbedded non-carbonate materials (typically shales) and sands from the 'P' member beneath the member 'O'.

We apply a technique--the multiple signal classification method--to extract AVO and FVO attributes in the frequency domain from windowed seismic waveforms. This method is based on an eigenanalysis of an autocorrelation matrix and separates information in the autocorrelation matrix into two vector subspaces, one a signal space and the other a noise space. Functions of the vector in either the signal or noise space can be used to create frequency estimators. The power spectral peak values estimated by the frequency estimator represent the strength of the signals. The signal locations in the frequency range indicate the signal frequencies. Note that the frequency estimator is a pseudo spectrum estimator because the autocorrelation sequence cannot be recovered by Fourier transforming the frequency estimator. A detailed discussion about the frequency estimator can be found in Schmidt (1986) and Johnson and Degraaf (1982). This method also has been used in fracture scattering studies and discussed in Shen and Toksoz (1998).

Figure 6 shows the normalized P-wave power spectra and their frequencies for the reflection at the fractured reservoir zone as a function of offset, corresponding to the CDPs shown in Figure 4 for the three lines. A linear regression, based on the criterion of the least absolute deviations, is used to obtain gradients of amplitudes (power spectra) and frequencies with offset. Because we are interested in the variations of amplitudes with offset, the P-wave amplitude (power spectra) of each CDP is normalized by the amplitude (spectrum) with the smallest offset. This normalization does not affect the comparative analysis in azimuth. The obtained AVO estimates are relative values and do not correspond to direct measurements of rock properties.

To check the estimated results qualitatively, RMS amplitudes are calculated, and AVO gradients are obtained by straight-line fitting in windowed seismic waveforms in the time domain. The lateral variations of AVO gradients from the two estimation methods are con-

sistent for the three lines, which confirms the reliability of the frequency estimator.

4.5 AZIMUTHAL AVO AND FVO ANALYSES

Frequency-dependent (AVO and FVO) attributes are estimated from a total of 180 CDPs in three lines and show specific characteristics. Line 1 is characterized by positive and large AVO gradients varying laterally from small to large CDP numbers. Large AVO gradients distribute between CDP 235 and CDP 260. For CDPs between 270 and 280, AVO gradients become small and have small lateral variations. FVO is characterized by decreasing frequency with offset. FVO gradients tend to have large negative values between CDP 220 and CDP 260. Beyond CDP 260, frequency decay with offset becomes small. Line 3 has lower positive AVO gradients than those of line 1 from CDP 220 to CDP 260. Beyond CDP 260, AVO gradients increase and become comparable with those of line 1. Overall FVO gradients have small values and small lateral variations, thus frequency variations with offset are small. In line 2, both AVO and FVO gradients have small lateral variations. The average AVO gradients in this line are smaller than those in line 1 and frequency gradients are smaller than line 1 but greater than line 3.

The distributions of the CDPs of three lines in attribute space are shown in Figure 7. The CDPs, not being overlaid, in three lines show their own specific characteristics which separate them in attribute space. CDPs with a red star in line 1 are characterized by a large increase in amplitude with offset and a large frequency decay with offset. CDPs with a green plus in line 2 are characterized by a small increase in amplitudes with offset and a moderate frequency decay with offset. CDPs with a blue circle in line 3 show that line 3 has a wide rang of AVO gradients but is characterized by the smallest frequency variations with offset. We also project the CDPs from attribute space to geometry space to demonstrate their variations in geometry space. If the azimuthal variations in AVO and FVO gradients can be attributed to the effects of fractures, the three lines have different orientations relative to the principal orientation of fractures.

In order to relate clusters of AVO and FVO attributes to fracture interpretation, insight into P-wave azimuthal AVO variations is calculated by using an approximation reflection coefficient equation (Ruger, 1998). Elastic parameters derived from sonic and density logs acquired from well 17 are listed in Table 1. Anisotropic parameters were derived from

Hudson's (1981, Hudson et al., 1996) crack model and Tsvankin's (1996, 1997) expressions. The parameters used in the calculation are listed in Table 1. Our results show that the fluid filled, open fractures can give rise to larger amplitude increase with offset in the fracture normal direction than in the fracture strike direction. Scattering studies show that the frequency has larger decay in the crack normal direction than in the crack strike direction (Shen and Toksoz, 1998). Therefore, line 1 is the line most perpendicular to the principal orientation of fractures and line 3 is the one most parallel to the principal fracture orientation. Since the properties of offset-dependent attributes in line 2 are close to those of line 1, it should be close to perpendicular to the principal fracture orientation. This interpretation is consistent with studies by Ata and Michelena (1995) who use P-SV converted waves to estimate fracture orientation and map fracture density. Their studies, correlated with well data, show that fracture orientations tend to run subparallel to the fault systems which cut the reservoir and that the major fault system is parallel or subparallel to line 3.

4.6 EFFECTS OF BACKGROUND PROPERTIES ON AVO SIGNATURES

Studies show that azimuthal AVO variations in fractured reservoirs are influenced by fracture parameters including fracture density, fluid content and fracture aspect ratio. In Maporal field member 'O', the material filling the crack system is expected to be gas, oil and water. Since the oil bulk modulus is between the gas and water, the azimuthal AVO variations of oil-saturated fractures are expected to vary between gas and water. Figures 8a and 8b show, in the crack normal direction, the P-wave AVO responses versus crack density at the top of gas- and water-saturated, fractured reservoirs, respectively. Background elastic parameters are taken from Table 1. Fractures have little effect on P-wave reflectivity except for intermediate incident angles. As crack density increases, the magnitudes of AVO gradients also increase. By comparing Figures 8a and 8b, we find that, with equal fracture density, water-saturated, fractured reservoirs have larger AVO gradients than those of gas-saturated, fractured reservoirs. However, the difference in AVO gradients is very small. For example, for the reservoirs with 10% crack density, 0.01 fracture aspect ratio and filled by gas and water, respectively, the difference in AVO gradient is only 2% in

the crack normal direction for a 30^{o} incident angle. Therefore, although fracture density and fluid content have effects on AVO signatures in off fracture strike directions, our calculations show that the fluid content has a small influence on AVO gradients in these directions.

Another important non-fracture factor influencing the azimuthal AVO variations is background elastic properties, including average Vp, Vs and ρ and their contrasts. A detailed discussion can be found in Shen et al. (1997). As mentioned above, near-middle offset amplitudes are most related to background lithological properties, and far-offset amplitudes contain more information about fractures than near-middle offset amplitudes. To investigate the effect of background heterogeneity on far-offset, azimuthal AVO gradients and understand the large variations of AVO gradients in line 3, we invert the interval velocities from near-middle poststack amplitudes and overall poststack amplitudes. In line 1, velocities inverted from near-middle offset, poststack amplitudes in the reservoir member 'O' gradually decrease from small to large CDP numbers and have smooth lateral variations (Figure 9a). If the far-offset, poststack amplitudes have a uniform contribution to near-middle, poststack amplitudes, the lateral variations of velocities from near-middle offset and overall poststack amplitudes could be comparable. However, the velocities inverted from overall poststack amplitudes have peak velocities around CDP 250 even though the average velocities between CDP 200 and 270 are larger than those between CDP 270 and 300 (Figure 9b). The difference in interval velocities between Figures 9a and 9b indicates that the far-offset amplitudes have a non uniform contribution to near-middle offset amplitudes, and the lateral variations of poststack amplitudes are different from each other. Furthermore, lateral velocity variations inverted from overall poststack amplitudes are consistent with those of AVO gradients in far-offset amplitudes. Therefore, the lateral variations of AVO gradients can be interpreted to be the result of fractures rather than background elastic properties. In line 2, velocities from near-middle offset and overall poststack amplitudes are comparable with each other (Figure 10a and 10b). Both of them have small lateral variations in velocities and relatively high velocities distributed between CDP 236 and CDP 260. The comparable lateral velocity variations inverted from near-middle offset and overall poststack amplitudes result from small values and small lateral variations of AVO gradients in far-offset amplitudes. Interval velocities from near-

middle offset, poststack amplitudes in line 3 show strong lateral heterogeneity (Figure 11a). Velocities inverted from overall poststack amplitudes have comparable lateral variations (Figure 11b). Large velocities distribute along a small CDP rang, from 200 to 228, and a large CDP rang, from 264 to 300, and the lateral discontinuity of velocities inverted from overall poststack amplitudes still can be observed around CDP 232, 252 and 276. The lateral variation of AVO gradients obtained from far-offset amplitudes is consistent with this lateral velocity variation. Since line 3 is parallel to the principal orientation of fractures, the AVO gradients in far-offset amplitudes are directly controlled by background properties.

By using the fracture parameters, including fracture density, fracture aspect ratio and fluid content, and elastic parameters in the Table 1, our calculation from the approximated reflection equation shows that only the variation of background P- and S-wave velocities in the reservoir layer can lead to large variations of AVO gradients both in the crack normal and in the crack strike directions for a 30^{o} incident angle. In the crack strike direction, varying P- and S-wave velocities from 4500 m/s and 2569.5 m/s to 6500 m/s and 3711 m/s and keeping Vp/Vs constant in the reservoir layer can lead to AVO gradients varying from 13% to -5%; varying P-wave velocity from 4500m/s to 6000m/s and Vp/Vs from 1.38 to 2.0 and keeping S-wave velocities at 3250 m/s can give rise to AVO gradients varying from -13% to 7%. Furthermore, if the reservoirs are assumed to be gas-saturated and to have 10% fracture density, varying P- and S-wave velocities from 4500 m/s and 2569.5 m/s to 6500 m/s and 3711 m/s and keeping Vp/Vs constant in the reservoir layer can lead to the variation of AVO gradients in the crack normal and strike directions from 9.3% to 8.28%; varying P-wave velocity from 4500m/s to 6000m/s and Vp/Vs from 1.38 to 2.0 and keeping S-wave velocities at 3250 m/s can give rise to the variation of AVO gradients in the crack normal and strike directions from 16% to 5.9%. These calculations show that background heterogeneity in the reservoir layer has an important effect on both AVO gradients in the crack strike direction and variations of AVO gradients in both the crack normal and the strike directions. Moreover, varying Vp and Vp/Vs and keeping Vs constant in the reservoir layer has a greater effect on azimuthal AVO variations than varying Vp and Vs and keeping Vp/Vs constant. Therefore, the reservoir lateral heterogeneity can be one of the major contributions to the wide variation range of AVO gradients in line 3. The

AVO signatures are not necessarily correlated with fracture parameters and the non-fracture factors also have an important effect on AVO gradients.

4.7 DISCUSSION AND CONCLUSION

We have demonstrated that AVO and FVO attributes estimated from seismic waveforms can be used to detect possible principal orientations of fracture systems in reservoirs with tuning thicknesses. Moreover, estimation based on waveforms can decrease the errors caused by residual velocity and inaccurate static correction. Statistic analysis in the attribute space is very helpful for identifying major characteristics of estimated attributes, particularly when the number of wells is limited and it is not possible to carry out quantitative calibrations. Offset-dependent attributes can be selected based on their capability of providing significant statistic relationships with the fracture information. Our results show that the CDPs in line 1 are characterized by a large increase in amplitudes with offset and large frequency decay with offset and that the CDPs in line 3 are characterized by a wide variation of AVO gradients and small frequency variations with offset. Line 2 is characterized by a moderate frequency decay with offset and smaller AVO gradients than those in line 1. Knowledge of the amplitudes and frequency variations with offset provide a better understanding of the P-wave reflectivity and yields further information about the reservoir properties.

Model analysis studies are very important and very helpful in the interpretation of estimated, offset-dependent attributes. Based on our theoretical calculation derived from well data, the highest AVO gradient is in the crack normal direction at the top of homogeneous fractured reservoirs. Previous studies show that the presence of fractures can lead to frequency decay with offset. If the azimuthal difference in AVO and FVO signatures can be attributed to the effects of fractures, line 3 is the closest to parallel or subparallel of the principal orientation of fractures, while line 1 is the closest to perpendicular to the fractures. Since line 2 is comparable with line 1, it is close to perpendicular to the fractures. This interpretation is consistent with the independent studies by Ata and Michelena (1995) with P-SV waves.

Although azimuthal AVO variations have been successfully used in fracture detection, our studies show that it is worthwhile to combine AVO analysis with FVO analysis. Both

fracture parameters (fracture density, saturated fluid content and fracture aspect ratio) and non fracture parameters (Vp, Vs and Vp/Vs of background rocks) can influence AVO gradients in the fracture strike direction and azimuthal AVO variations. Mazzotti's (1991) studies show that similar AVO trends can be obtained by using wavelets with different frequency bands and models with different thicknesses and that the frequency indicator is dominated mainly by the wavelet spectrum. Our calculation shows that for the reservoir with 10% fracture density, the difference in AVO gradients between water- and gas-saturated reservoirs in the crack normal direction is 2% and that the variations of Vp, Vs and Vp/Vs can lead to large variations in AVO gradients. Reservoir heterogeneity has an important effect on AVO signatures. Information about frequency variations with offset can help lessen the ambiguity in fracture detection.

Errors from estimation and physical interferences can contribute to distortion of the AVO and FVO estimates of gradients and intercepts. To check the validity of the straight-line fit and the oscillation in the amplitudes and frequency data, the mean absolute deviation from the fit lines is one criteria for measuring reliability. Studies from Ramos and Davis (1997) show that undulations in the normalized RMS amplitude data are caused by converted waves and coherent noise. Additionally, the CDPs with very limited offset ranges have a small degree of reliability. These errors should be considered when making interpretations using estimated attributes.

Acknowledgments

REFERENCES

Ata, E., and Michelena, R. J., 1995, Mapping distribution of fractures in a reservoir with P-S converted waves, The Leading Edge, 12, 664-676.

Corrigan, D., Withers, R., Darnall, J., and Skopinski, T., 1996, Fracture mapping from azimuthal velocity analysis using 3-D surface seismic data: 66th Ann. Internat. Mtg., Soc. Expl. Geophys., Expanded Abstracts, 1834-1837.

Hudson, J. A., 1981, Wave speeds and attenuations of elastic waves in material containing cracks, Geophys. J. Roy. Astr. Soc., 64, 133-150.

Hudson, J. A., Liu, E., and Crampin, S., 1996, Transmission properties of a plan fault,

Geophys. J. Int., 125, 559-566.

Johnson, D. H., and DeGraaf, S. R., 1982, Improving the resolution of bearing in passive sonar arrays by eigenvalue analysis, IEEE Transaction On Acoustics, Speech and Signal Processing, ASSP-30, 638-647.

Levin, S. A., 1998, Resolution in seismic imaging: Is it all a matter of perspective?, Geophysics, 63,743-749.

Lynn, H. B., Bates, C. R., Simon, K. M., and van Dok, R., 1995, The effects of azimuthal anisotropy in P-wave 3-D seismic, 65th Ann. Internat. Mtg., Soc. Expl. Geophys., Expanded Abstracts, 723-730.

Mazzotti, A., 1991, Amplitude, phase and frequency versus offset applications, Geophysical Prospecting, 39, 863-886.

Mallick, S., Craft, K. L., Meister, L. J., and Chambers, R. E., 1998, Determination of the principal directions of azimuthal anisotropy from P-wave seismic data, Geophysics, 63, 692-706.

Neidell, N. S., and Cook, E. E., 1986, Seismic method for identifying low velocity subsurface zones: US Patent 4 571 710.

Paul, R. J., 1993, Seismic detection of overpressure and fracturing: an example from the Qaidam Basin, People's Republic of China, Geophysics, 58, 1532-1543.

Perez, M., and Gibson, R., 1996, Detection of fracture orientation using azimuthal variation of P-wave AVO responses: Barinas field (Venezuela), 66th Ann. Internat. Mtg., Soc. Expl. Geophys., Expanded Abstracts, 1353-1356.

Ramos, A. C. B., and Davis, T. L., 1997, 3-D AVO analysis and modeling applied to fracture detection in coalbed methane reservoirs, Geophysics, 62, 1683-1695.

Ruger, A., 1998, Variation of P-wave reflectivity with offset and azimuth in anisotropic media, Geophysics, 63, 935-947.

Schmidt, R., 1986, Multiple emitter location and signal parameter estimation, IEEE Transaction On Antennas and Propagation, AP-34, 276-280.

Shen, F., and Toksoz, M. N., 1998, Scattering characteristics in heterogeneous fractured reservoirs from waveform estimation, 68th Ann. Internat. Mtg., Soc. Expl. Geophys., Expanded Abstracts.

Shen, F., Zhu, X., and Toksoz, M. N., 1997, Anisotropy of aligned fractures and P-wave

azimuthal AVO response, 67th Ann. Internat. Mtg., Soc. Expl. Geophys., Expanded Abstracts, 2001-2004.

Tsvankin, I., 1996, P-wave signatures and notation for transversely isotropic media: An overview, Geophysics, 61, 467-483.

Tsvankin, I., 1997, Reflection moveout and parameter estimation for horizontal transverse isotropy, Geophysics, 62, 614-629.

Table 5: Fracture Parameters, Elastic parameters and Anisotropic Parameters used in analytic calculations

Parameters	Shale	Carbonate
Vp (m/s)	3580	5692
Vs (m/s)	1875	3250
ρ (g/cm^3)	2.50	2.65
Fracture density		10%
fracture aspect ratio		0.01
$\varepsilon^{(v)}$ (gas)		-0.1752
$\delta^{(v)}$ (gas)		-0.1878
γ (gas)		0.1189
$\varepsilon^{(v)}$ (water)		-0.050
$\delta^{(v)}$ (water)		-0.1369
γ (water)		0.1189
γ (water)		0.1189

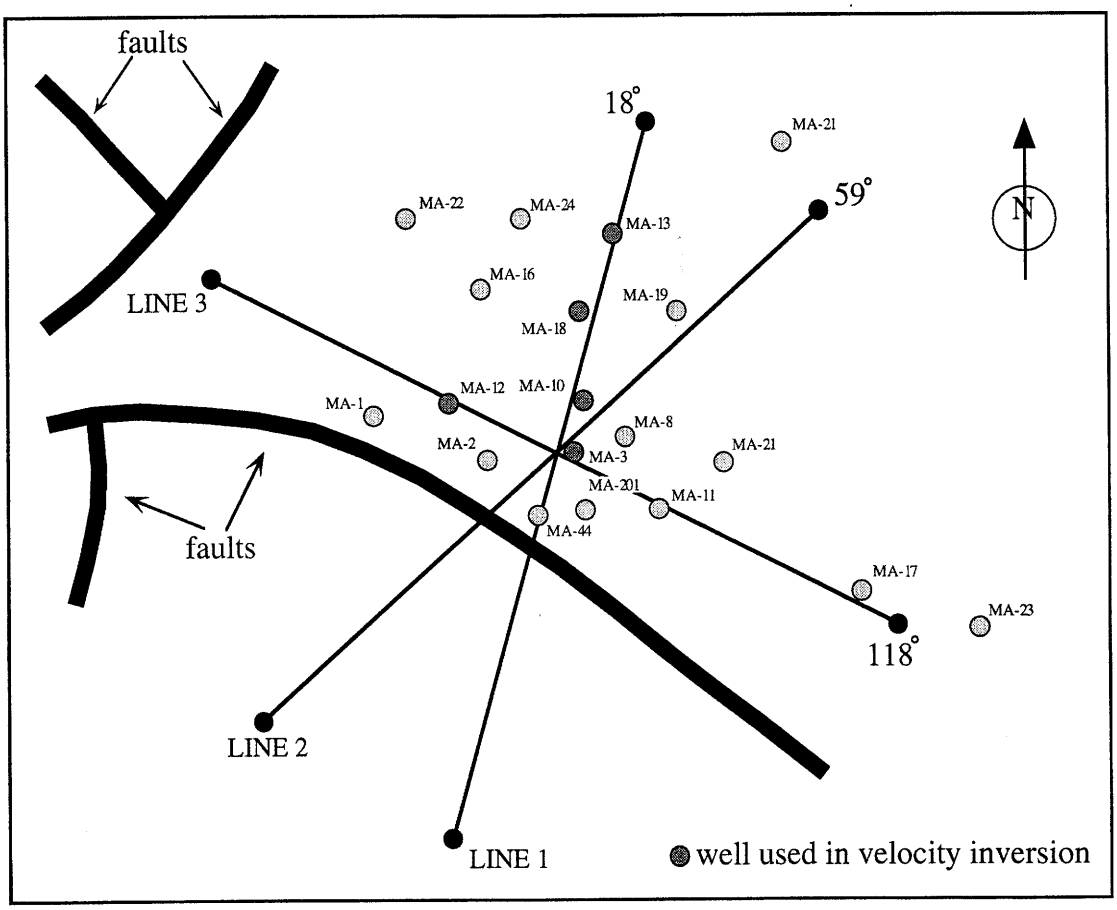

Figure 4-1 Locations of wells and two fault systems and geometry for three seismic survey lines in the Maporal field in the Barinas basin in southwest Venezuela (modified from Perez, M., 1997).

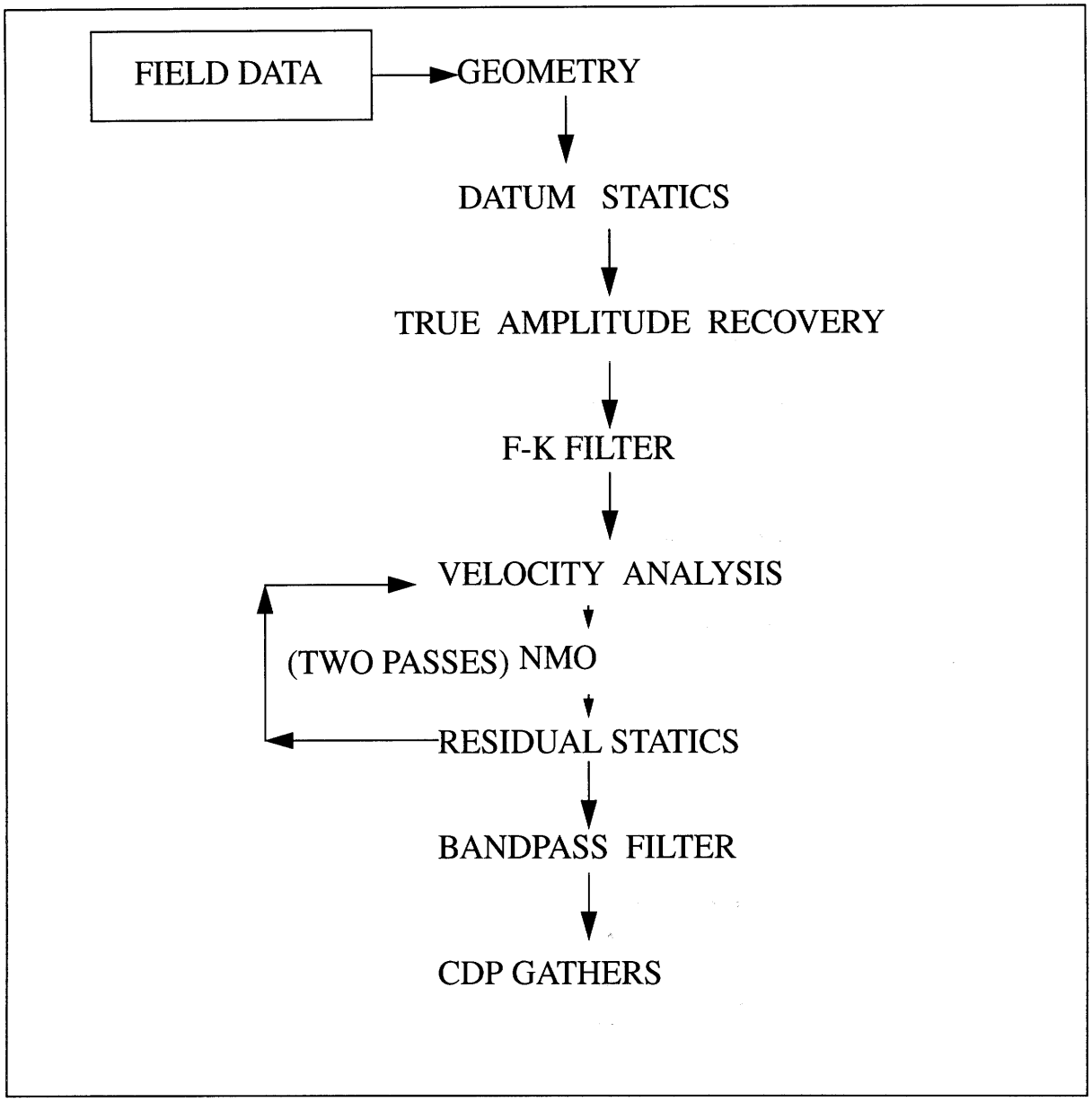

Figure 4-2 Data processing sequence used to obtain the prestack CDP gathers.

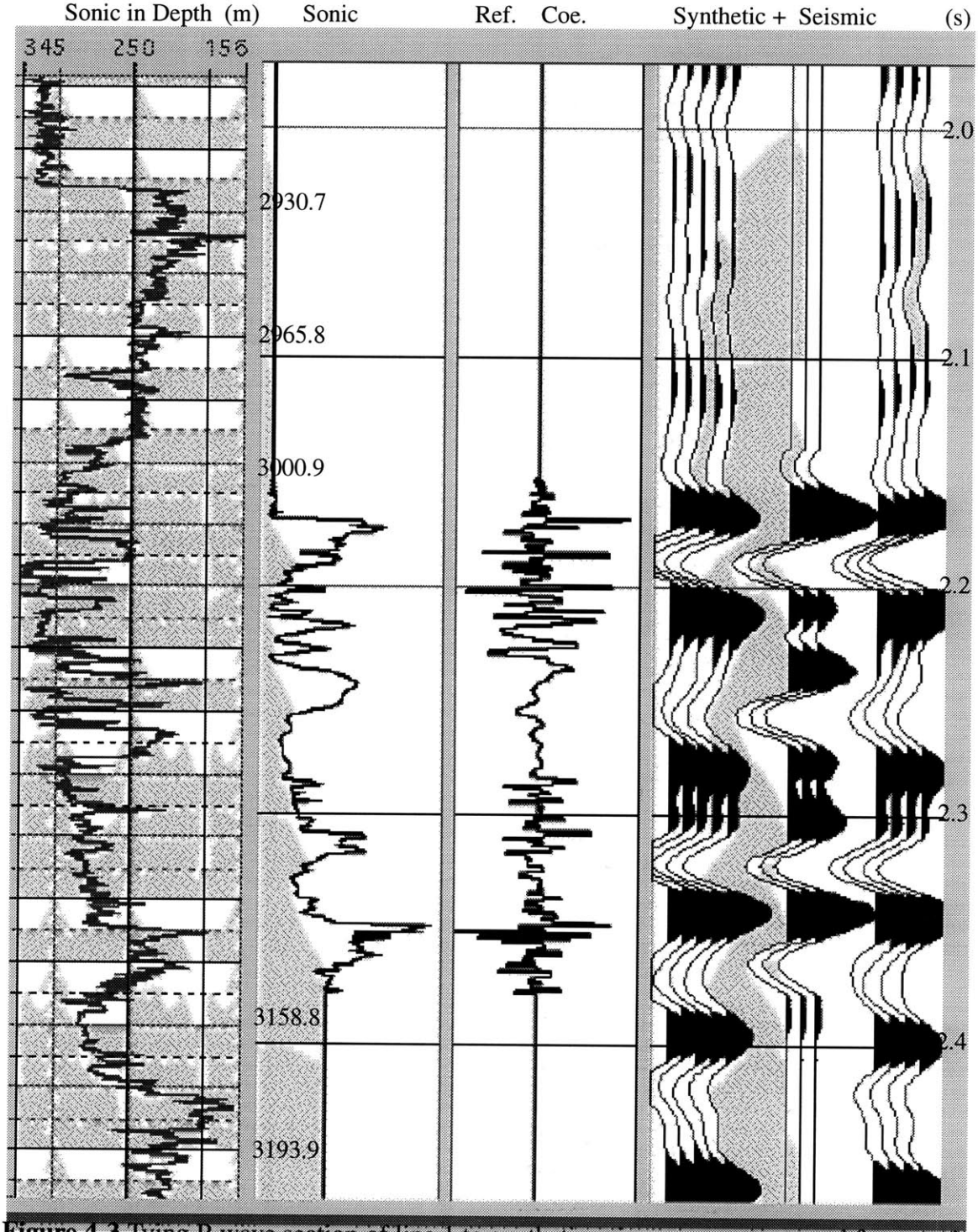

Figure 4-3 Tying P-wave section of line 1 to synthetic seismograms generated from sonic logs of well 13.

Figure 4-4 Prestack CDP gathers (a) CDP 245 to 249 in line 1; (b) CDP 245 to 249 in line 2; (c) CDP 245 to 249 in line 3.

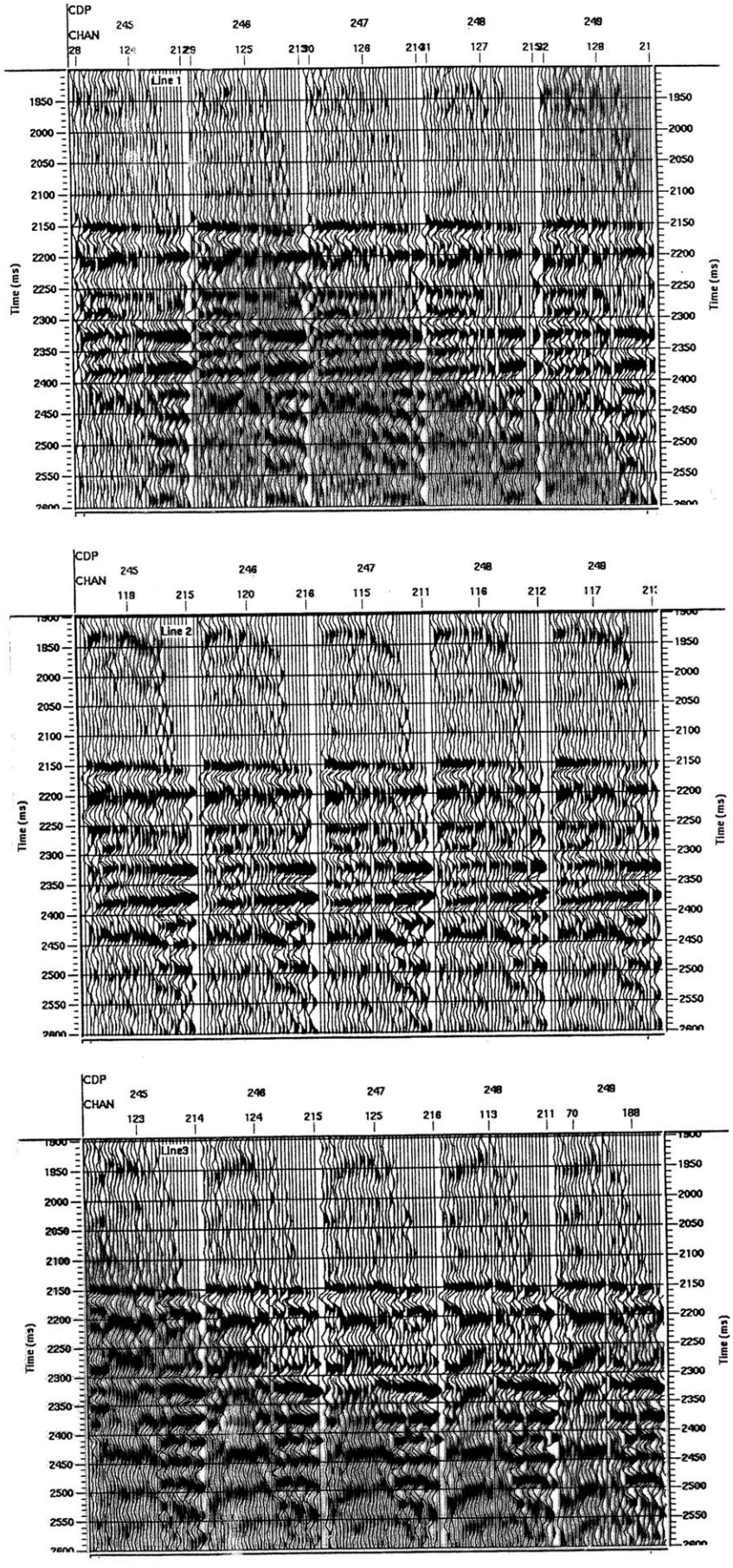
CDP
CHAN
245
246
247
248
249
Line 1
Line 2
Line3
Time (ms)

Figure 4-5a Offset-dependent poststack seismic profiles. (a) near-middle offset, far offset and full offset poststack sections in line 1.

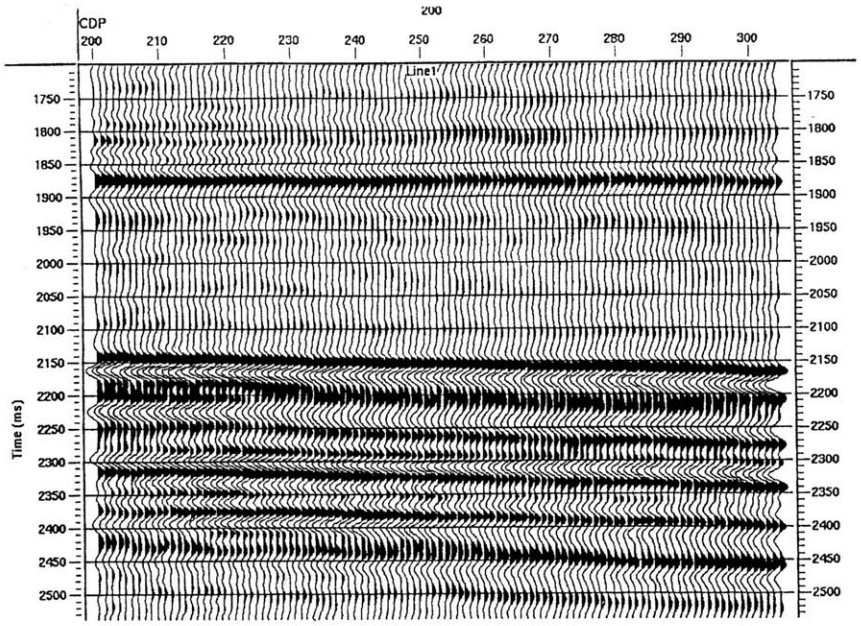
CDP
200
210
220
230
240
250
260
270
280
290
300
Line1
Time (ms)
1750
1800
1850
1900
1950
2000
2050
2100
2150
2200
2250
2300
2350
2400
2450
2500

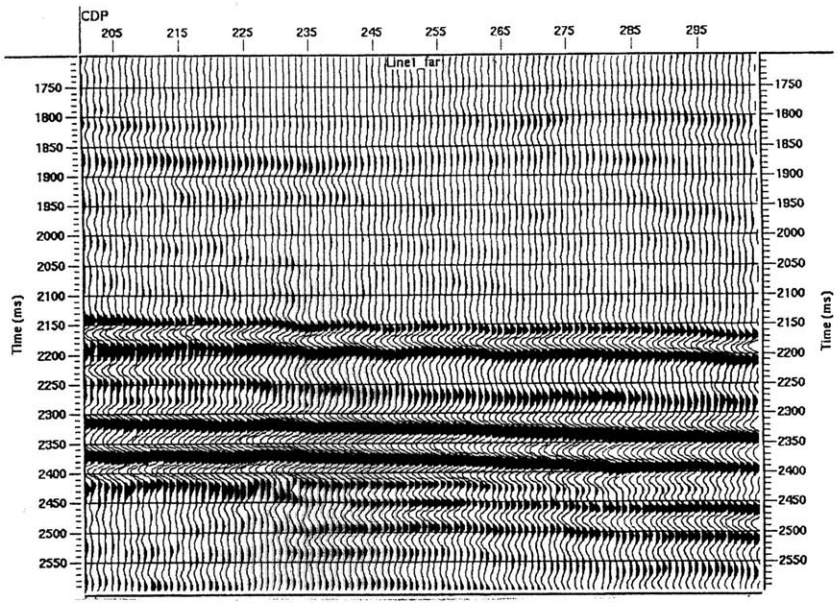
CDP
205
215
225
235
245
255
265
275
285
295
Line1_far
Time (ms)
1750
1800
1850
1900
1950
2000
2050
2100
2150
2200
2250
2300
2350
2400
2450
2500
2550

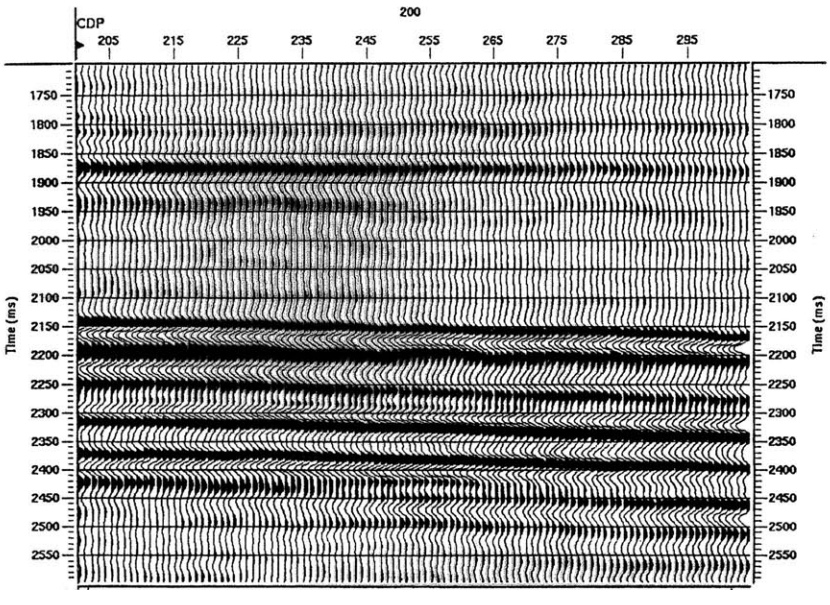
CDP
200
205
215
225
235
245
255
265
275
285
295
Time (ms)
1750
1800
1850
1900
1950
2000
2050
2100
2150
2200
2250
2300
2350
2400
2450
2500
2550

Figure 4-5b Offset-dependent poststack seismic profiles.(b) near-middle offset, far offset and full offset poststack sections in line 2.

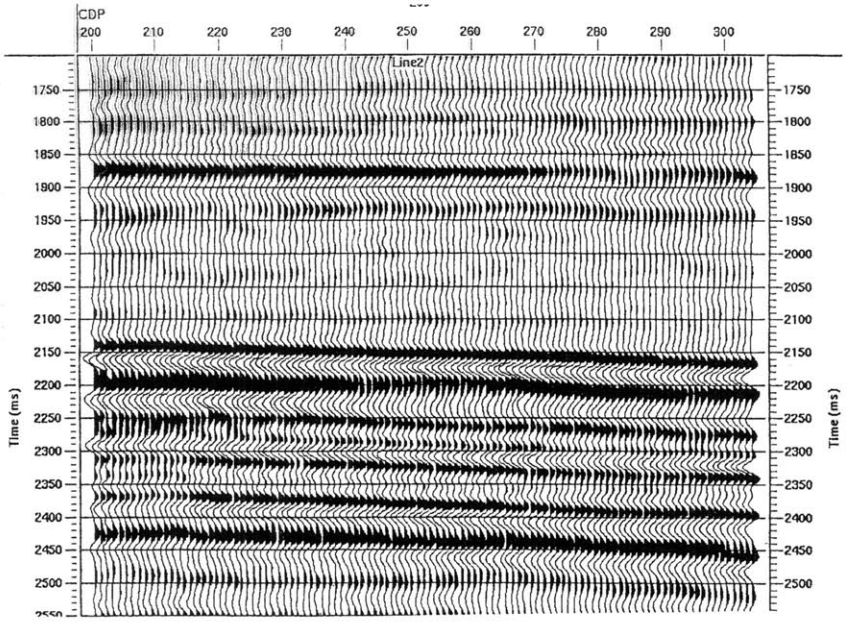
CDP
200 210 220 230 240 250 260 270 280 290 300
Line2
1750 1800 1850 1900 1950 2000 2050 2100 2150 2200 2250 2300 2350 2400 2450 2500
Time (ms)

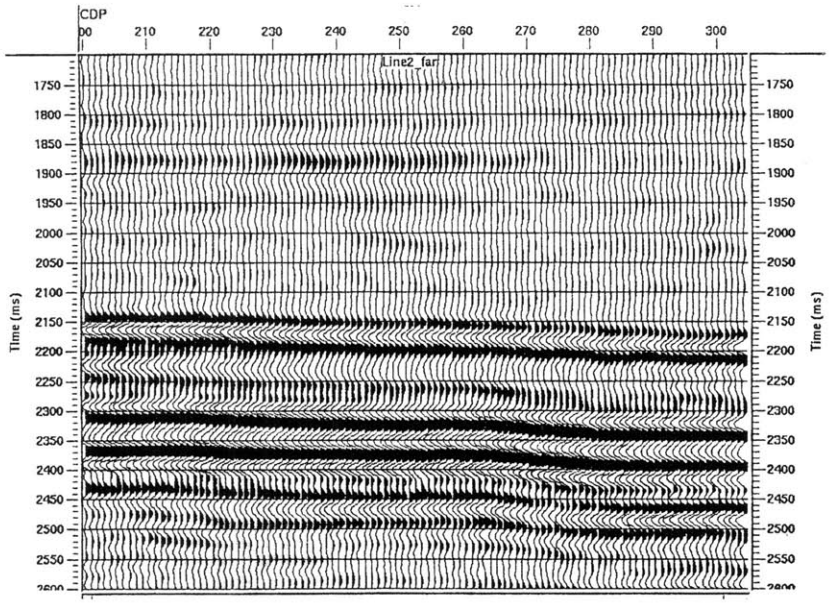
CDP
210 220 230 240 250 260 270 280 290 300
Line2_far
1750 1800 1850 1900 1950 2000 2050 2100 2150 2200 2250 2300 2350 2400 2450 2500 2550
Time (ms)

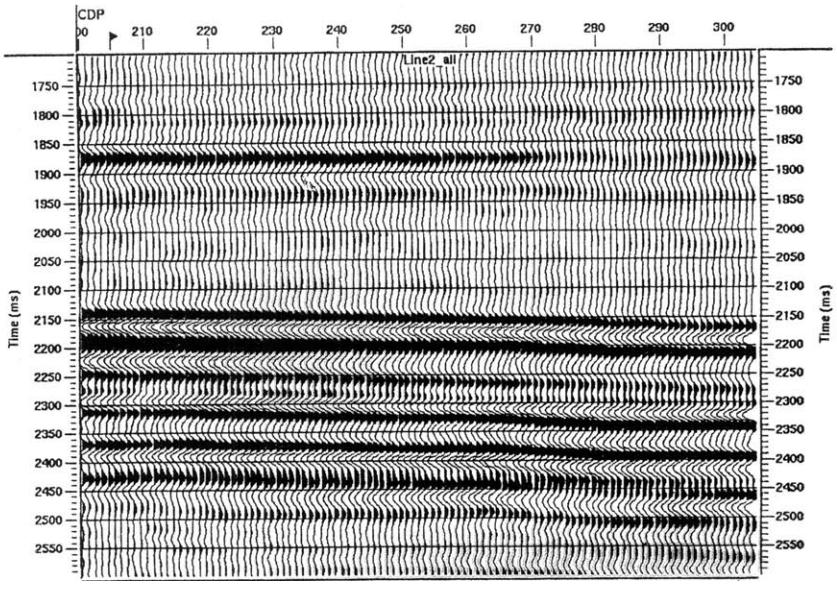
CDP
210 220 230 240 250 260 270 280 290 300
Line2_all
1750 1800 1850 1900 1950 2000 2050 2100 2150 2200 2250 2300 2350 2400 2450 2500 2550
Time (ms)

Figure 4-5c Offset-dependent poststack seismic profiles.(c) near-middle offset, far offset and full offset poststack sections in line 3.

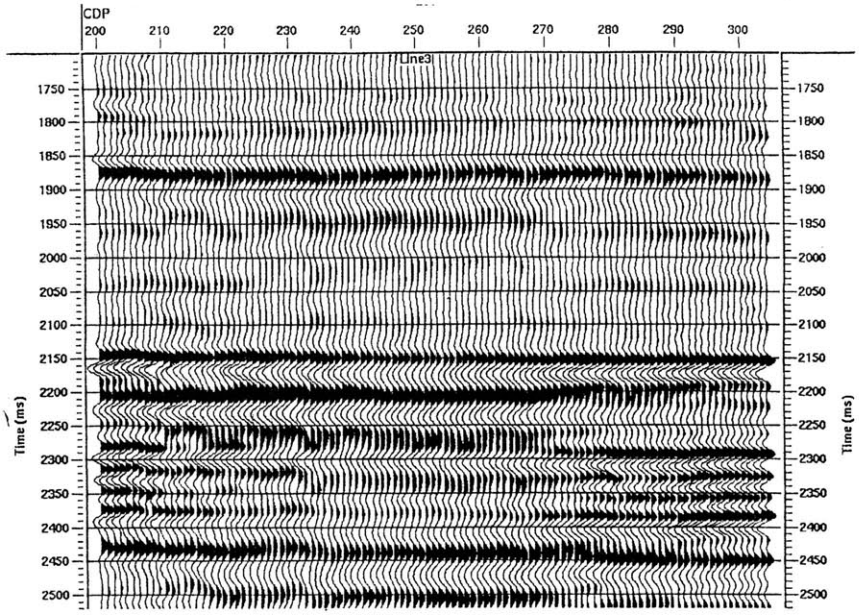
CDP
200 210 220 230 240 250 260 270 280 290 300
Line3
1750 1800 1850 1900 1950 2000 2050 2100 2150 2200 2250 2300 2350 2400 2450 2500
Time (ms)

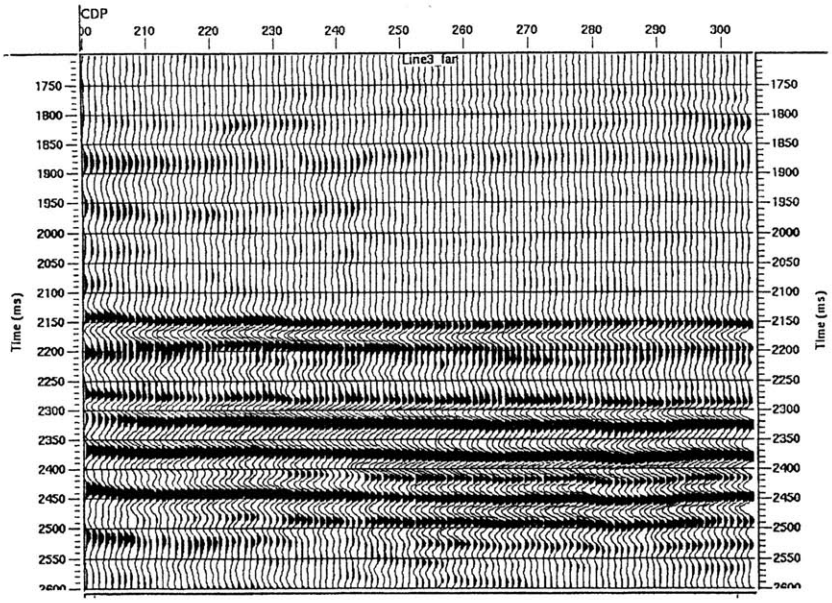
CDP
210 220 230 240 250 260 270 280 290 300
Line3_lan
1750 1800 1850 1900 1950 2000 2050 2100 2150 2200 2250 2300 2350 2400 2450 2500 2550
Time (ms)

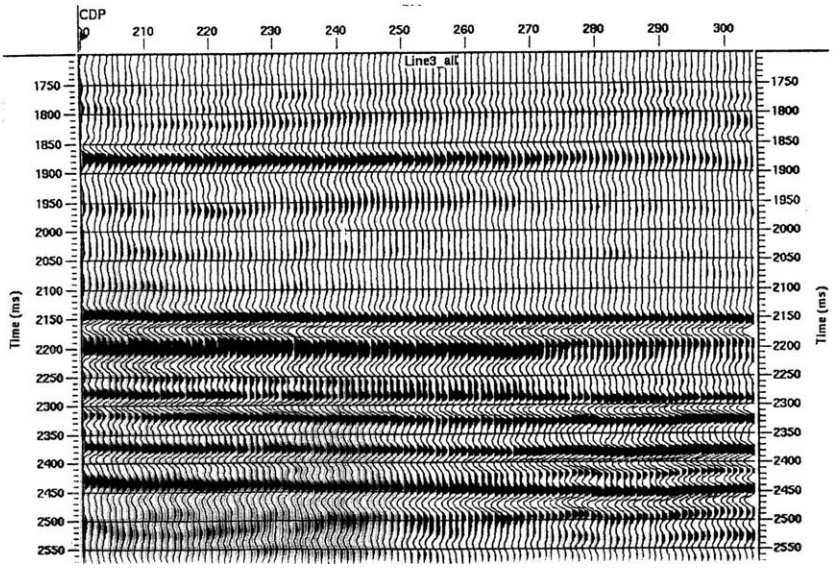
CDP
210 220 230 240 250 260 270 280 290 300
Line3_air
1750 1800 1850 1900 1950 2000 2050 2100 2150 2200 2250 2300 2350 2400 2450 2500 2550
Time (ms)

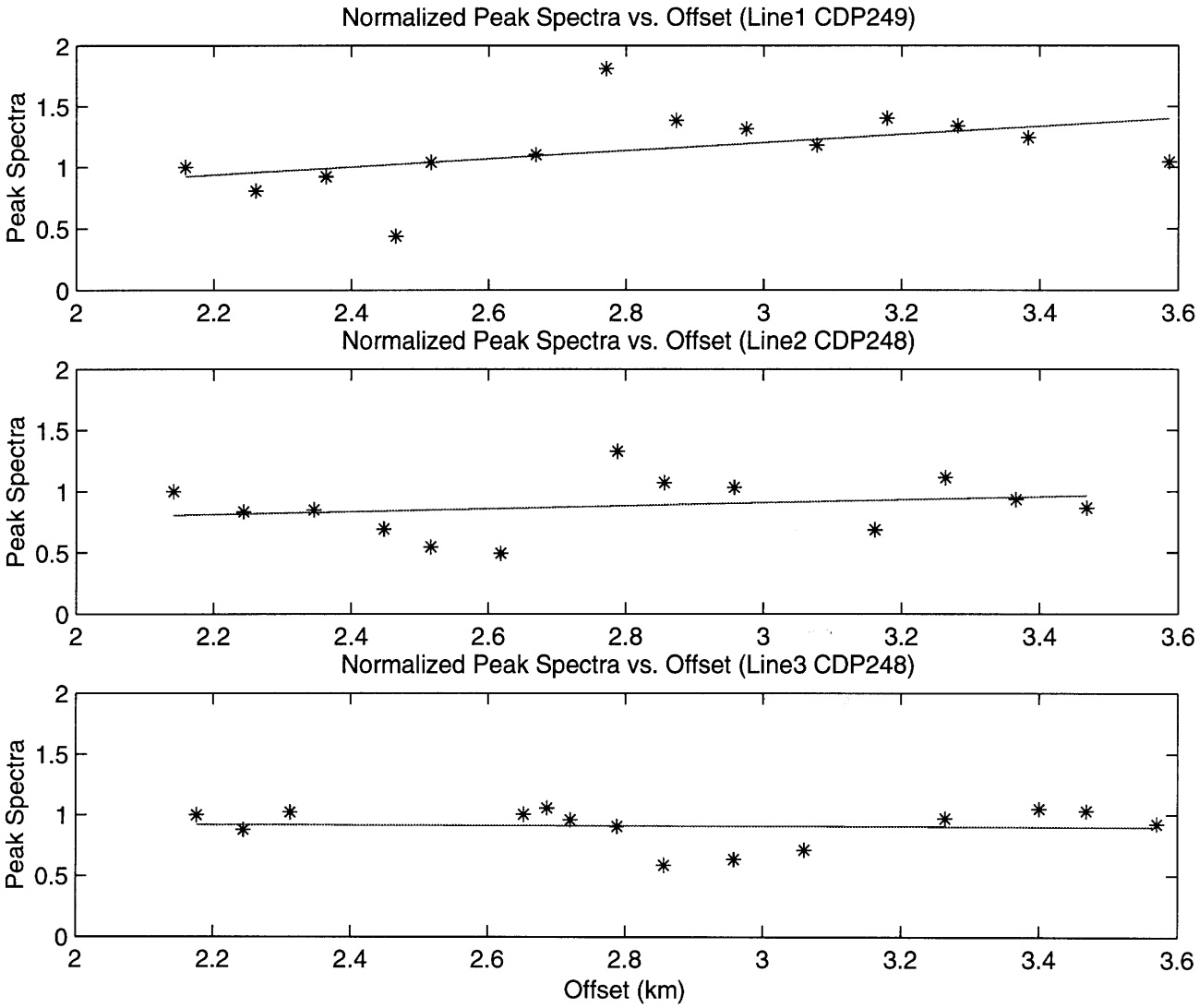

Figure 4-6 (a) Estimated normalized peak spectra versus offset at CDP 249 (line 1), at CDP 248 (line 2) and at CDP 248 (line 3).

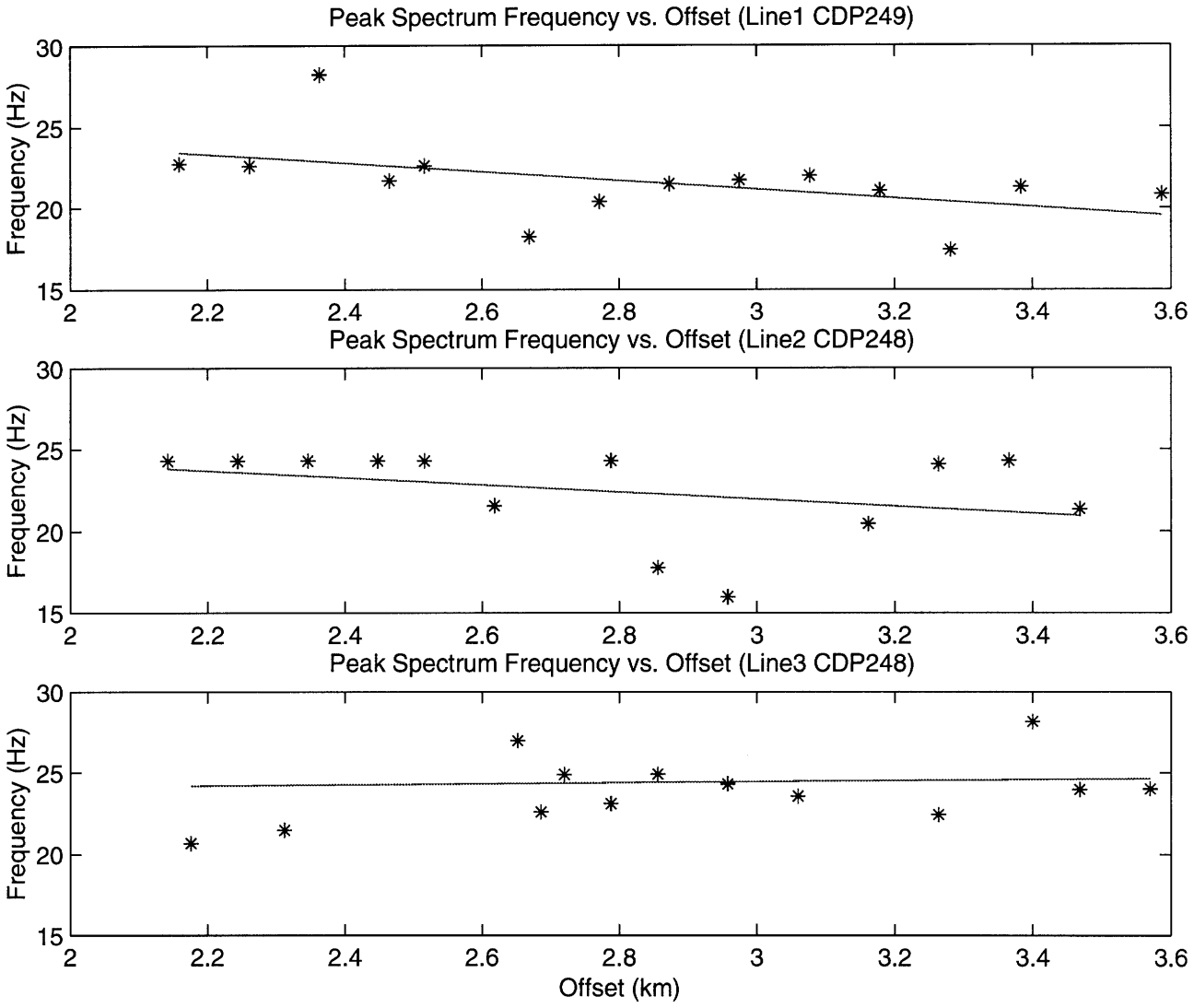

Figure 4-6 (b) Estimated normalized peak spectrum frequency versus offset at CDP 249 (line 1), at CDP 248 (line 2) and at CDP 248 (line 3).

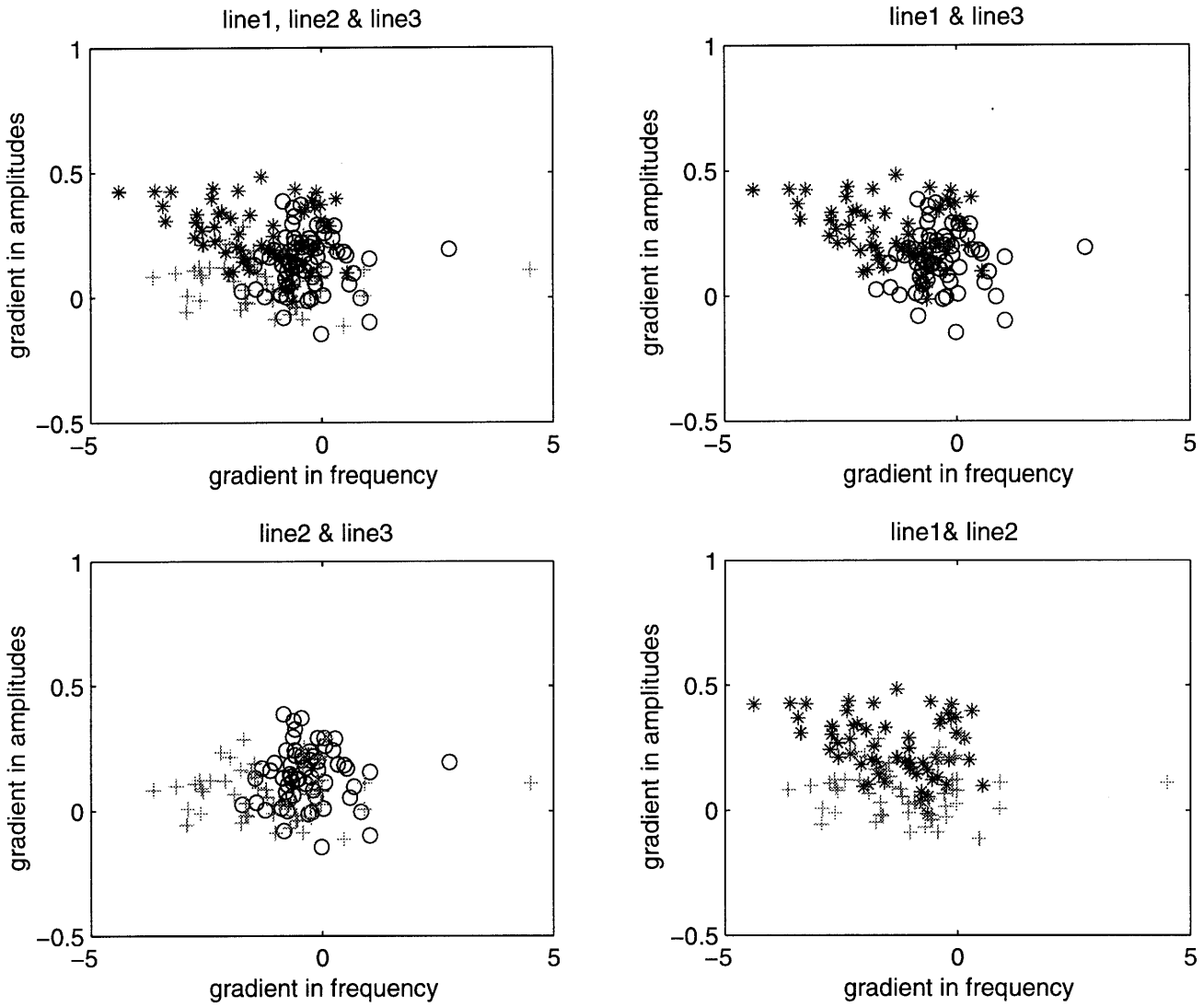

Figure 4-7 Distributions in attribute space. *---CDPs from line 1; +---CDPs from line2; o---CDPs from line 3.

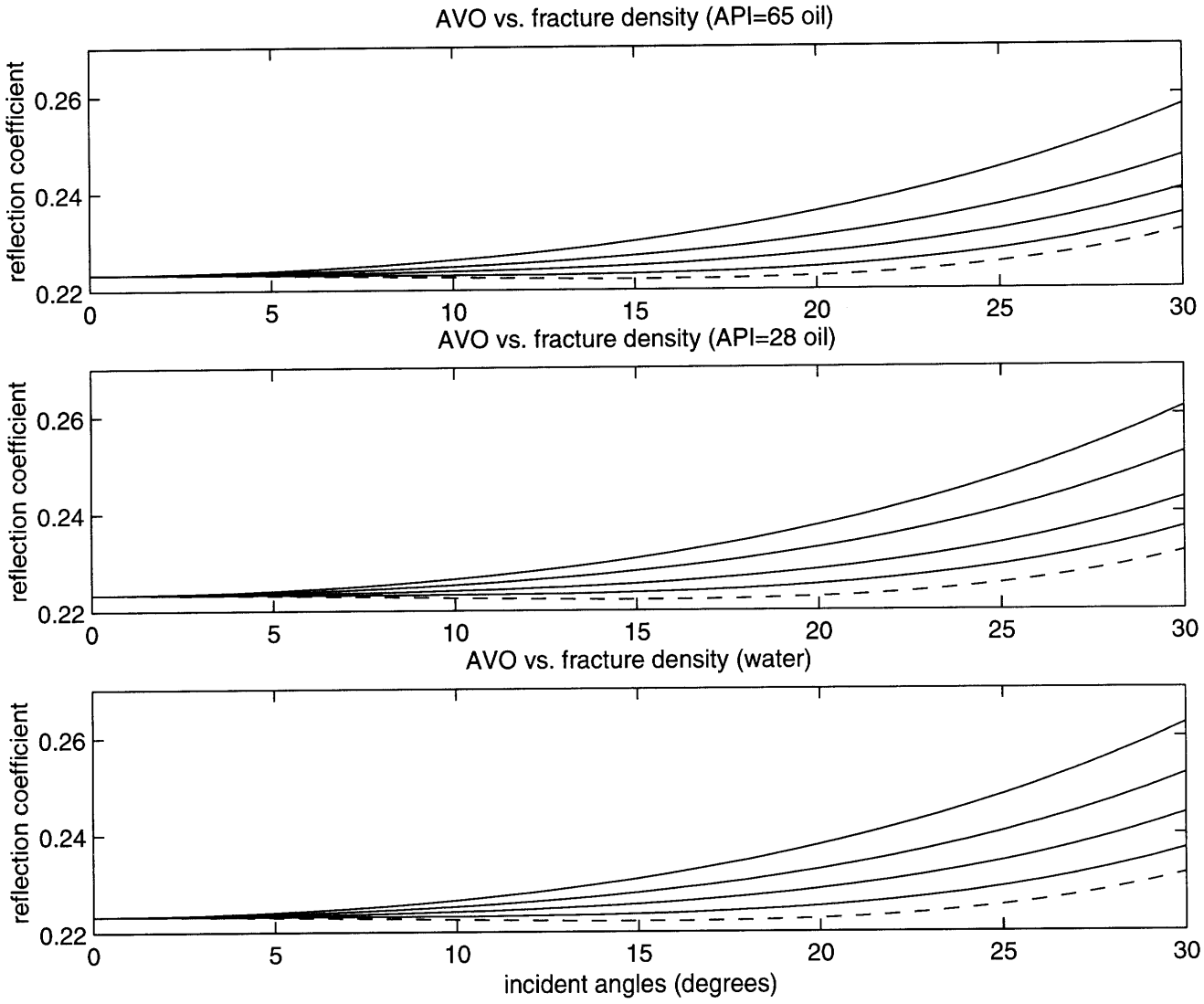

Figure 4-8 Theoretical calculations from parameters listed in Table 1. (a) AVO curves in API 65 oil saturated, fractured reservoirs with fracture density 0%, 5%, 10%, 15% and 20% (from the bottom to the top). (b) AVO curves in API 28 oil saturated, fractured reservoirs with fracture density 0%, 5%, 10%, 15% and 20% (from the bottom to the top). (c) AVO curves in water saturated, fractured reservoirs with fracture density 0%, 5%, 10%, 15% and 20% (from the bottom to the top).

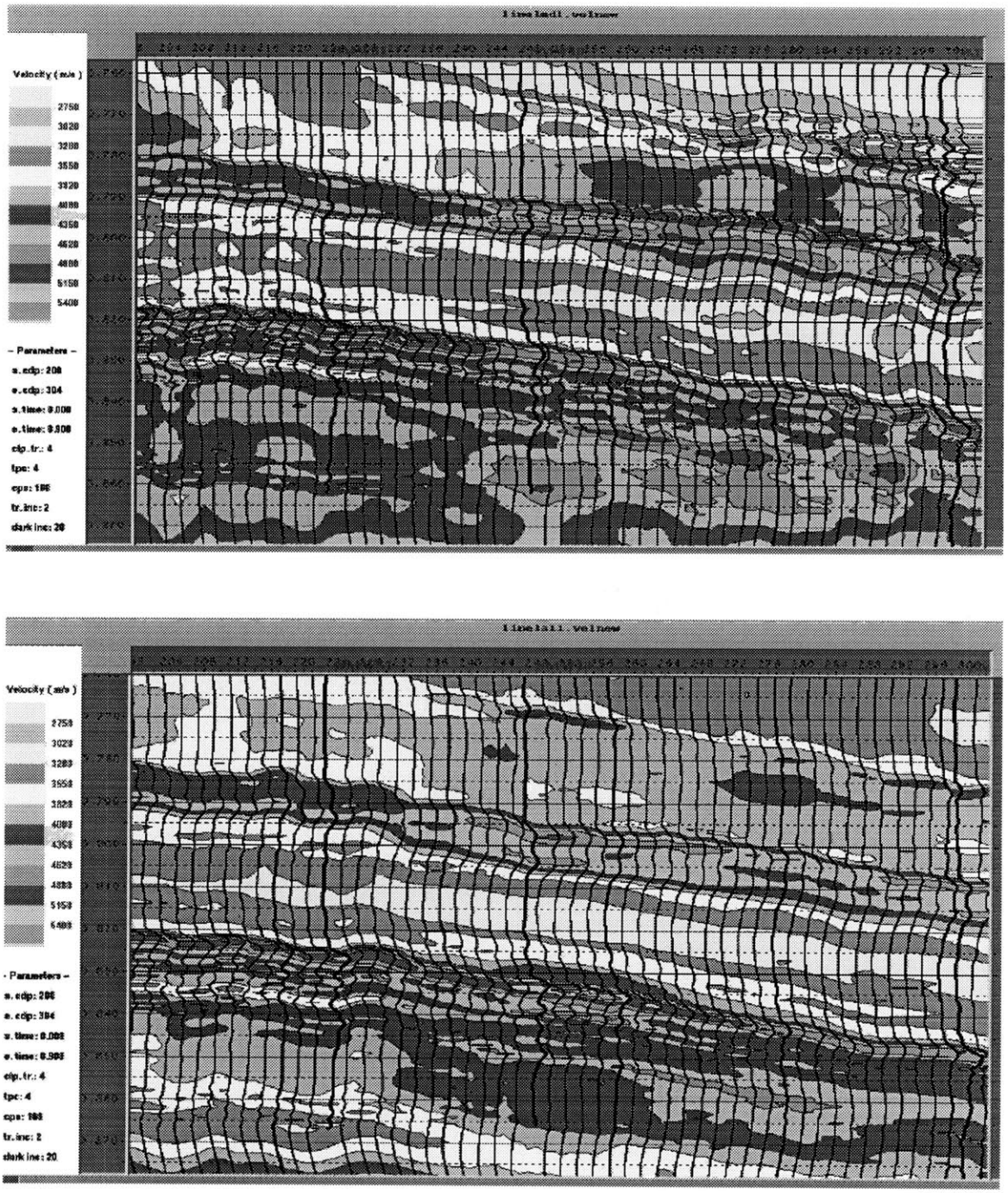

Figure 4-9 (a) Inverted interval P-wave velocities from near-middle poststack data in line 1. (b) Inverted interval P-wave velocities from overall poststack data in line 1.

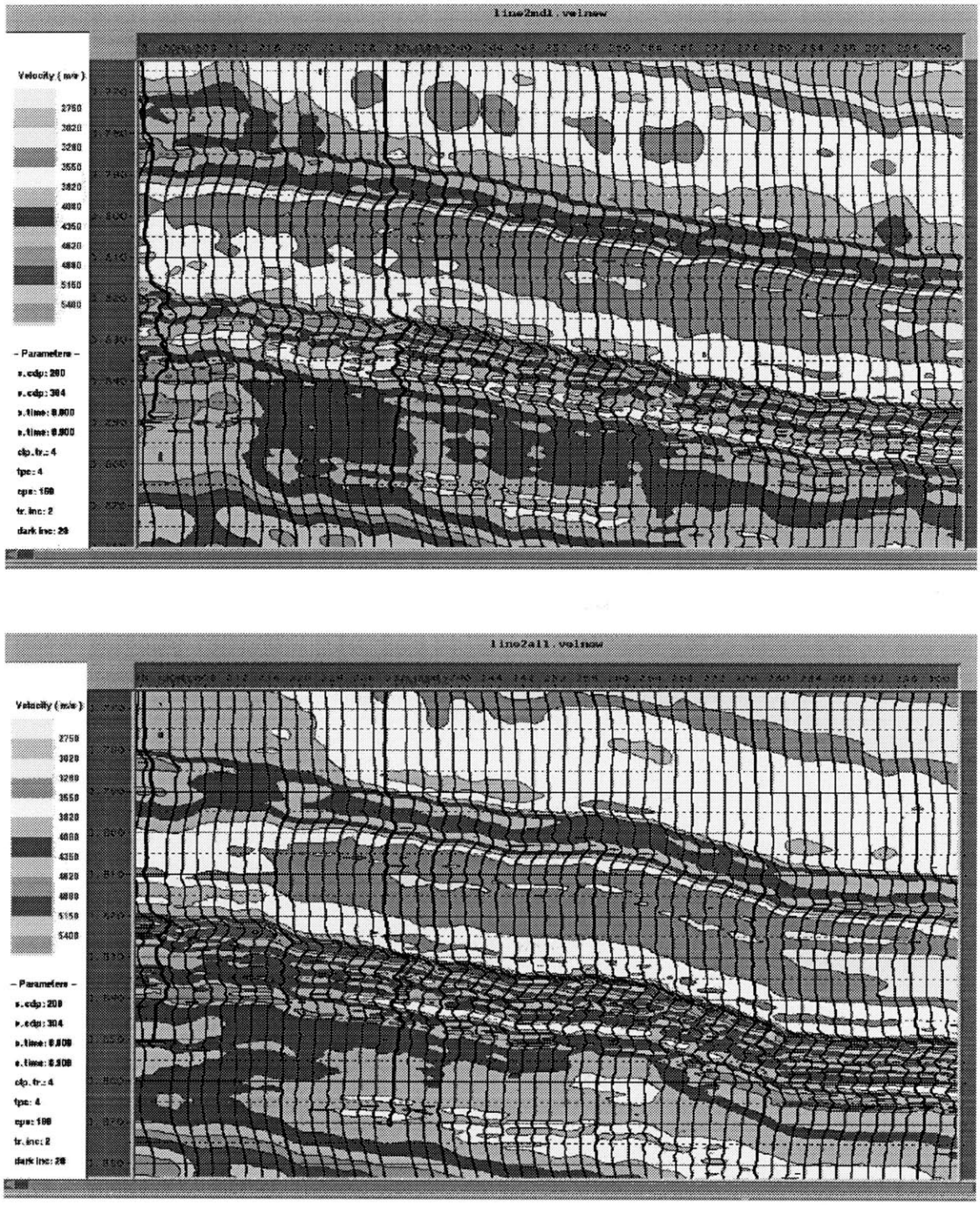

Figure 4-10 (a) Inverted interval P-wave velocities from near-middle poststack data in line 2. (b) Inverted interval P-wave velocities from overall poststack data in line 2.

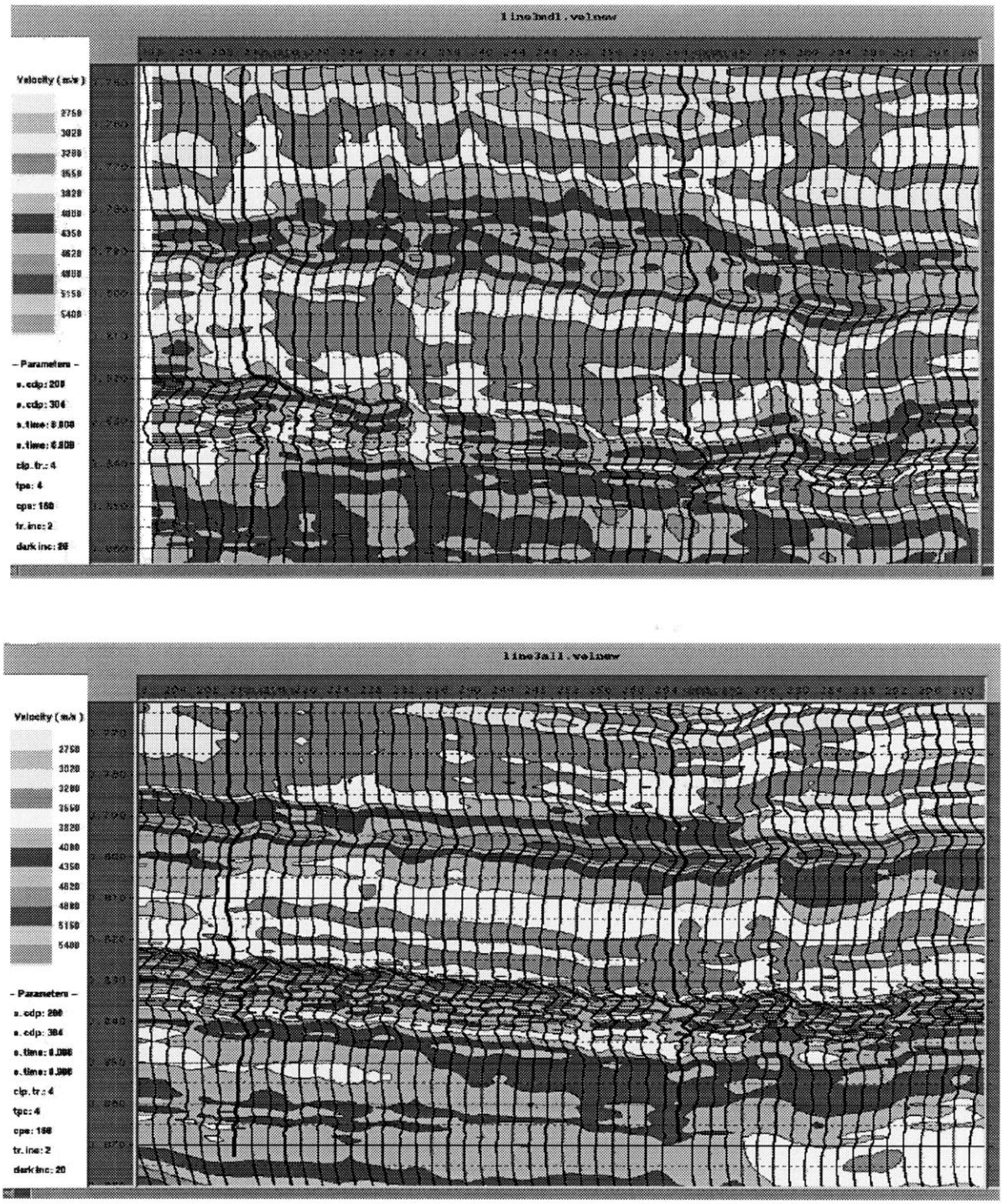

Figure 4-11 (a) Inverted interval P-wave velocities from near-middle poststack data in line 3. (b) Inverted interval P-wave velocities from overall poststack data in line 3.

CHAPTER 5

Large Scale Crustal Deformation in Eastern Syntaxis Of the Tibetan Plateau From a 3-D Analytical Model

5.1 ABSTRACT

A 3-D, large-scale analytical model is used to model continental crustal deformation in the Tibetan plateau. The idealized crust is assumed to consist of two layers, an upper layer with a uniform viscosity and a lower layer with viscosity decreasing exponentially with depth. The motions of the underlying mantle are the fundamental driving forces for crustal flow. The parameters used in modeling are constrained mainly by observations in the India-Asia collision zone of topography. The modeled results reveal that the growth of the Tibetan plateau can be divided into two phases: the mountain building and plateau phases. Crustal flow and thickening show specifical characteristics and have distinct variations in these two phases.

Numerical experiments yield spatial distributions of velocity, strain and rotation rate on the modeled Tibetan plateau. The modeled velocity results indicate that relative right lateral motion occurs between India and south China and East Tibet. Larger velocity gradients are located at the edges of the high plateau. In the central plateau, deformation is characterized by E-W extension. Rapid shortening occurs on the flanks of the plateau and orientations of the principal compressive strain are aligned roughly perpendicular to the regional topographic contours. Much of the relative right-lateral motion is accomplished by clockwise rotation in the region of eastern syntaxis. The maximum rates of rotation about vertical axes occurs in the region of the eastern syntaxis proper.

The topographic gradient plays an important role in the formation and deformation of the Tibetan plateau. The development of surface extension is proportional to the weakness of the lower crust. Calculated results, including topography, surface velocity and strain rate are in broad agreement with geological observations made in this area.

5.2 INTRODUCTION

The largest and highest plateau on earth, the Tibetan plateau, is the result of the collision of the Indian and Asian continental plates (Powell and Consign, 1973; Molnar and Tapponnier, 1975). Convergence between India and Asia has been accommodated in two ways, thrusting of the Indian continental lithosphere under Asia and deformation within Asia. However, there is no agreement on the relative importance of these two mechanisms. Earthquakes within 159 km north of the Himalayan front show clear evidence for underthrusting of India beneath the Himalaya. Paleontological data support the theory that much of the convergence between India and Asia was accommodated by shortening within Asia, and that southern Tibet has moved north by around 2000 km because of the collision (Zhu et al, 1977, Molnar and Chen, 1978; Attache et al, 1984).

The extreme flatness of central Tibet may be due to the presence of a weak lower crust (Bird, 1991, Massed et al, 1994). Several authors have presented models for the deformation of the continents that treat the continental lithosphere as a continuum deforming in response to applied boundary conditions (Tapponnier and Molnar, 1976; Bird and Piper, 1980; England and Mckenzie, 1982; Violate et al., 1982; Zhu and Morgan, 1985; Houseman and England, 1986). For example, Houseman and England (1986) and England and Houseman (1988) use a numerical model of a thin viscous sheet to interpret the tectonic evolution of the Tibetan plateau. Their model assumes a simple indenting boundary condition applied to an initially laterally homogeneous sheet obeying a power law rheology. The deformation causes a broad plateau in front of the indenter. One flaw in their model is that it does not account for the east-west extension in the plateau which is observed in the field. Additionally, the orientation of calculated principal compressive and extensional strains in the southeast of syntaxis (Yunnan) are approximately perpendicular to those inferred from earthquakes in the area.

In this chapter, we present the results of numerical experiments on a 3-D analytical model for large-scale crustal deformation (presented by Royden (1996)). In this model, the crust is treated as laterally homogeneous and is assumed to consist of two layers of Newtonian viscosity whose deformation can be calculated by considering horizontal motions of underlying mantle acting on it. For a given choice of boundary conditions, the calculated deformation is dependent on six parameters. We shall compare the results of calcula-

tions using this model with observations of the Tibetan plateau's topography, present geological and geophysical studies. The comparison provides constrains on the effective parameters. The range of the effective parameters and calculated results help us understand the development of Tibetan plateau and physical mechanisms that control the distribution of deformation in the plateau.

5.3 VISCOUS MODEL

The 3-dimensional, analytical model for large-scale deformation has been described and discussed in detail by Royden (1996) and is only summarized here. In this model, an idealized crust is assumed to consist of two layers of Newtonian viscosity, an upper layer with a uniform viscosity (μ_0) and a lower layer with viscosity decreasing exponentially with depth ($\mu_0 e^{-z/\alpha}$), where z=0 corresponds to the interface between the upper and lower layers. The viscosity of the crust is laterally homogeneous and a function of depth alone. Deformation is controlled by viscosity variations and by the boundary conditions imposed. To the first order, this viscosity profile is generally analogous to that developed by Brace and Kohlstedt (1980) who divide the continental lithosphere into three regions: an upper crust that fails by faulting and obeys Byerlee's law, underlain by a ductile lower crust whose properties are governed by steady state creep of quartz, which in turn is underlain by an upper mantle whose strength is governed by the laboratory-determined properties of dry olivine (Goetze, 1979).

We assume that the "plate-like" mantle lithosphere adjacent to a 'mantle suture' undergoes convergence at a uniform and constant rate driven by mantle motions. The viscosity profile within the crust plays an important role in continental deformation. When no significant low-viscosity zone develops at the base of the crust during crustal thickening, a long linear mountain belt develops above the mantle suture. When a low-viscosity zone is initially absent in the lower crust but develops during convergence and crustal thickening, a steep-sided, flat-topped plateau forms. Accordingly, a plateau goes through two stages in its development, a mountain building phase corresponding to no low-viscosity zone and a plateau phase corresponding to a well developed low-viscosity zone.

Crustal flow can be characterized by two kinds of end member flow models: coupled flow and decoupled flow (Royden, 1996). Viscosity is a dominant factor in controlling the

mode of crustal flow. In the mountain building phase, viscosity is independent of depth and flow occurs in the coupled flow mode. In the plateau phase, as the lower-crustal low-viscosity zone develops, crustal flow may change from coupled to decoupled flow.

If the lower crust beneath the high plateau is very weak, flow occurs in the decoupled flow mode. In this case, channel flow develops within the low-viscosity, lowermost crust. The maximum channel flow rates are commonly many times greater than the rates of mantle motions. Beneath the plateau, lower crustal material is carried away from the mantle suture by the channel flow and upper crustal material is carried toward the suture by laterally transmitted stresses. Channel flow is not a necessary condition for development of a plateau, while it is an indicator of a very weak lower crust. Channel flow disappears very rapidly at the edge of the plateau. In these areas where a low-viscosity zone is absent or does not develop well, such as at the edges of a numerically modeled plateau, crustal flow occurs in the coupled flow mode.

5.4 APPLICATION TO THE TIBETAN PLATEAU

5.4.1 Constraints of parameters

The configuration of the mantle suture and coordinates applying to Tibet modeling are shown in Figure 1. There are only six variables involved in 3-D, analytical solutions: the imposed velocities at the base of the crust, $u_0$and v_0; the initial crustal thickness, h_0+b; the thickness of the upper layer (upper crust), b; the viscosity of the upper layer, μ_0; and the viscosity decay coefficient in the lower layer (lower crust), α. The range of acceptable parameters for convergence rate and initial crustal thickness (u_0, v_0 and h_0+b) vary little, and the other parameters that need to be estimated are μ_0, α and b. The total convergence velocity across the mantle suture is well constrained at about 50 mm/yr. Acceptable values for the three parameters would generate distributions of topography which are comparable with observations. Constraints on acceptable ranges for these parameters are discussed below, and their values are selected based on the comparison with observations in the Tibetan Plateau.

The total convergence rate is assumed to be 50 mm/yr in which the northward motion is 40 mm/yr and southward motion is 10 mm/yr. Based on crustal structure studies, an initial crustal thickness is assumed to vary between 30 km and 35 km. With these assump-

tions, the observed elevation of the Tibetan plateau (4-5 km) can be further used to constrain the choice of upper layer thickness, the uniform viscosity of the upper layer (μ_0) and the viscosity decay coefficient (α) of the lower crust. The crustal thickness has first order control on the height of plateau. If we keep the viscosity of the upper layer (μ_0) and the viscosity decay coefficient (α) of the lower crust constant at $1.0e^{21}$Pa and 1.0 km,\ and change only the upper layer thickness from 45-75 km, the calculated the height of the plateau topography can vary from 3500 to 8000 m and the width of N-S profiles can change from 1000 to 1700 km (Figure 2a). A reasonable upper crustal layer thickness is around 55 km, which makes a comparable topographic height with the Tibetan plateau. The viscosity of the upper layer is a major influence on the shape of the plateau. If we keep the thickness of the upper crustal layer at 55 km and the viscosity decay coefficient (α) of the lower crust constant at 1.0 km, and change only the viscosity of the upper layer (μ_0) from $1.0e^{20}$ to $1.0e^{22}$ Pa, the calculated shape of the plateau can vary from a very low and broad mountain range to an unrealistically tall and narrow plateau, as shown in Figure 2b. The acceptable plateau can be obtained by using μ_0 between $5.0e^{20}$ and $1.0e^{21}$. The viscosity decay coefficient (α) of the lower crust measures the variations of strength of the lower crust with depth and influences mainly the flatness of the plateau. Varying α from 0.01 to 2.0 km, the generated plateau would be characterized by a low, wide, and flat top to a high, narrow and less flat top. Figure 2c shows the cross section of plateaus with different α values. A reasonable plateau can be generated when the viscosity decay coefficient varies between 0.25 and 1.0 km. Based on the comparison between the numerical experiments and the observations of topography in the Tibetan plateau, we prefer the upper layer thickness to be 55 km, the uniform viscosity of the upper layer (μ_0) to be $1.0e^{21}$ Pa, and the viscosity decay coefficient (α) of the lower crust to be 1.0 km.

5.4.2 Implications for plateau development

With the selected parameters, we produce a mountain range a few kilometers in elevation and a few hundred kilometers in N-S cross section. It is assumed that the present plateau formed after 40 m.y. of convergence. Based on the variations of plateau morphology, we divide the development of the plateau into two stages: the mountain building phase and

plateau phase. The evaluation of the plateau in the two stages elucidates physical mechanisms that control the plateau development.

The mountain building phase starts at the beginning of convergence and ends with development of a significant low viscosity zone in the lower crust. Convergence produces a "narrow" triangular mountain range whose width and height are controlled by the upper crustal viscosity, μ_0. (It is necessary for μ_0 to be approximately 10^{21} Pa to produce typical dimensions typical of a mountain system). As convergence proceeds, the mountain range becomes taller and wider, and its final maximum elevation at the end of the mountain building stage (equivalent to the altitude of the plateau) is controlled by the thickness of the upper layer. As mentioned above, in order to produce a flat plateau at about 4-5 km elevation, a low viscosity zone must begin to develop at crustal thicknesses of about 50-60 km (see below). For a total convergence rate of 50 mm/yr and crustal thickness of 55 ±5 km, a low viscosity zone begins to develop at about 3-4 m.y. After 8 m.y. of convergence, the mountain system begins to display distinctly "plateau like" morphology. The N-S cross sections in Figure 3a reveal the development of topography of the mountain range from 2 to 8 m.y. The 3-D morphology of the plateau among the mountain building phase, after 7 m.y. convergence, is shown in Figure 3b.

Crustal flow is strongly coupled to mantle flow during the mountain building phase. At the base of this convergent system, crustal material is carried toward the suture by the motions of the top of the mantle. However, at the surface of the convergent system, gravitational force carries crustal material away from the suture. Although the net thickness of the crust increasing, the N-S and E-W cross sections through the model plateau at 5 m.y. show that, above the mantle suture, crustal thinning occurs in the upper part of the crust and crustal thickening occurs in the lower part of the crust (Figure 4). The maximum rates of crustal shortening at the surface occur at the foot of the mountains because the rate of crustal shortening is proportional to the second spatial derivative of topography in theoretical formula (Royden, 1996).

Once a significant low viscosity zone develops in the lower crust, the plateau phase starts and a flat topped plateau begins to form. As mentioned above, the viscosity decay coefficient of the lower crust (α) controls the strength and flow patterns of the lower crustal layer. Since the weaker lower crust develops in this stage, the morphology of the

plateau, the surface deformation and the crustal flow patterns are mainly effected by the properties of the lower crust. As the lower crust becomes thicker and weaker, the height of the model plateau lowers slightly and the plateau becomes wider due to the horizontal stresses within the upper-mid crust. Figure 5a shows the development of the model plateau from 10 m.y. to 40 m.y. in the south-north direction. The 3-D morphology of the plateau at 40 m.y. is shown in Figure 5b. Profiles from numerical modeling with different viscosity decay coefficients (α) for the lower crust after 40 m.y. of convergence are shown in Figure 6. The N-S topographic observations from the Tibetan plateau are also shown in the same diagram for comparison. Note that, after 40 m.y. of convergence, the plateau extends to the southeast beyond the eastern syntaxis when using the α values 1. and 0.25 km (Figure 7a and 7b). In contrast with other parts of the plateau's edges, the southeast of eastern syntaxis and the southwest of western syntaxis have low topographic gradients.

As mentioned above, crustal flow beneath the plateau is controlled by the strength of the low-viscosity lower crust. If the lower crust is very weak ($\alpha \leq 0.35$ km), crustal deformation beneath the high plateau is decoupled from mantle motions. Material is carried toward the suture within the upper crust and away from the suture within the lowermost crust. Upper crustal thickening beneath the high plateau is in the form of pure shear deformation resulting from laterally transmitted compressive stresses imposed at the plateau's edges. Thinning and extension of the lower crust occur above the mantle suture. The upper crust deformation varies, laterally with thickening at the mantle suture, thinning at the outer edge of the plateau, and thickening at the foot of the plateau. As convergence increases, this phenomenon becomes more and more obvious. On the other hand, if the lower crust is relatively strong, the upper crust thins only along the mantle suture. Although the upper crust becomes thin around the outer edge of the plateau and thick at the foot of the plateau, this variation is not as striking as in the very weak lower crust case. Figures 8 and 9 show the north-south and east-west profiles for the relatively weak lower crust (α=0.25 km) and strong lower crust (α=1.0 km), respectively. The lower crust is well developed beneath the high part of the plateau. Elsewhere, the lower crust does not develop well, and the crustal deformation is similar to that mentioned in the mountain building stage.

5.4.3 Surface velocity field, deformation and rotation

The model surface velocity field (relative to stable South China), superimposed on the calculated topography, shows northward motion in front of the indenter, northeastern motion within the east plateau, southeastward motion in the southeast of the eastern syntaxis (Yunnan) and westward motion along the N-S trending boundary between India and Asia (Figure 10). The velocity field indicates that the motions of the southeastern part of the eastern syntaxis (Yunnan) have a clockwise rotation relative to South China and they pivot about a point near the eastern syntaxis. Relative to South China the velocity field in Figure 10 shows that there is no expulsion of crustal material beyond the eastern margin of the model plateau. Another characteristic of the velocity field is that large velocity gradients distribute around the plateau edges. Velocity directions are roughly perpendicular to the edges of the plateau, whereas those in the high part of the plateau are specifically oriented. The magnitude of the velocity field within the southeast of the eastern syntaxis is smaller than that in the any other part of the plateau.

In order to characterize the deformation fields in the modeled plateau, by using FONDA (Dong, 1993), we compute surface strain and rotation fields derived from the modeled velocity field. To compute strain, we assume a uniform strain field at each location and solve for the velocity gradient tensors. The strain and rotation rates are calculated for each square consisting of four adjacent points. The results are put in the middle of the square.

The principal components of the strain field shown in Figure 11 indicate that different parts of the model plateau exhibit different strain rate distributions and correspond to differing deformation. A uniform strain rate field is located in the high parts of the plateau with E-W extension and N-S compression. Along the flanks of the plateau, the orientations of maximum compressive axes are aligned roughly perpendicular to the regional topographic contours. The rapid crustal shortening rates along the flanks of the plateau are in sharp contrast to the very slow shortening rates on the high plateau. On the surface of the modeled plateau, very large compression distributes in front of the indenter, syntaxis proper and northeast part flanks while small compression occurs in the southeast of the eastern syntaxis (Yunnan). At the outer edges of the plateau, extension is nearly parallel to the regional topographic gradients. Spatial variations in the strain rate field indicate that it

is characterized by E-W extension in the central plateau, E-W compression along the eastern margin of the plateau, and E-W extension in the southeast of the eastern syntaxis (Yunnan).

We have mentioned that the strength of a low-viscosity lower crust controls the subsurface crustal thickening. In order to investigate the effects the strength of the lower crust has on the surface deformation, we calculate the strain rate field for a range of acceptable α, from 0.25 to 2.0 km, for instance. The major deformation characteristics are comparable. However, some variations are still observable. Our results show that the strength of the lower crust also affects the surface deformation and that the weaker the lower crust, the more obvious upper crustal extension is at the edges of the plateau surface. If the lower crust is very strong, for example α=5.0 km, there is no observable extensional deformation at the surface.

Figure 12 shows the rotation field relative to South China. The area surrounding the eastern syntaxis is characterized by clockwise rotation with maximum rate in the region of the eastern syntaxis proper. In the southeastern part of the eastern syntaxis (Yunnan), left-lateral shear is predicted on NW-SE trending zones, with right-lateral shear on NNE-trending zones.

The mantle motion beneath the low-viscosity lowermost crust and topographic gradient at the surface of the plateau are important driving forces of the crustal flow. For a sufficiently weak lower crust, a lower crustal channel forms. Channel flow occurs in approximately the opposite direction of upper mantle flow and increases in magnitude at the edges of the plateau (Figure 13a). Lower crustal material at this depth is carried by channel flow toward the edges of the plateau. Extension and lower crustal thinning are distributed beneath the high plateau, while lower crustal shortening and thickening occur at its edges. With a very weak lower crust, thinning caused by channel flow is very striking. However, if the lower crust is relatively strong ($\alpha > 0.35$ km), the horizontal flow velocity field in the lower crust shows different characteristics and channel flow does not occur (Figure 13b). The difference in the velocity field at the lower parts of the lower crust can be used to explain the difference in crustal thickening.

5.4.4 Varying subduction direction

By asking how our results vary when the southward-directed subduction of the Asian lithosphere beneath the crustal part of the Tibetan plateau is assumed, we can assess the importance of the sense of mantle motions relative to the mantle suture. For this model, we use the same parameters as those in earlier calculations. One of the primary differences between this model's results and one that assumes northward-directed subduction of India is the location of the mantle suture. For the first case, the mantle suture is located beneath the northern part of the plateau. For the second case, the mantle suture is beneath the southern part of the plateau.

The two different cases share the following features: (1) velocity fields show that the eastern syntaxis constitutes a distributed right-lateral shear zone; (2) The region surrounding the eastern syntaxis is characterized by a deformation field that varies from E-W extension in the central plateau to E-W compression along the margin of the plateau; (3) Maximum clockwise rotation occurs near the syntaxes. However, the following differences should also be noted: (1) East component velocities in the second case are more pronounced than those than in the first case. The velocity field in the first case is characterized by north-ward motion in front of the indenter. (2) For the second case, strain rates in the margins of the plateau are much bigger than those in the central plateau, and this difference suggests that the deformation along plateau margins is stronger than that of the high plateau. Deformation is less pronounced in the first case. (3) Rotation rates show more complicated strain partitioning in the second case, while the first case is consistent with left-lateral shear on NW-SE trending zones.

These results can be compared with direct and indirect observations of velocity, strain rates and deformation within the Tibetan plateau.

5.5 OBSERVATIONS AND COMPARISON

According to the obtained velocity field, the crustal movement in the eastern part of the model plateau is characterized by clockwise rotation around the eastern syntaxis. The rotation rates derived from this velocity field predict that the maximum rotation rate is located at the eastern syntaxis proper (Figure 11). The results can be attributed to the northward movement of the Indian plate relative to the South China portion of Eurasia.

This movement created a broad zone of N-trending right-lateral shear. The crustal fragments within this right-lateral shear zone rotate clockwise (Deway, et al., 1989). Such rotational movement is also indicated by tectonic evidence. In the eastern Tibetan plateau there are numerous, active strike-slip faults surrounding the eastern syntaxis and which are convex to the northeast. To mention a few dominant faults, the Jali-Sagaing fault and Red River fault are right-lateral (Allen et al., 1984, Wang, 1994) and the Litang and the Xianshuihe/Xiaojiang faults are left-lateral (Allen et al., 1991). The shear pattern and the arcuate geometry of these faults indicate that the crustal movement along them must be characterized by clockwise rotation around the eastern syntaxis. The fact that the middle part of the Red River fault is prominently bent to the south also suggests that the crust has moved to the southwest.

Our numerical results are consistent with other studies on the earthquake focal mechanisms in the region of the eastern Himalayan syntaxis (Holt, et al., 1991, Holt and Haines, 1993). These studies show that the entire area, extending from 20^{o}N-30^{o}N, within deforming Asia (Yunnan, western Sichuan, and eastern Tibet), constitutes a distributed dextral shear zone with clockwise rotation. As shown in Figure 10, there is no component of eastward motion of crustal material beyond the eastern margin of the model plateau. The velocity results from GPS measurements in the Longmen Shan area also indicate that there is no significant eastward motion relative to Chendu in the east margin of the Tibetan plateau (King et al., 1996). The geological evidence has revealed that most of the eastern margin of Tibet, south of Qinling mountain, is not significantly shortened by thrusting (Burchfiel et al., 1996)

As shown in Figure 12, the strain rate field derived from numerical results indicates that the maximum compressive strain rate occurs along the flanks of the plateau, roughly parallel to topographic gradients. On the other hand, extension is generated along the outer edges of the plateau, approximately perpendicular to topographic gradients. Additionally, the maximum compressive strain rates are distributed in front of the indenter (Indian plate) and in the northeast margins of the plateau, where consistent geological studies show that intensive crustal shortening has dominated the Cenozoic evolution of the Himalaya thrust belt and Qilian Shan (Tapponnier et al., 1990). Along the northern margin of the Hima-

laya, the evidence supports the existence of E-treading low-angle normal faults (Burchfiel et al., 1992).

5.6 DISCUSSION AND CONCLUSION

The topography, velocity and strain rate fields calculated from a 3-dimensional analytical model for large-scale crustal deformation are consistent with results from geological studies. This correlation supports our interpretation that crustal deformation results from crust flows existing within the upper crustal and lower crust. These flows are controlled by viscosity within the upper crust and lower crust. To the first order, the numerical results reveal the general process of continental deformation in the Tibetan plateau and also display the relationship between surface deformation and lower crustal viscosity. The surface velocity field shows that velocities increase at the edge of the high part of the plateau, and it implies that crust in the region of the eastern syntaxis has undergone clockwise rotation relative to South China and has formed a right-lateral distributed shear zone. North trending velocity gradients occurring in the southeastern part of the eastern syntaxis are attributed to gravitational effects. Rapid crustal thickening occurs on the flanks of the plateau and orientations of the principal maximum compressive strain rates are aligned roughly perpendicularly to regional topographic contours. With the development of the plateau, the high plateau itself occupies a local minimum strain rate field. Rotation rates show that the maximum rotation rates are located at the syntaxis proper.

However, some direct comparisons between the numerical results and observations are difficult. For example, earthquake data are sensitive to local deformation and emphasize short term slip rates while the 3-D model velocity field demonstrates an average of long term effects. It is well known that continental deformation is dominated by the deformation of the upper 20 km or so of crust in which most intercontinental earthquakes occur. In addition, with strain partitioning, strike-slip faulting may develop. These strike slip faults and their configuration could become more important in the late stages of plateau evolution. The effects of faulting are not considered in the 3-D, analytical model. Additionally, results of the calculations are dependent on the assumptions of lateral homogeneity of crustal viscosity. Vilotte et al. (1982) and England and Houseman (1988) suggest that the

presence of the lateral heterogeneities may lead to enhancement of strike-slip deformation around the northern edges of the Tibetan plateau.

Crustal thickening in the Tibetan plateau is a direct consequence of the collision between India and Asia, but there is considerable debate as to whether a large fraction of the indentation has been accommodated by eastward motion of the lithospheric blocks of southeastern Asia and southern China. The numerical experiments tested by Houseman and England (1993) show that during collision the eastern boundary is smoothly displaced to the east at a rate about 1/4 of the indentation rate, with only minor variation due to geometry or rheology. The significant east-west asymmetry of the Tibetan plateau may have other causes. It could be induced by the obliquity of the indenter or by a large scale lithospheric strength heterogeneity, such as an anomalously strong block of the lithosphere in the location of the Tarim basin.

REFERENCES

Achache, J., Courtillot, V. and Zhou, Y. X., Paleogeographic and tectonic evolution of southern Tibet since middle Cretaceous time: New paleomagnetic data and synthesis, J. Geophys. Res., 89, 10311-10339, 1984.

Allen, C. R., Gillespie, A. R., Han, Y., Sieh, K. E., Zhang, B., and Zhu, C., Red River and associated Yunnan province, China: Quaternary geology, slip rates, and seismic hazard, Geol. Soc. Am. Bull., 95, 686-700, 1984.

Allen, C. R., Lio Zhuoli, Qian Hong, Wen Xueze, Zhou, Huawei and Huang Weishi, Field study of a highly active fault zone: the Xianshuihe fault of southwestern China, Geol. Soc. Am. Bull., 1989.

Bird, P., Lateral extension of lower crust from under high topography in the isostaic limit, J. Geophys. Res., 96, 10275-10286, 1991.

Bird, P., and Piper, K., Plane stress finite element of tectonic flow in southern California, Phys. Earth. Planet. Inter., 21, 158-175, 1980.

Brace, W. F., and Kohlstedt, D. L., Limits on lithospheric stress imposed by laboratory experiments, J. Geophys. Res., 85, 6248-6253, 1980.

Burchfiel, B. C., Chen, Z., Hodges, K. V., Liu, Y., Royden, L. H., Deng, C., and Xu, J., Extension contemporaneous with and parallel to shortening in the Himalaya, Geological Society of America Special Paper, 269, 41, 1992.

Burchfiel, B. C., Chen, Z., Liu, Y., Royden, L. H., Tectonics of the Longmen Shan and adjacent regions, International Geological Review, 37, 661-735, 1996.

Dewey, J., Shackleton, R. M., Chang, C., and Sun, Y., The Tectonics Evolution of the Tibetan plateau, in Chang, C., Shackleton, R. M., Dewey, J., and Yin, J., (eds), The geological evolution of Tibet, Philospherical Transactions of the Royal Society of London, Series A, 327, 397-413, 1988.

Dong, D. N., The horizontal velocity field in southern California from a combination of terrestrial and space-geodetic data, Ph.D. thesis, Mass. Inst. of Technol., Cambridge, 157 pp. 1993.

Englanf, P., and Mckenzie, D. P., A thin viscous sheet model for continental deformation, *Geophys. J. R. Astron. Soc.*, 70, 295-321, 1982.

England, P., and Houseman, G., The mechanics of the Tibetan plateau, Philos. Trans. R. Soc. London Ser. A, 326, 301-320, 1988.

Goetze, C., and Evans, B., Stress and temperature in the bending lithosphere as constrained by experiments rock mechanics, Geophys. J. R. astr. Soc., 59, 463-478, 1979.

Holt, W. E., and Ni, J. F., Wallace, T. C., and Haines, A. J., The active tectonics of the eastern Himalayan suntaxis and surrounding regions, J. Geophys. Res., 96, 14595-14632, 1991.

Holt, W. E., and Haines, A. J., Velocity fields in deforming Asia from the inversion of earthquake-related strain, Tectonics, 12, 1-20, 1993.

Houseman, G., and England, P., Finite strain calculations of continental deformation, 1, methods and general results for convergent zones, J. Geophys. Res., 91, 3651-3663, 1986.

King, R. W., Shen, F., Burchfiel, B. C., Chen, Z., Li, Y., Liu, Y., Royden, L. H., Wang, E., Zhang, X., and Zhao, J., 1996, Geodetic measurement of crustal motion in southwest China, Geology,

Masek L. G., Isacks, B. L., Fielding, E. J., and Browaeys, J., Rift flank uplift in Tibet: evidence for a viscous lower crust, Tectonics, 13, 659-667, 1994.

Molnar, P., and Chen, W. P., Evidence for large Cenozoic crustal shortening of Asia, Nature, 273, 218-220, 1978.

Molnar, P., and Tapponnier, P., Cenozoic tectonics of Asia: effects of a continental collision, Science, 189, 419-426.

Powell, C. M., and Conaghan, P., Plate tectonics and the Himalayas, Earth Planet. Sci. Lett., 20, 1-12, 1973.

Royden, L., Coupling and decoupling of crust and mantle in convengent orogens: Implications for strain partitioning in the crust, J. Geophys. Res.,

Tapponnier, P., and Molnar, P., Slip-line field theory and large scale continental tectonics, Nature, 264, 319-324, 1976.

Tapponnier, P., Meyer, B., Avouac, J.P., Peltzer, G., Gaudemer, Y., Guo, S., Xiang, H.G., Yhin, K., Chen, Z., and Dai, H., Active thrusting and folding in the Qinlian Shan, and Decouple between upper crust and mantle in northeastern Tibet, Earth Planet. Sci. and Lett., 97, 382-403, 1990.

Vilotte, J.P., Daignieres, M., and Madariaga, R., Numerical modeling of intraplate deformation: Simple mechanical models of continental collision, J. Geophys. Res., 87, 10709-10728, 1982.

Wang, E., Late cenozoic Xianshuihe/Xiaojiang and red river fault systems of southeastern Sichuan and central Yunnan, China, Ph.D thesis, 256 pp., Mass. Inst. of Technol., Canbridge, 1994.

Zhao, W. L., and Mrgan, W. J., Uplift of Tibet Plateau, Tectonics, 4, 359-369, 1985.

Zhu, X., Liu, C., Ye, S., and Liu, J., Remanence of red beds from Linzhou, Xizang and northward movement of the Indian plate, Sci, Geol.Sin., 1, 44-51, 1977.

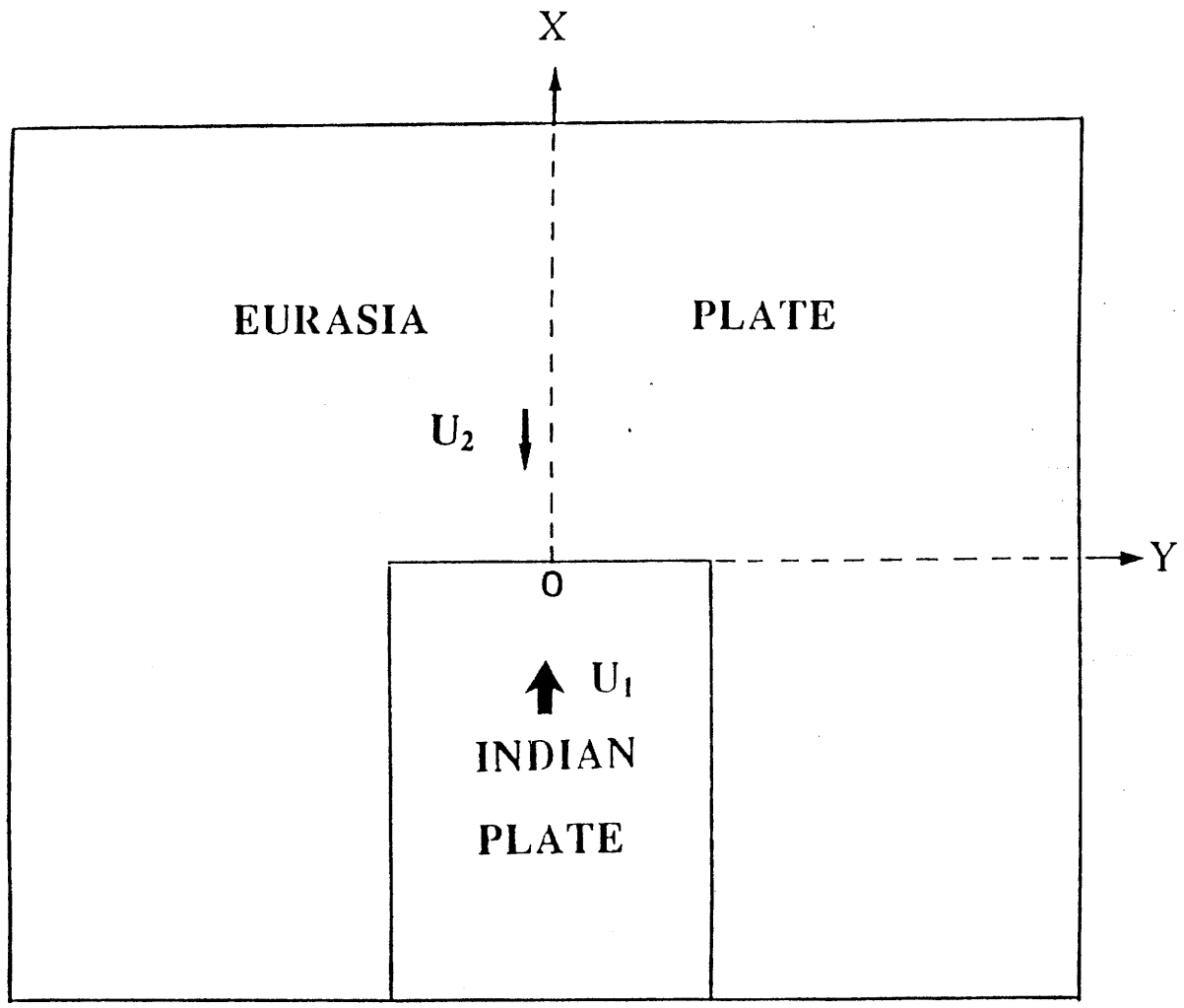

Figure 5-1 Configuration, coordinates, and base boundary conditions for the numerical calculations.

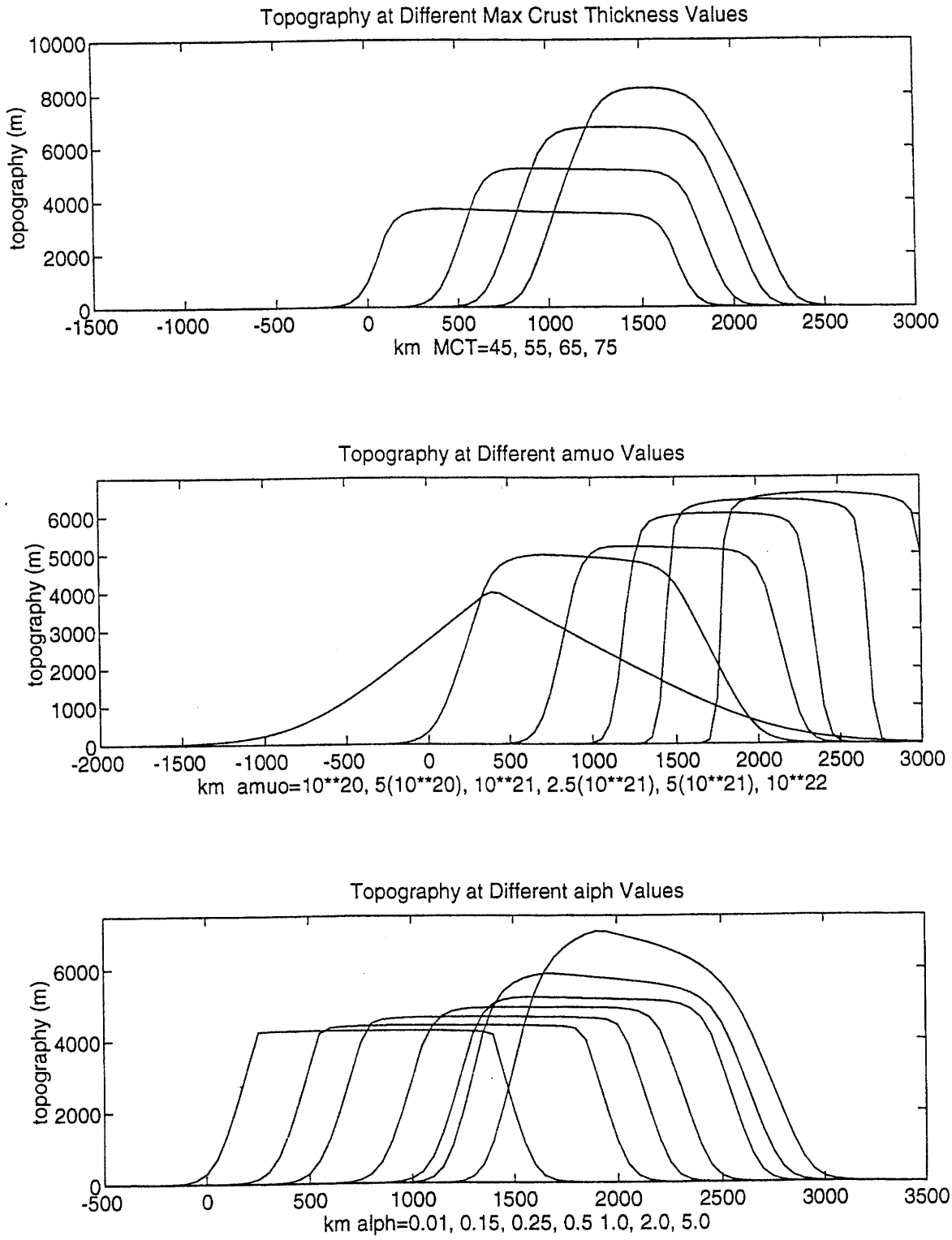

Figure 5-2 N-S topography cross sections with different parameters: (a) Upper crustal thickness with 45, 55, 65 and 75 km; (b) Upper crustal viscosity with $1.e^{20}$, $5.0e^{20}$, $1.0e^{20}$, $5e^{21}$ and $1.e^{22}$ Pa; (c) Viscosity decay coefficients of the lower crust with 0.01, 0.15, 0.25, 1.0, 2.0 and 5.0 km.

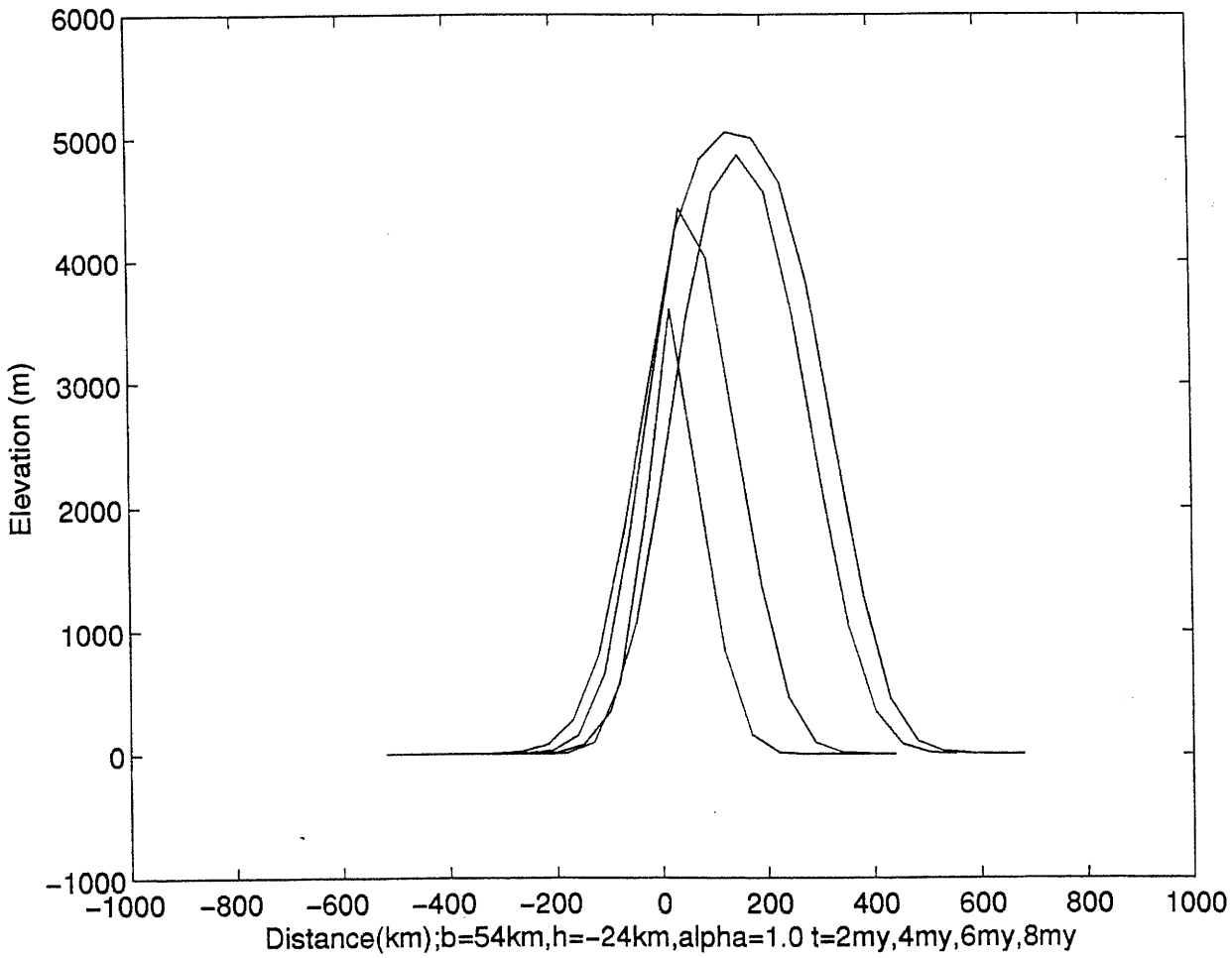

Figure 5-3a S-N trending profiles illustrate the developement of the plateau at the 'mountain building' stage, from 0 to 8m.y. The curves represent the convergence at 2 m.y., 4m.y., 6m.y. and 8m.y.

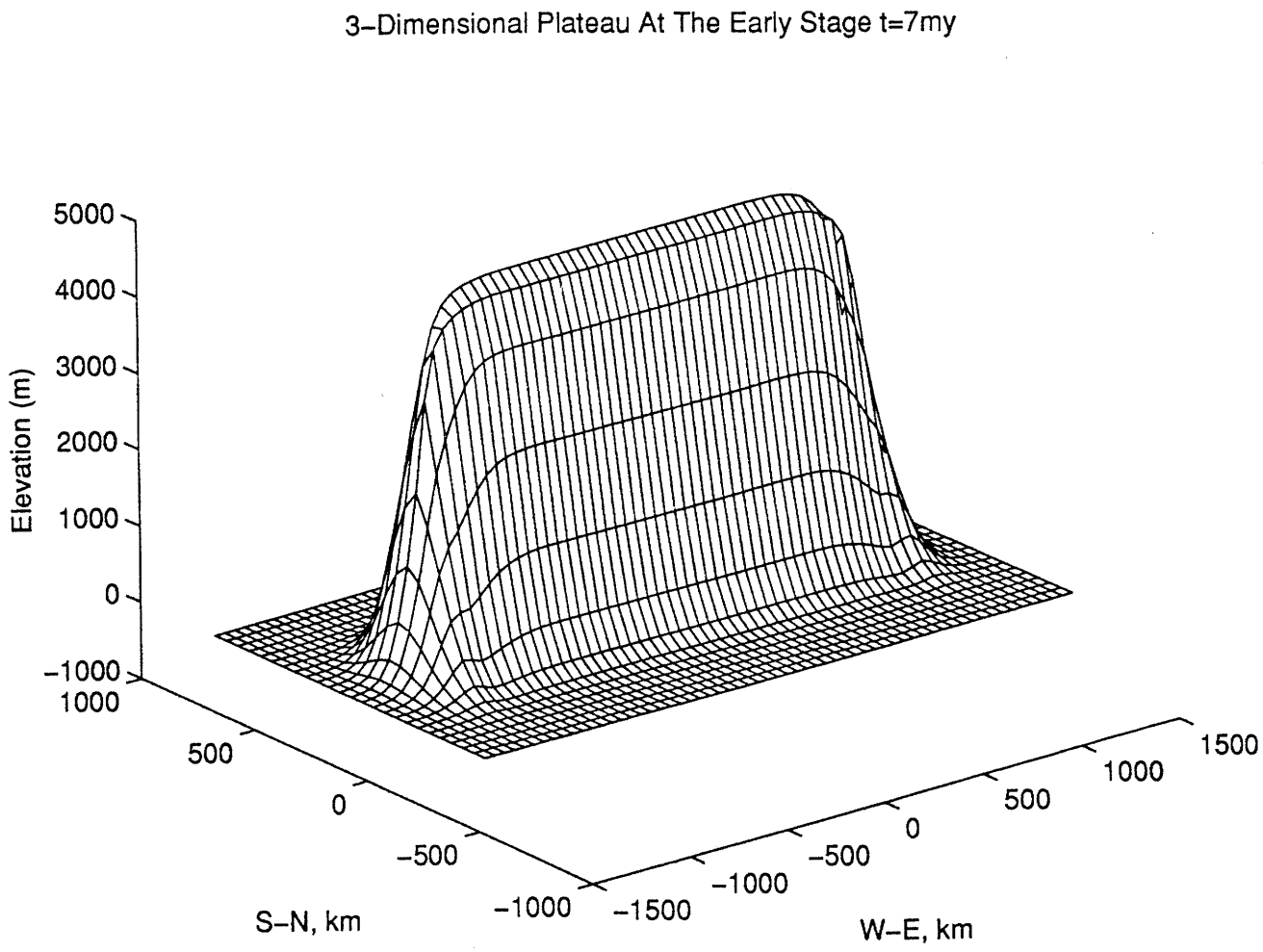

Figure 5-3b 3-D topography for the plateau at 'mountain building' stage represents convergence at 7 m.y.

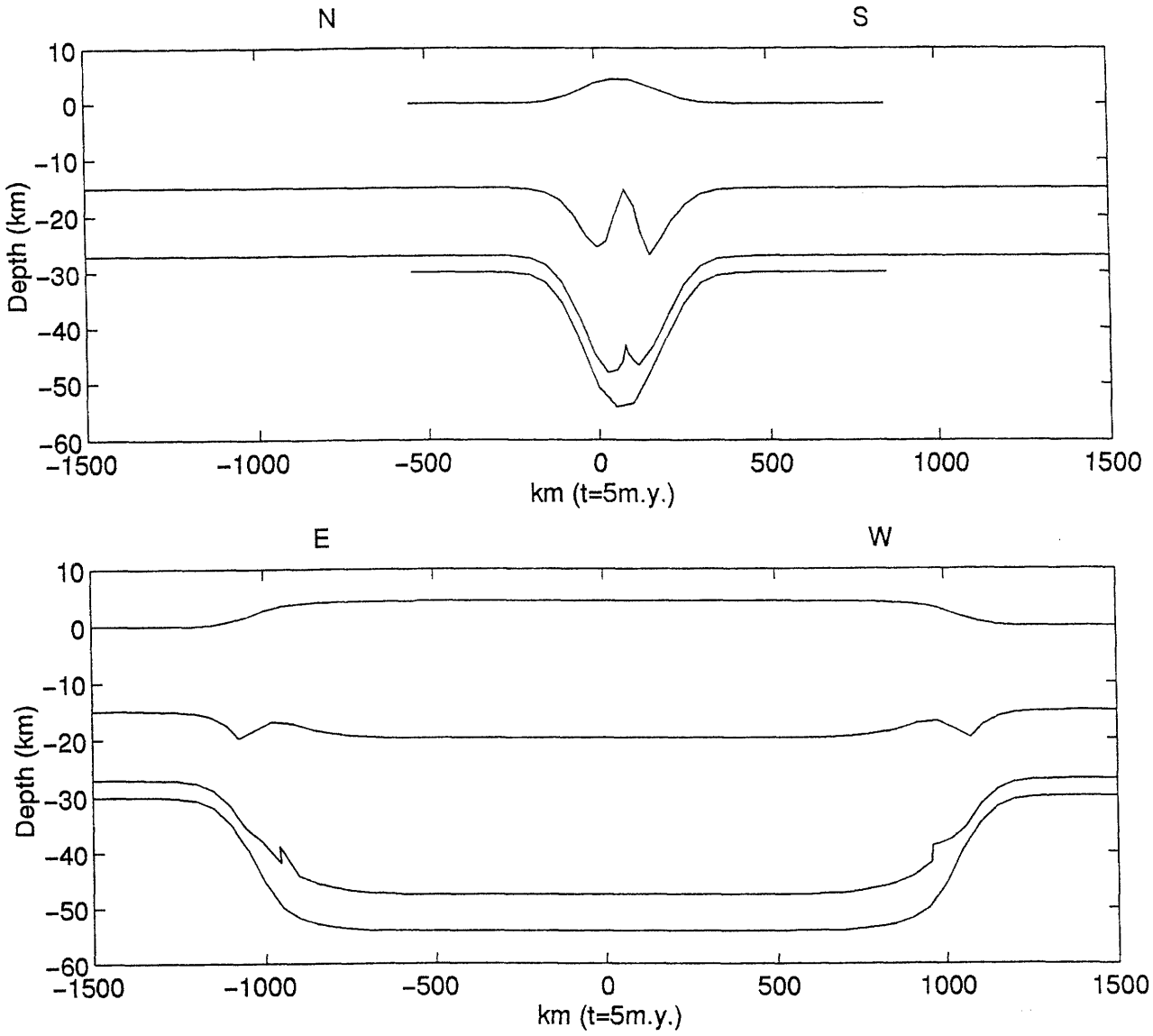

Figure 5-4 N-S and E-W cross sections showing model topography, crustal thickness of two initial layers after 5 m.y. convergence. The depths of the two initial horizontal layers are 15 km and 28 km, respectively.

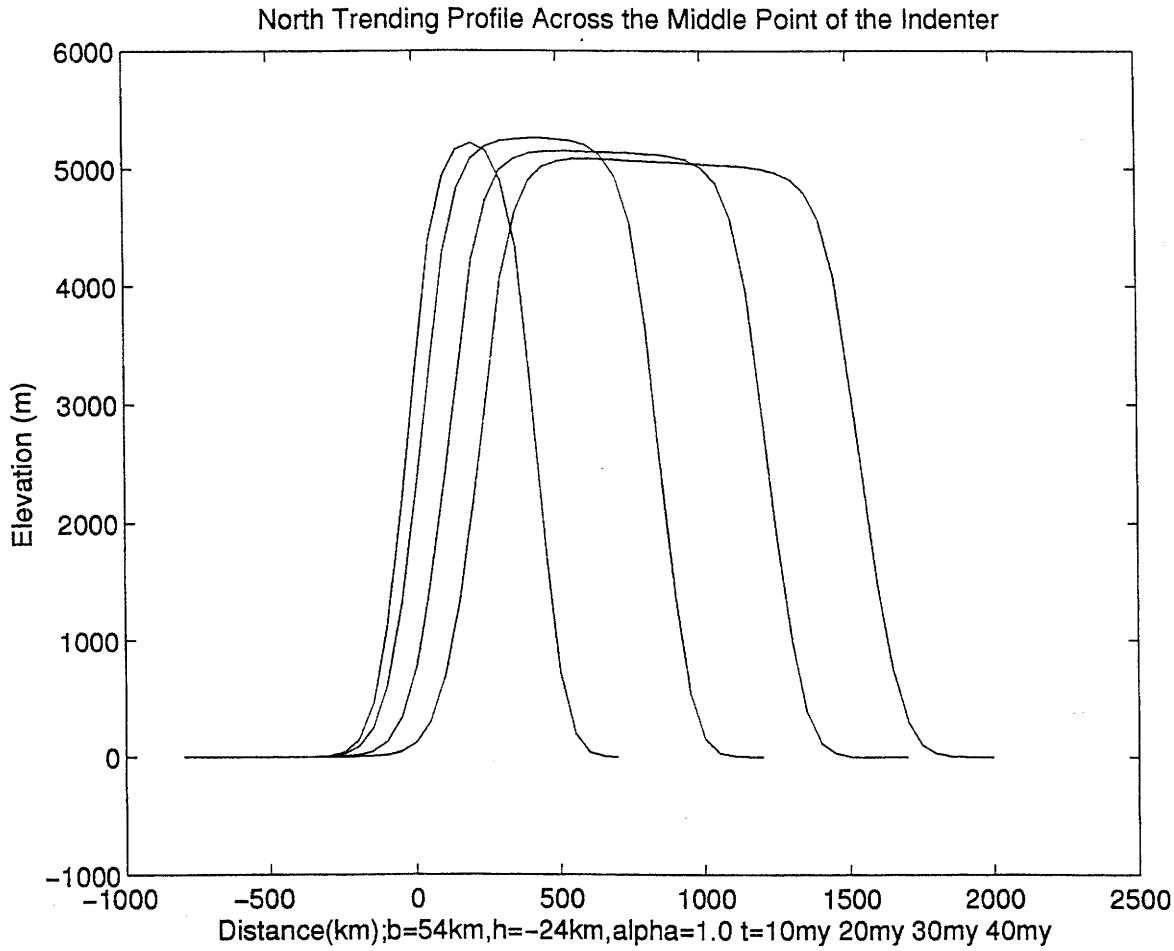

Figure 5-5a S-N treading profiles illustrate the development of plateau at the 'plateau phase' from 10 to 40 m.y. The curves represent the convergence at 10 m.y., 20 m.y., 30 m.y., and 40 m.y.

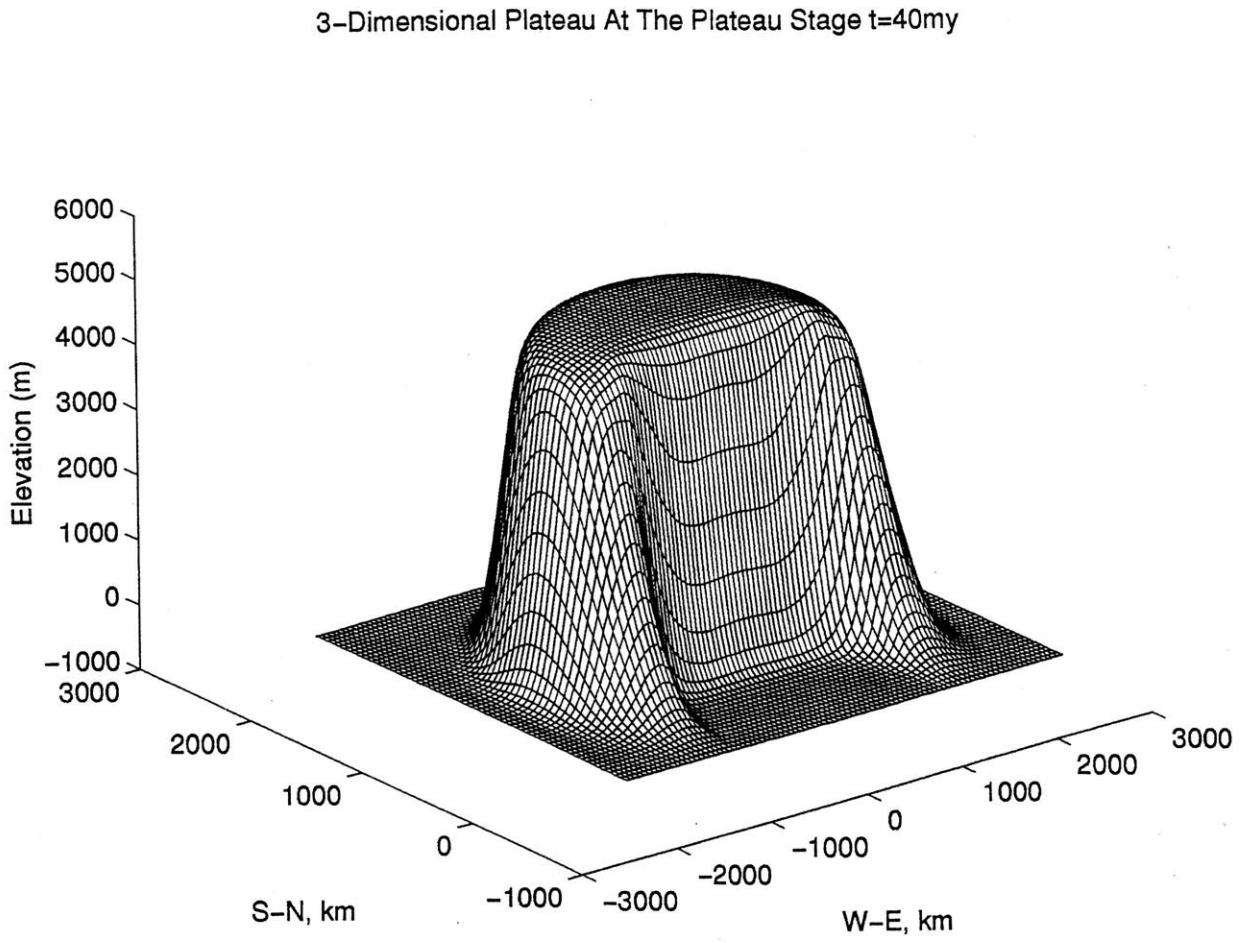

Figure 5-5b 3-D topography for the plateau at plateau stage after 40 m.y. convergence.

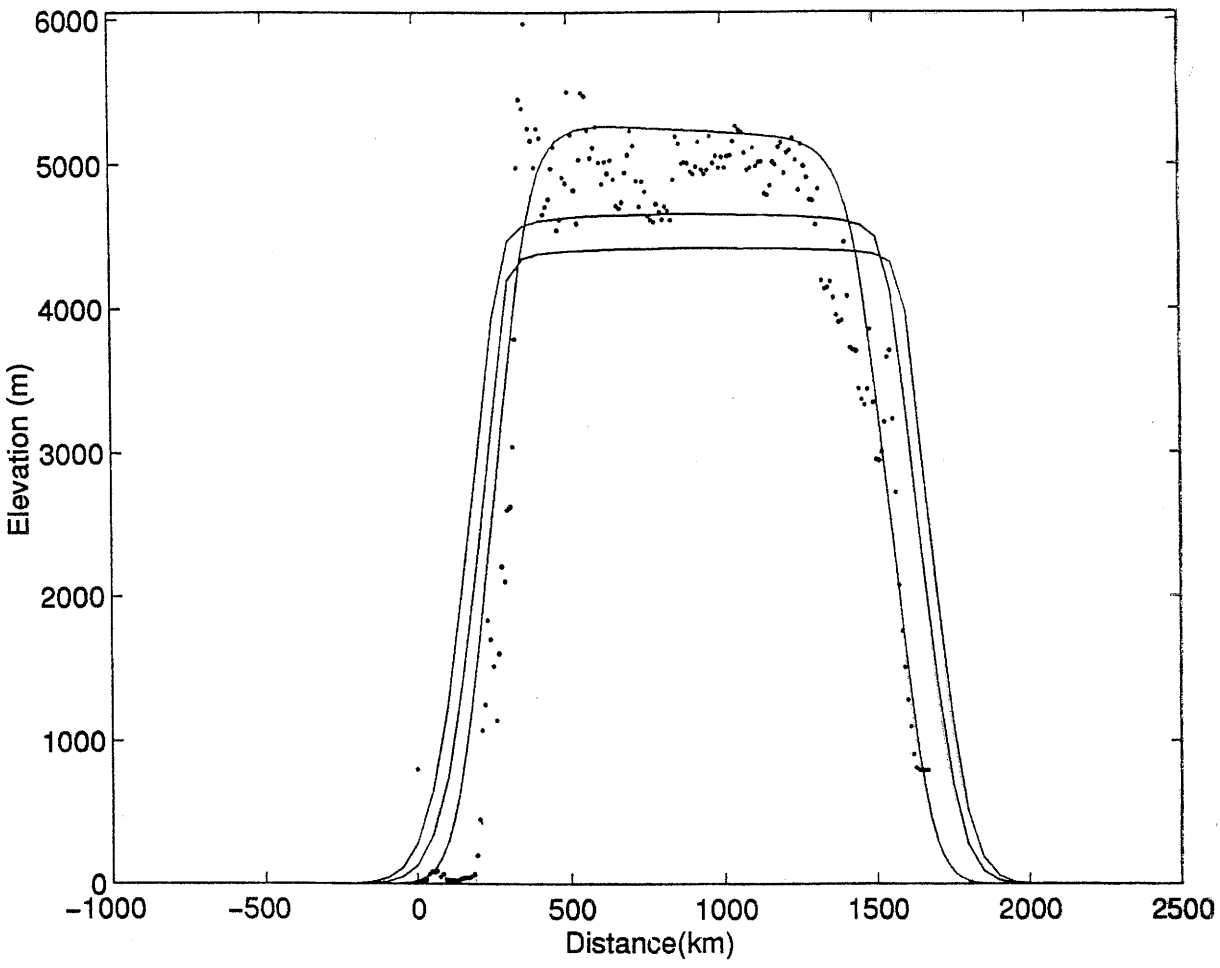

Figure 5-6 S-N trending profile for model Tibetan plateau. The dots represent observed data. Smooth lines represent modeled profiles with different viscosity decay coefficients (α) : 0.15, 0.25 and 1.0 km.

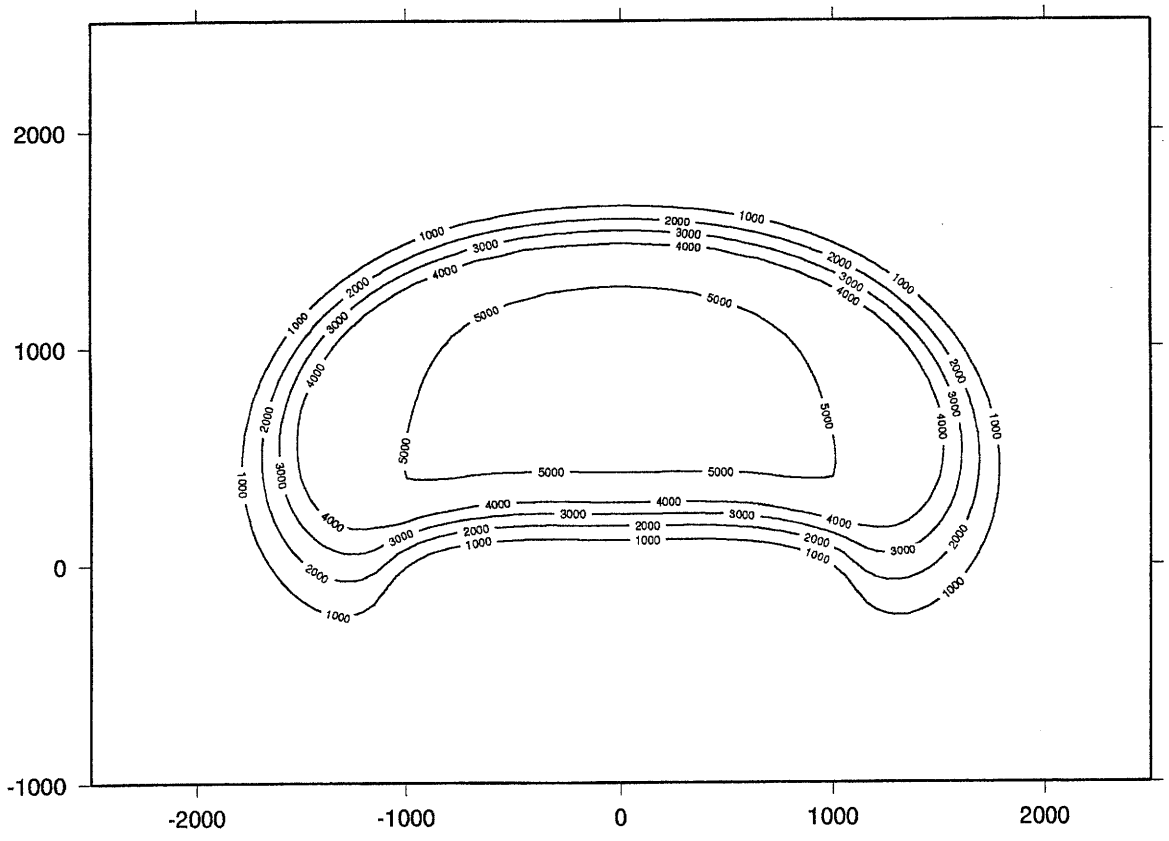

Figure 5-7 Topographic contour maps for the modeled plateau at 40 m.y. Viscosity decay coefficient α=1.0 km.

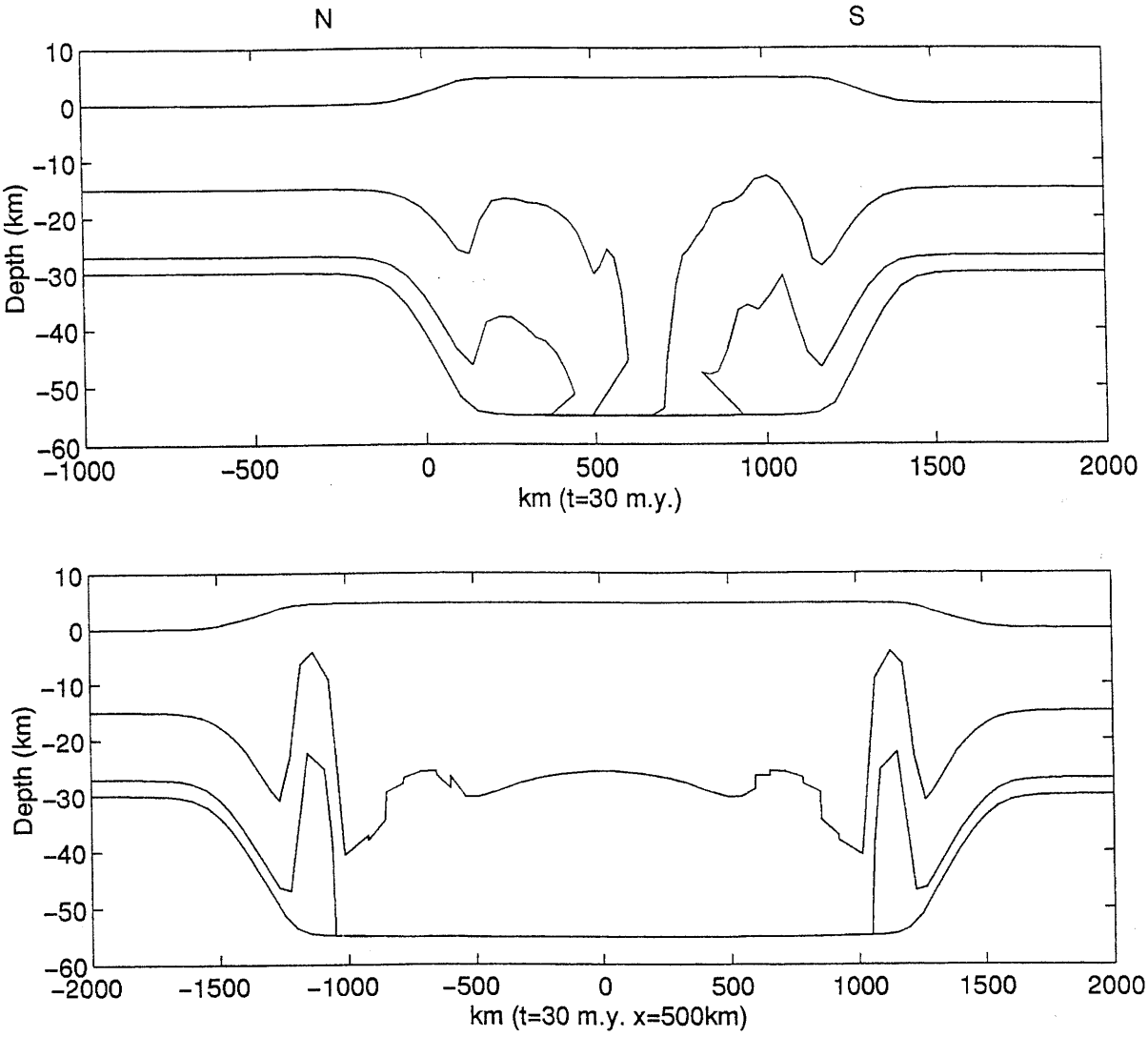

Figure 5-8 S-N and W-E cross sections showing model topography and crustal thickness of the two internal layers after 30 m.y. convergence for the weaker lower crust case (α=0.25). The depth of the two initial horizontal layers are 15 km and 28 km respectively.

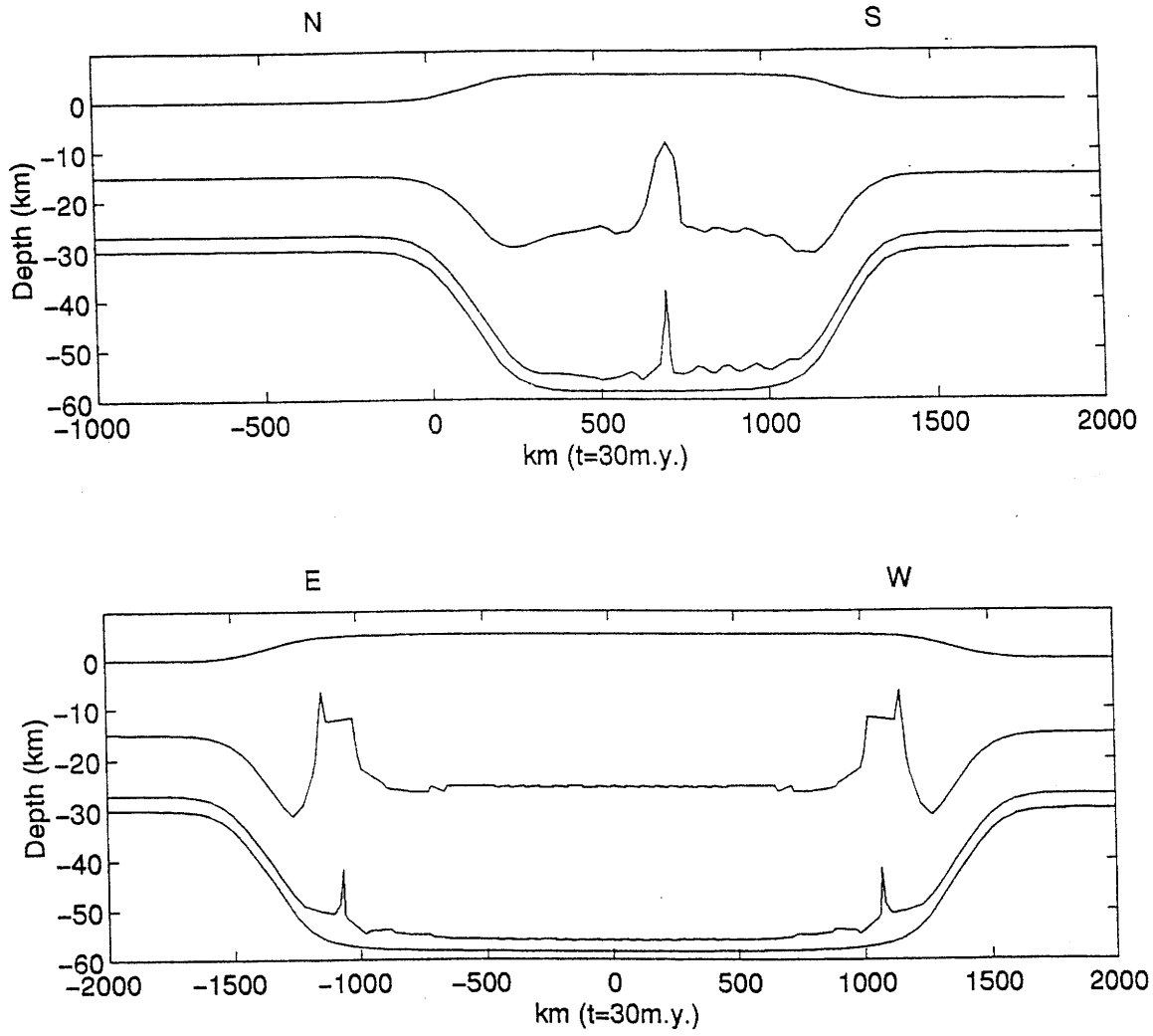

Figure 5-9 S-N and W-E cross sections showing model topography, crustal thickness of two internal layers after 30 m.y. convergence for the stronger lower crust case (α=1.). The depths of two initial horizontal layers are 15 km and 28 km, respectively.

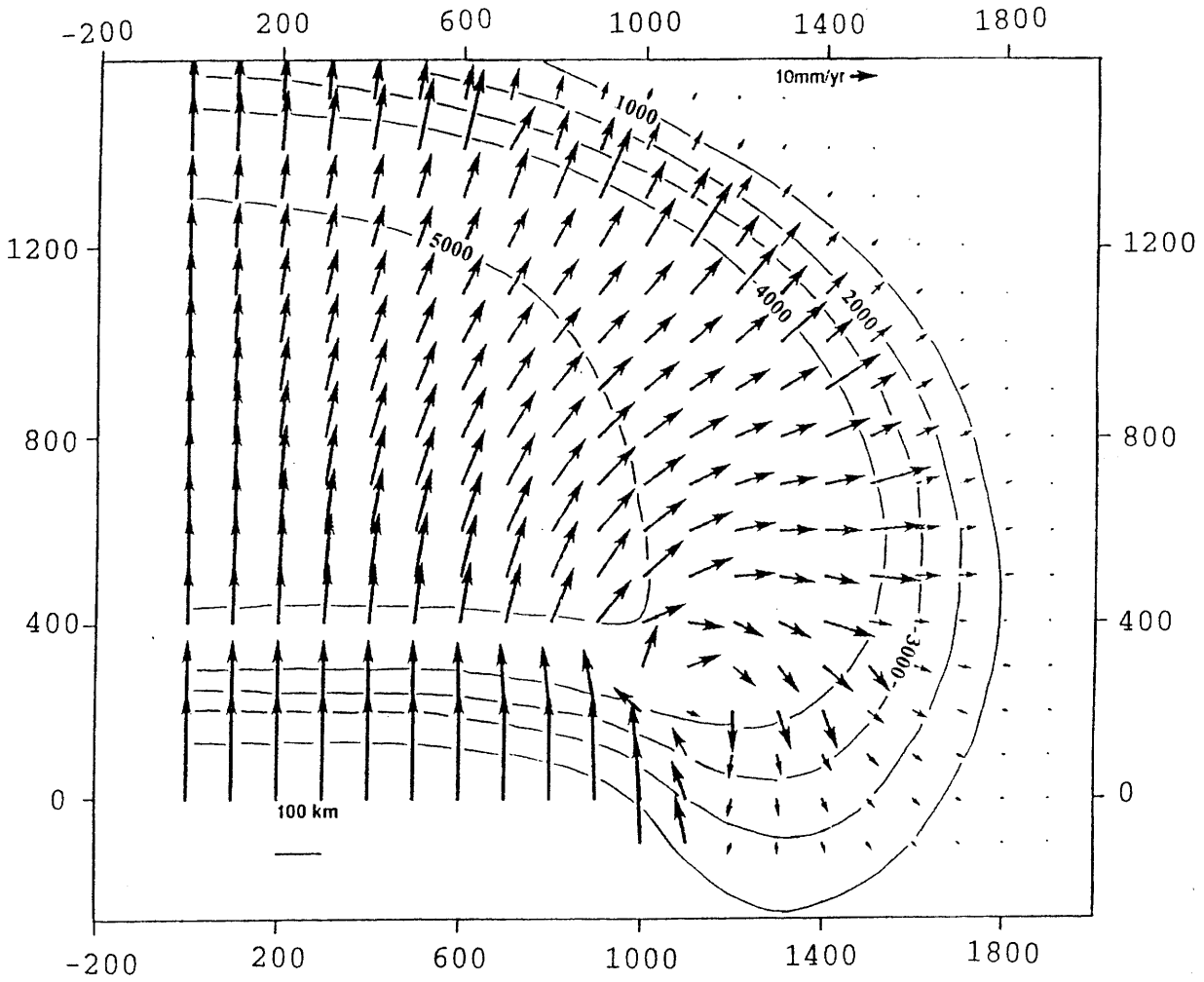

Figure 5-10 The velocity field calculated from the 3-D model (α=1.0 km), for the case of northward-directed subduction of India (Convergent velocity at the Indian plate is 40 mm/yr. Convergent velocity at the Asia is 10 mm/yr.

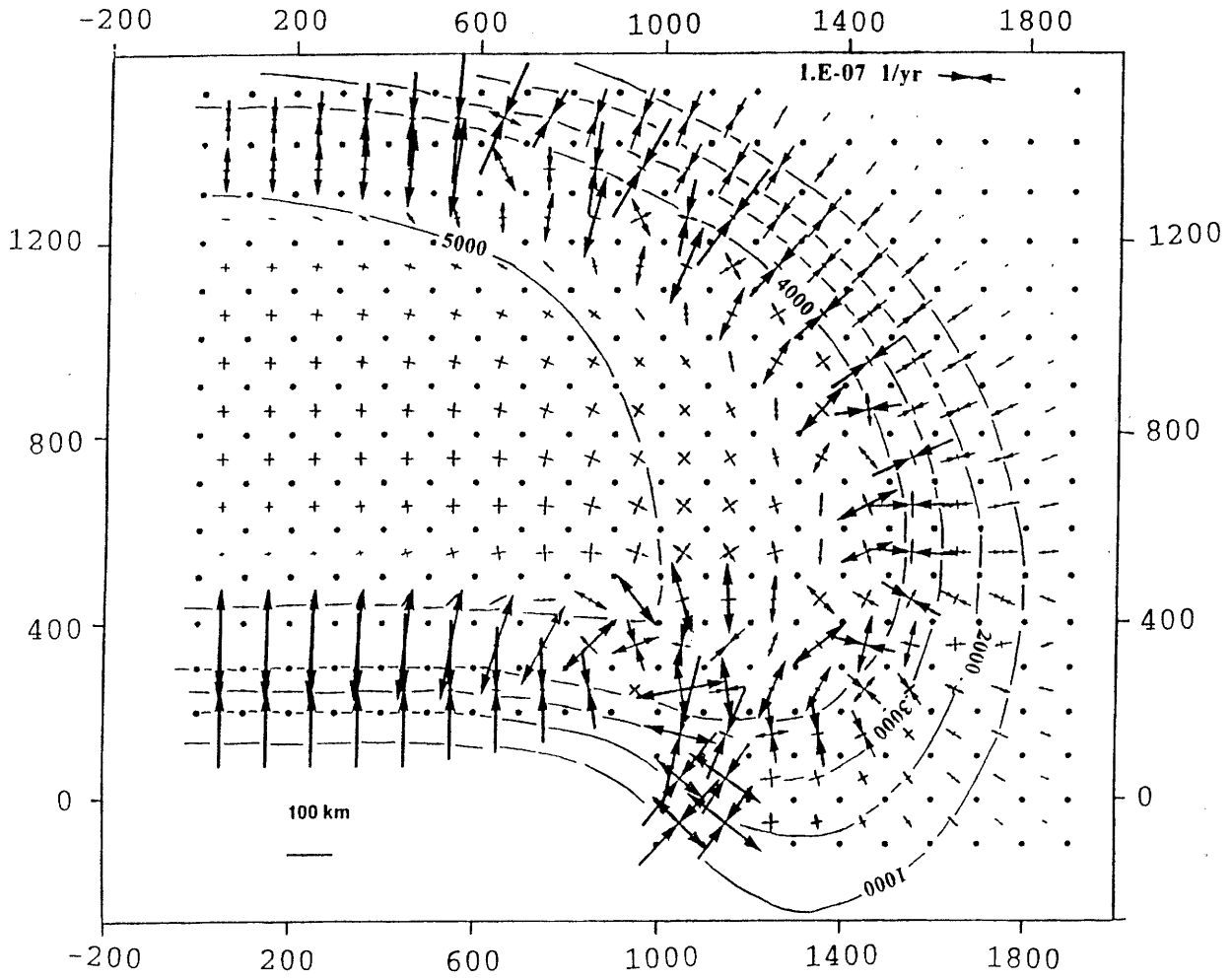

Figure 5-11 Principal axes of the horizontal strain rate tensors in the eastern syntaxis calculated from the modeled velocity field for the case of the northward-directed subduction of the India plate (velocity at the Indian plate is 40 mm/yr, velocity at the Eurasian is 10 mm/yr).

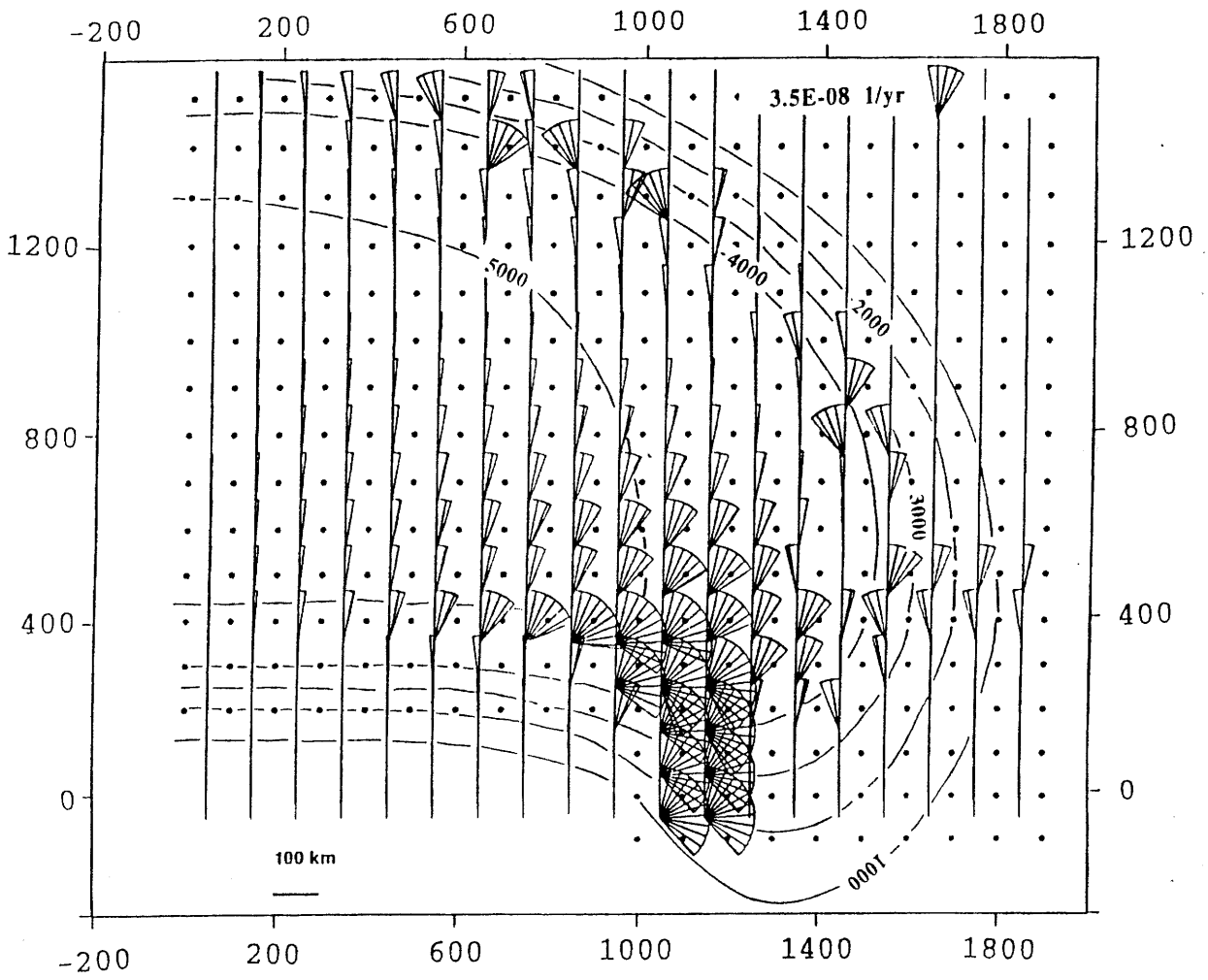

Figure 5-12 Rotation rates inferred from the model velocity field for the case of northward-directed subduction of the India plate (Velocity at the India plate is 40 mm/yr, velocity at the Eurasian is 10 mm/yr.).

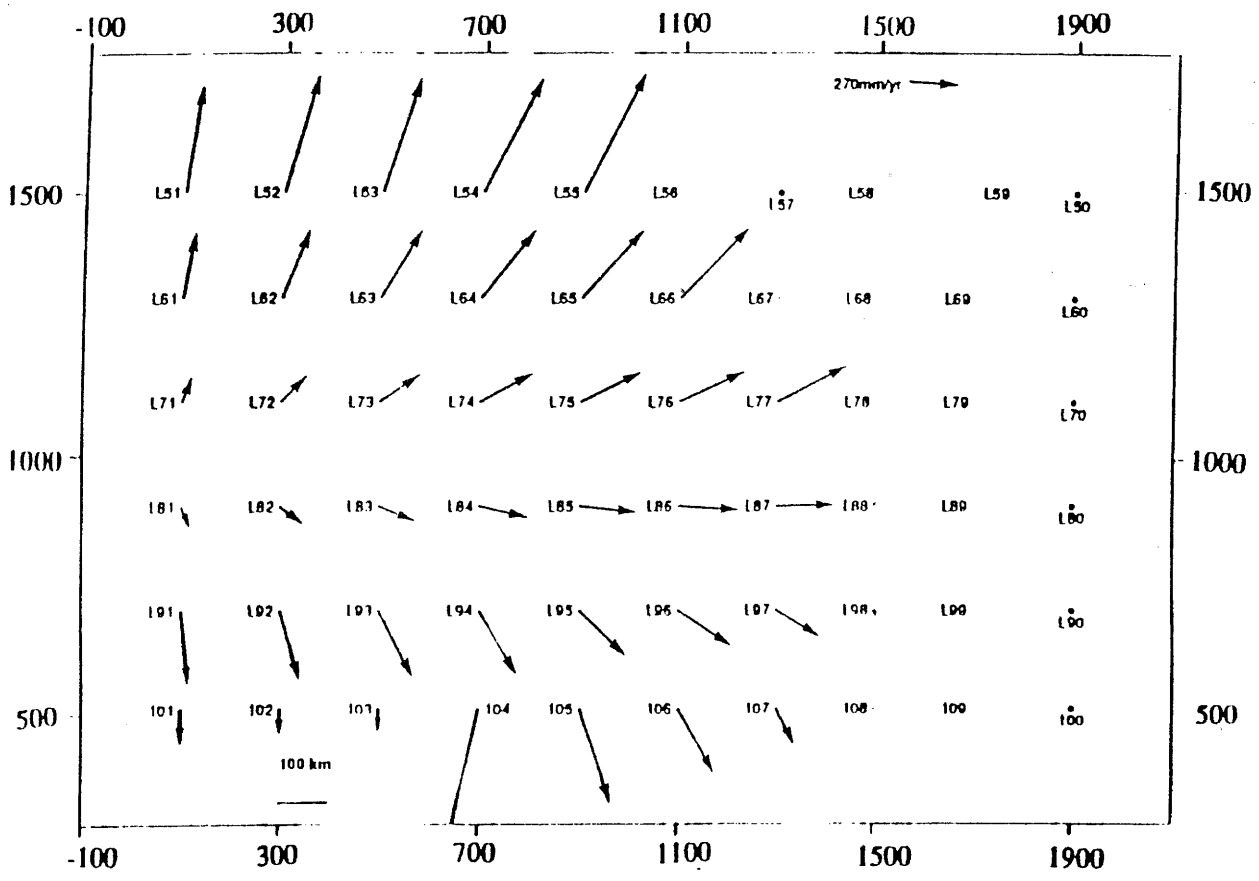

Figure 5-13a The lower crustal velocity filed at the depth z=h-1. The α has small value ($\alpha < 0.35$).

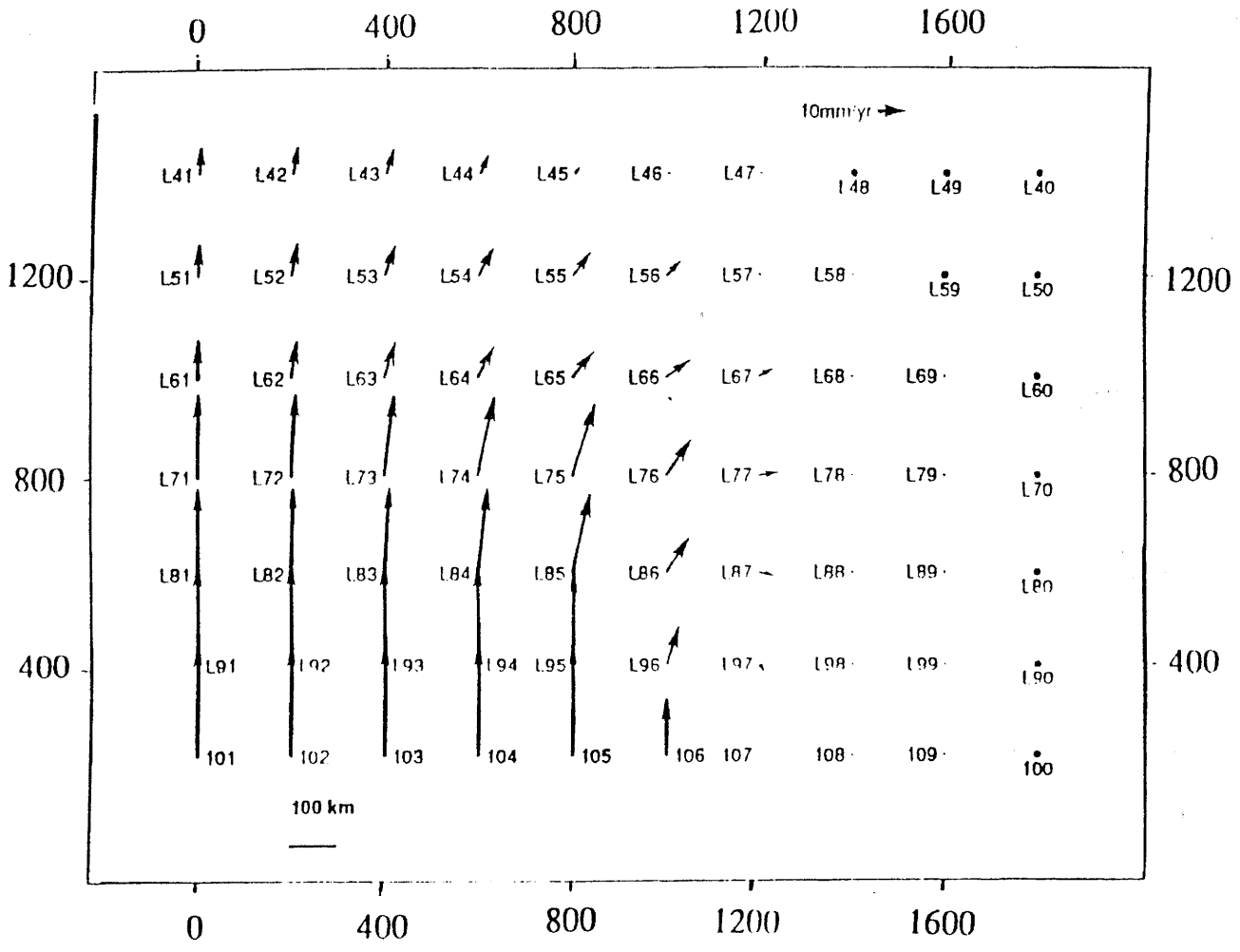

Figure 5-13b The lower crustal velocity filed at the depth z=h-1. The α has small value (α=1).